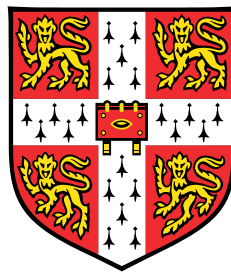


Modelling the impact of surface melt on the hydrology and dynamics of the Greenland Ice Sheet



Conrad Pawel Koziol

Department of Geography
University of Cambridge

This dissertation is submitted for the degree of
Doctor of Philosophy

St John's College

September 2017

Declaration

This dissertation is the result of my own work and includes nothing which is the outcome of work done in collaboration except as declared in the Preface and specified in the text. It is not substantially the same as any that I have submitted, or, is being concurrently submitted for a degree or diploma or other qualification at the University of Cambridge or any other University or similar institution except as declared in the Preface and specified in the text. I further state that no substantial part of my dissertation has already been submitted, or, is being concurrently submitted for any such degree, diploma or other qualification at the University of Cambridge or any other University or similar institution except as declared in the Preface and specified in the text. This dissertation contains fewer than 225 pages.

Conrad Pawel Koziol
September 2017

Acknowledgements

I would like to acknowledge: N. Arnold, R. Arthern, J. Bausch, R. Butler, P. Christoffersen, N. Davies, N. Douglass, G. Flowers, E. Frebold, D. Goldberg, D. Hall, R. Harris, I. Hewitt, R. Hussum, L. Koziol, T. Maciel, J. Maillard, A. McKay, E. Miles, B. Minchew, L. Souza, C. Schoof, J. Todd, T.J. Young.

Funding was generously provided through a St John's College Benefactors' Scholarship.

Abstract

Increasing surface runoff from the Greenland Ice Sheet due to a warming climate not only accelerates ice mass loss by altering surface mass balance, but may also lead to increased dynamic losses. This is because surface melt draining to the bed can reduce ice-bed coupling, leading to faster ice flow. Understanding the impact of surface melt on ice dynamics is important for constraining the contribution of the Greenland Ice Sheet to sea level rise.

The aim of this thesis is to numerically model the influence of surface runoff on ice velocities. Three new models are presented: an updated supraglacial hydrology model incorporating moulin and crevasse drainage, along with lake drainage over the ice surface via channel incision; an ice sheet model implementing a numerically efficient formulation of ice flow; an adjoint code of the ice flow model based on automatic differentiation. Together with a subglacial hydrology model, these represent the key components of the ice sheet system.

The supraglacial hydrology model is calibrated in the Paakitsoq region. Model output shows the partitioning of melt between different drainage pathways and the spatial distribution of surface drainage. Melt season intensity is found to be a relevant factor for both.

A key challenge for simulations applying a coupled ice-flow/hydrology model is state and parameter initialization. This challenge is addressed by developing a new workflow for incorporating modelled subglacial water pressures into inversions of basal drag. A current subglacial hydrology model is run for a winter season, and the output is incorporated into the workflow to invert for basal drag at the start of summer in the Russell Glacier area. Comparison of the modelled subglacial system to observations suggests that model output is more in line with summer conditions than winter conditions.

A multicomponent model integrating the main components of the ice sheet system is developed and applied to the Russell Glacier area. A coupled ice-flow/hydrology model is initialized using the proposed workflow, and driven using output from the supraglacial hydrology model. Three recent melt seasons are modelled. To a first order, predicted ice velocities match measured velocities at multiple GPS sites. This affirms the conceptual model that summer velocity patterns are driven by transitions between distributed and channelized subglacial hydrological systems.

Table of Contents

List of Figures	xiii
List of Tables	xvii
1 Introduction	1
1.1 Overview	1
2 Literature Review	5
2.1 Overview	5
2.2 Greenland Ice Sheet Mass Balance	5
2.3 Greenland Ice Sheet Hydrology	6
2.3.1 Surface Hydrology	7
2.3.2 Englacial Hydrology	15
2.3.3 Subglacial Hydrology	18
2.4 Ice Dynamics	21
3 Surface Hydrology	29
3.1 Overview	29
3.2 Introduction	30
3.3 Methods	31
3.3.1 Model Formulation	32
3.3.2 Study Area and DEM	36
3.3.3 Crevasse and Moulin Locations	37
3.3.4 Driving Variables	39
3.3.5 Simulation Design	40
3.4 Results	42
3.4.1 Standard Run	42
3.4.2 Sensitivity Analysis	46
3.4.3 Interannual Comparison	47

3.5	Discussion	49
3.6	Conclusions	52
4	Ice Sheet Modelling and Inversions	55
4.1	Overview	55
4.2	Introduction	56
4.3	Methods	59
4.3.1	Hybrid Ice Sheet Model	59
4.3.2	Inversion Model	63
4.3.3	Subglacial Hydrology Model	70
4.3.4	Test Simulations	70
4.3.5	Application to Russell Glacier Area	72
4.4	Results	77
4.4.1	Model Verification	77
4.4.2	Application to Russell Glacier Area	81
4.5	Discussion	89
4.5.1	Methods	89
4.5.2	Application	96
4.6	Conclusions	98
5	Integrated Modelling	99
5.1	Overview	99
5.2	Introduction	99
5.3	Methods	101
5.3.1	Study Area and Datasets	102
5.3.2	Supraglacial Hydrology	104
5.3.3	Subglacial Hydrology	104
5.3.4	Ice Flow/Inversion	107
5.3.5	Model Integration	109
5.3.6	Workflow	110
5.3.7	Simulations	111
5.4	Results	112
5.4.1	Supraglacial Input	112
5.4.2	Calibration	114
5.4.3	Model Sensitivity	118
5.4.4	Validation	119
5.4.5	Future Scenario	119

5.4.6	Average Melt Season Velocities	121
5.4.7	Channel Network Morphology/Extent	121
5.4.8	Distributed and Channelized Discharge	124
5.5	Discussion	126
5.5.1	Model Fit	126
5.5.2	Model Sensitivity	128
5.5.3	Model Complexity	130
5.5.4	Implications	131
5.6	Conclusions	133
6	Conclusions	135
6.1	Summary of Thesis	135
6.2	Directions for Future Work	136
6.3	Concluding Remarks	138
	References	139
	Appendix A Additional Sensitivity Analysis Plots of the Integrated Model	151

List of Figures

2.1	Ice mass loss from ice sheets	7
2.2	Illustration of the hydrological system of a land-terminating section of the Greenland Ice Sheet	8
2.3	Image of lake distribution at two different points in the melt season.	9
2.4	Distribution and statistics of lake drainage types.	12
2.5	Location of Paakitsoq Region.	13
2.6	Comparison of manual and automated methods for supra glacial lake identification	16
2.7	The physics of channels and cavities.	19
2.8	Summer melt compared to ice velocities.	24
3.1	Schematic drawing of lake drainage by channel incision	33
3.2	Paakitsoq region study area	36
3.3	Overlay of observed and modelled streams in the Paakitsoq area	37
3.4	Modelled crevassed areas over the Paakitsoq area	39
3.5	Modelled surface runoff over the Paakitsoq area	40
3.6	Sensitivity analysis of partitioning between different meltwater pathways	43
3.7	Bar graph of drainage at different elevations for three different melt seasons	44
3.8	Map of modelled lake fates in the Paakitsoq area	45
3.9	Channelized drainage lake hydrographs	46
4.1	Russell Glacier study area.	73
4.2	Velocity measurements and reported error in the Russell Glacier area.	74
4.3	Surface and bed topography in the Russell Glacier area	75
4.4	Flow chart of workflow for non-linear inversions	76
4.5	ISMIP-HOM Experiment A at 10 km, 40 km, and 80 km domain lengths.	78
4.6	ISMIP-HOM Experiment C at 10 km, 40 km, and 80 km domain lengths.	78

4.7	Grid convergence for ISMIP-HOM Experiments A and C at 40 km domain length	79
4.8	Convergence of Picard iterations for Experiment C at 40km and Experiment A at 10km for different methods of calculating viscosity.	79
4.9	Linear sliding law identical twin test	80
4.10	Equifinality of inversions for the identical twin test of the linear sliding law.	81
4.11	Generalized Weertman sliding law identical twin test	82
4.12	Schoof sliding law identical twin test	83
4.13	L-curve for inversion of the Russell Glacier area using a linear sliding law	84
4.14	Convergence of inversion using linear sliding law applied to the Russell Glacier area.	85
4.15	Histogram and map of discrepancy between observed and inverted velocities.	85
4.16	Inverted basal parameters and sliding ratio using a linear sliding law.	86
4.17	Modelled basal melt rate	87
4.18	Subglacial hydrological system evolution	87
4.19	Subglacial hydrology discharge and effective pressure for the winter subglacial hydrology run	88
4.20	L-curve for inversion of the Russell Glacier area using a generalized Weertman sliding law	89
4.21	Histogram and map of discrepancy between observed and inverted velocities for generalized Weertman sliding law.	90
4.22	Inverted basal parameters and sliding ratio using a generalized Weertman sliding law.	91
4.23	L-curve for inversion of the Russell Glacier area using a Schoof sliding law	92
4.24	Histogram and map of discrepancy between observed and inverted velocities for a Schoof sliding law.	93
4.25	Inverted basal parameters and sliding ratio using a Schoof sliding law.	94
5.1	Russell Glacier study area.	102
5.2	Modelled daily surface runoff in the Russell Glacier area.	103
5.3	Schematic drawing of crevasse drainage.	110
5.4	Flow chart of workflow for integrated model runs	111
5.5	Pie chart of surface runoff partitioning into different meltwater pathways for the 2009 melt season in the Russell Glacier area	112
5.6	Modelled supraglacial drainage in the Russell Glacier area for 2009.	113
5.7	Modelled ice velocities plotted against GPS measurements for the 2009 melt season	115

5.8	Modelled ice velocities plotted against GPS measurements for the 2011 melt season	116
5.9	Modelled ice velocities plotted against GPS measurements for the 2012 melt season	120
5.10	Modelled ice velocities under potential future melt scenarios	122
5.11	Average melt season velocities at GPS stations	123
5.12	Change (%) in averaged modelled melt season velocities over the whole study area between 2009 and 2011x4.	123
5.13	Channelized system morphology at maximum summer extent for 2009, 2011, and 2012	125
5.14	Time series of discharge in the distributed and channelized system for three different summers and a future melt scenario	126
A.1	Sensitivity analysis of crevasse drainage	152
A.2	Sensitivity analysis of lake hydrofracture events	153
A.3	Sensitivity analysis of englacial storage	154
A.4	Sensitivity analysis of hydraulic conductivity	155
A.5	Measured and modelled velocities at 6 h intervals	156

List of Tables

3.1	Parameters for the surface hydrology model	34
3.2	Remotely sensed and modelled lake drainage statistics for 2009	41
3.3	Parameters and values varied in the sensitivity analysis	41
3.4	Statistics of lake hydrofracture and lake drainage via channelization for each of the modelled runs.	47
4.1	Constants for ISMIP-HOM experiments.	71
4.2	Constants used in the ice sheet/inversion model applied to the Russell Glacier area.	76
5.1	Constants used for the subglacial hydrology during integrated runs in the Russell Glacier area.	107
5.2	Constants used in ice flow model/inversion code applied to the Russell Glacier area for integrated runs.	108

Chapter 1

Introduction

1.1 Overview

Ice mass loss from the Greenland Ice Sheet is a significant contributor to global sea level rise. Over the last two decades, the annual contribution from the Greenland Ice Sheet is estimated to have doubled, rising from 0.33 mm yr^{-1} to 0.66 mm yr^{-1} . Its total contribution over this period represents approximately 11% of global sea level rise. The proportion the Greenland Ice Sheet contributes to sea level rise is predicted to increase over the coming decades (Vaughan et al., 2013). With total ice mass equivalent to 7m of sea level rise (Alley et al., 2005), and accelerating ice mass loss (Rignot et al., 2011; Shepherd et al., 2012), understanding the evolution of the ice sheet in the coming decades will be important to accurately forecasting and responding to increasing sea levels.

Surface melt on the Greenland Ice Sheet which does not refreeze can be intercepted by surface features and drain to the base. Crevasses, moulins, and ice fractures caused by rapidly draining lakes allow water to enter the subglacial system. The subglacial system dynamically responds to input, and is predicted to evolve between a low pressure channelized system, and a high pressure distributed system. Since water pressure is an important control on basal drag, the evolution of the hydrological system is a strong control on ice velocities.

Recent acceleration of ice mass loss from the Greenland Ice Sheet is attributed to increased calving of marine-terminating glaciers and increased surface melt runoff (van den Broeke et al., 2009). In addition to removing ice mass from the surface of the Greenland Ice Sheet, increased surface melt runoff may further contribute to ice mass loss by influencing the velocity structure of the Greenland Ice Sheet. Therefore, the long-term impact of increased amounts of surface melt reaching the base of the glacier on ice loss is an open question. If increased surface melt results in a significant acceleration of the ice sheet, there is the

potential for a positive feedback, as faster flow will decrease the elevation of the ice sheet, further increasing surface melt (Joughin et al., 2008; Schoof, 2010; Zwally et al., 2002).

The aim of this thesis is to investigate the hypothesis that increasing amounts of surface melt on the Greenland Ice Sheet will lead faster ice sheet flow at the margin. In order to address this hypothesis, this work advances both the understanding of individual components of the ice sheet system, and the dynamic behaviour of the system as a whole. The goals of the thesis are: a) improve a current surface hydrology model and investigate the partitioning of surface runoff into different drainage pathways to the ice-bed interface; b) develop an ice sheet/inversion code, integrate it with a current generation subglacial hydrology model, and apply the coupled model to invert for basal parameters during the winter; c) interface the surface hydrology model to the coupled ice flow/subglacial hydrology model, and use the integrated model to investigate how ice sheet velocities may vary in melt seasons of different intensities.

The chapters of the thesis are organized as follows:

Chapter one contains a brief introduction and overview of the thesis. Here, we introduce the importance of ice mass loss from the Greenland Ice Sheet, state that the aim of the thesis is to investigate the influence of increased surface melt on ice acceleration, and outline the chapters of the thesis.

Chapter two contains a literature review. The chapter begins with an overview of the partitioning of mass loss of the Greenland Ice Sheet into surface mass changes, and dynamic losses via calving. Next follows a review of glacier hydrology, which is divided into sections on surface hydrology, englacial hydrology, and subglacial hydrology. The chapter concludes with a review of ice dynamics of land-terminating sectors of the Greenland Ice Sheet, with a focus on interactions between ice flow and hydrology.

Chapter three presents improvements to a current surface hydrological model, and a new application to the Paakitsoq Region, Western Greenland. In this chapter, we begin by describing model enhancements, which include: runoff drainage into crevasses; runoff drainage into moulins outside of lake basins; supraglacial lake drainage via channel incision at the edge (slow drainage). Description of the model is followed by a discussion of the variety of remote sensing data incorporated in the model during simulations. The results subsection focuses on the partitioning of meltwater into different drainage pathways, and the influence of melt season intensity. The next section discusses that partitioning of meltwater varies non-linearly with melt season intensity, as well as some of the limitations of the model. The conclusion highlights that as melt season intensity increases, an increased proportion of water may drain at higher elevations.

Chapter four presents a new ice sheet model and its associated adjoint model, as well as a novel application to the Greenland Ice Sheet incorporating modelled subglacial water pressures. The chapter begins with an introduction to ice sheet modelling, and the formulation of both the ice sheet model and its adjoint. A current subglacial hydrology model (Hewitt, 2013) is also briefly described to provide context for its application. Next, a workflow for incorporating modelled subglacial water pressures in inversions using non-linear sliding laws is presented. The results include standardized tests verifying and validating the ice sheet model/inversion code, and the application to the Russell Glacier area. The discussion focuses on some of the numerics and implementation issues of the models developed, and compares the output of the subglacial hydrology model during winter to the limited data available. The conclusion highlights that the models are robust, but the hydrology model output is more in line with summer observations than winter observations.

Chapter five presents the results of combining the models from the previous chapters to predict summer velocities in the Russell Glacier area. The chapter begins with an introduction to our current understanding of the impact of summer melt on ice velocities. The methods section includes the coupling of the ice flow model to the subglacial hydrology model, its initialization using the workflow from Chapter 4, and its forcing using the supraglacial hydrology model developed in Chapter 3. The results show the model calibration based on GPS data from two summer melt seasons, and its validation using GPS data from a third melt season. The discussion touches upon the modelling process itself, the model fit to measured velocities, and implications for the future response of the ice sheet. The main outcome from this chapter is to provide quantitative support for the hypothesis that summer acceleration of the Greenland Ice Sheet is forced by subglacial hydrology in a manner analogous to the speedup observed in alpine glaciers.

Chapter six provides a brief synthesis of the work in the thesis, direction for future work, and concluding remarks.

Chapter 2

Literature Review

2.1 Overview

The literature review is organized into four sections:

This first section details the organization of the chapter. The second section is a review of mass loss from the Greenland Ice Sheet (GrIS). It discusses the acceleration of ice mass loss from the GrIS, and the partitioning of ice mass loss between surface mass balance changes and dynamic losses. Since ice mass loss from the GrIS is a significant contributor to sea level rise, this section serves as a motivation for the thesis. Section three is a review of ice sheet hydrology. It contains subsections on surface hydrology, englacial hydrology, and basal hydrology. Together, these components have an important impact on ice sheet flow. Surface hydrology controls the spatial and temporal patterns of meltwater drainage from the ice surface, which via the englacial system, can drain into the subglacial system. Meltwater draining into the subglacial system is an important control on water pressures, and hence basal drag. The last section (four) is focused on ice dynamics, and in particular, the interactions between surface hydrology, basal hydrology, and ice flow. The complex feedbacks between these systems contributes to the uncertainty in estimates of future contributions of the GrIS to global sea level rise. In each section/subsection of this chapter, we begin by considering the observational evidence, followed by the results of numerical and theoretical work.

2.2 Greenland Ice Sheet Mass Balance

Ice-sheets gain and lose mass through precipitation, runoff, sublimation, and calving (Cuffey and Paterson, 2010). Based on an analysis of satellite gravimetry, altimetry, and interferometry datasets, Shepherd et al. (2012) report that between the years 1992 and 2011 the GrIS lost

2700 ± 930 Gt of ice. This is approximately twice the ice mass loss that is reported for the Antarctic Ice Sheet over the same period. Assuming that 360Gt of ice is equivalent to 1mm of sea level rise, the loss from the GrIS between 1992 and 2011 corresponds to 7.5 ± 2.58mm sea level rise (Figure 2.1) (Shepherd et al., 2012).

Ice mass loss from the GrIS has accelerated over the last two decades at an average rate of 21.9 ± 1 Gt yr⁻². This is approximately one and a half times the acceleration measured in Antarctica, and three times greater than that measured for glaciers and ice caps (Rignot et al., 2011). Estimates place ice mass loss at a rate of 51 ± 65 Gt yr⁻¹ between 1992 and 2000, and 263 ± 30 Gt yr⁻¹ between 2005 and 2011 (Shepherd et al., 2012). Although the GrIS has experienced a negative mass balance since 1990s, large inter-annual and spatial variability exists, particularly in the surface mass balance (SMB) component (van den Broeke et al., 2009).

Ice mass loss can be divided into SMB and ice discharge components. Between 1996 and 2009, both SMB and ice discharge contributed approximately 50% to cumulative ice mass loss. Between 2003 and 2008, approximately half of the total ice mass loss occurred in the southeast, where the primary mechanism of ice mass loss was calving (van den Broeke et al., 2009). Pritchard et al. (2009) reports that much of the margin of the GRiS is thinning due to a negative surface mass balance, with a concentration of dynamic loss in marine-terminating glaciers experiencing accelerated flow. Although fast flowing glaciers occur in all latitudes, their contribution to mass loss is most significant in the southeast and northwest of the GrIS. Overall, fast flowing (>100myr⁻¹) portions of the ice sheet thinned significantly more rapidly than slow-flowing portions (0.84myr⁻¹ vs 0.12myr⁻¹) of the ice sheet (Pritchard et al., 2009)

Enderlin et al. (2014) report a strong localization in ice mass loss, with 15 outlet glaciers of the 178 surveyed responsible for 77% of ice mass loss due to acceleration since 2000. Additionally, only 4 glaciers were responsible of 50% of that ice mass loss. From 2000-2005, marine terminating glaciers accelerated and accounted for 58% of ice mass loss. This has been attributed to warmer water inflow due to a weak North Atlantic Oscillation (NAO). Since then, this fraction has decreased, and since 2009 SMB has accounted for 84% of ice mass loss.

2.3 Greenland Ice Sheet Hydrology

The hydrology of the GrIS is potentially a significant driver of dynamic change. Ice velocities during the summer melt season are observed to speed up by 50% to 100% (Joughin et al., 2008) in Western Greenland. Both theoretical work (Hewitt, 2013; Schoof, 2010) and

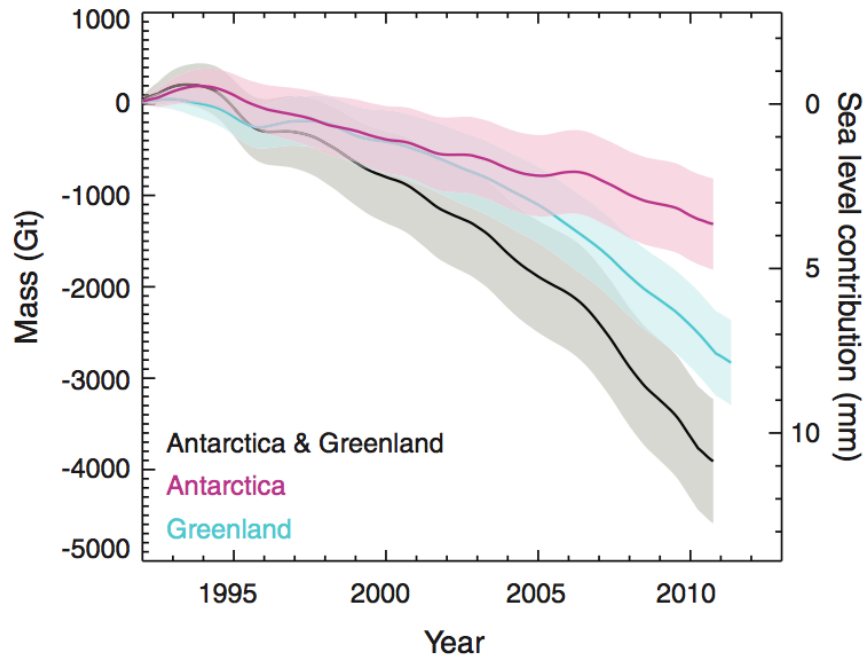


Fig. 2.1 Cumulative changes in the mass of ice sheets. [Reprinted from (Shepherd et al., 2012)]

observational studies (Das et al., 2008; van de Wal et al., 2008; Zwally et al., 2002) suggest coupling between surface melt and ice dynamics as the mechanism behind this variability.

Surface melt forms networks of supraglacial channels and lakes, and can enter the ice-bed interface through crevasses and moulins (Figure 2.2). Supraglacial lakes can hydraulically fracture ('hydrofracture') the ice beneath them (Das et al., 2008; van der Veen, 2007) leading to the rapid drainage of large quantities of water to bed, forming a surface-to-bed connection (moulin) that remains open for the melt season (Banwell et al., 2013; Selmes et al., 2011). Recent studies have shown that the pattern and timing of water entering the subglacial hydrological system impacts ice velocities, with increased ice velocities corresponding to higher variability of melt input to the subglacial system (Bartholomew et al., 2011a; Colgan et al., 2011b; Schoof, 2010). This has raised the possibility of a positive feedback, whereby increased ice velocities driven by surface melt decrease the elevation of the GrIS, increasing the ablation area (Das et al., 2008; Zwally et al., 2002).

2.3.1 Surface Hydrology

Surface runoff incises into the ice in the ablation zone to form channels. These channels connect to form an arborescent network of channels in the ablation zone similar to terrestrial

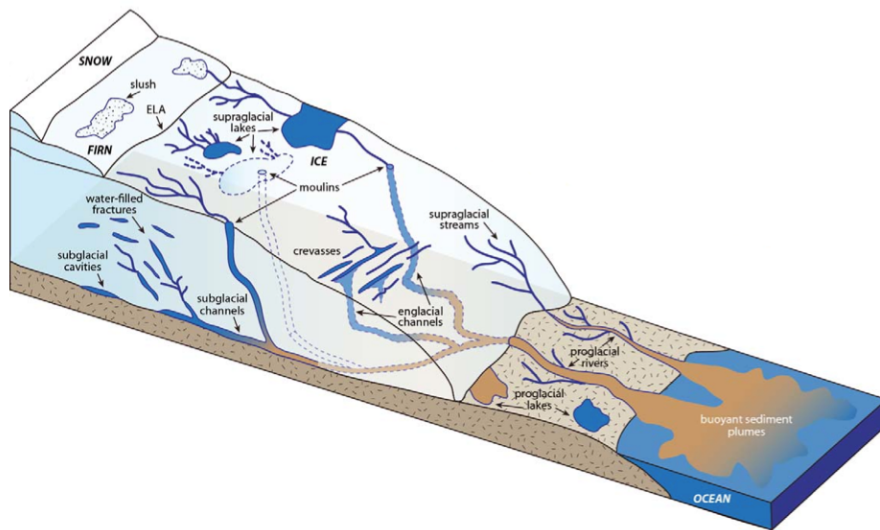


Fig. 2.2 Components of the hydrological system of a land-terminating section of the Greenland Ice Sheet. [Reprinted from Chu (2013)]

river systems (Cuffey and Paterson, 2010). The properties of the system are likely broadly influenced by the contributing area, local topography, runoff volume, and surface characteristics, and evolve during the course of the summer (Irvine-Fynn et al., 2011). Water in surface channels that intercept crevasses, moulins, and supraglacial lakes can be routed into the englacial and subglacial hydrological systems.

A significant proportion of surface meltwater drains into the englacial system, with observations at the ice margin showing the majority of water exiting through subglacial channels and only limited flow over the ice edge (Zwally et al., 2002). Mapping of supraglacial stream networks in the ice sheet watershed of Leverett glacier, southwest Greenland shows all observed meltwater rivers draining into the englacial hydrological system prior to reaching the ice margin (Smith et al., 2015). Under optimal conditions, the ice sheet surface is observed to be well drained, with a high supraglacial river flux and low observed water storage in supraglacial lakes (Smith et al., 2015).

Observations also show that at high elevations (1200-2000 m), surface runoff can be stored in firn aquifers (Harper et al., 2012). Water flow through firn can delay the transport of water downstream, as well contribute to refreezing of meltwater, buffering the impact of increased surface melt on sea level rise (Forster et al., 2013; Harper et al., 2012). Recent work suggests that firn will continue to act as a buffer for surface melt in the near future, but its long-term capacity for that is unclear (Harper et al., 2012; Noël et al., 2017).

Supraglacial lakes form seasonally across the ablation zone of the GrIS (Johansson et al., 2013; Luthje et al., 2006; Selmes et al., 2011). Their distribution is concentrated in the

southwest region, which has approximately 55% of the lake population, while they are sparsest in the southeast region, which has approximately 2% of the population (Luthje et al., 2006; Selmes et al., 2011). Many studies to date on supraglacial lake drainage have focused their attention on the southwest region (e.g. Bartholomew et al. (2011b); Das et al. (2008); Liang et al. (2012); Sundal et al. (2009)). Between 2005 and 2009, Selmes et al. (2011) calculated the mean lake size of all lakes larger than 0.0625 km^2 across the GrIS as 0.80 km^2 . The largest lake had an area of 16.8 km^2 . As a percentage of surface area in the SW region, supraglacial lakes cover less than 1% of the ablation zone (Luthje et al., 2006). In-situ measurements of lake depth record a maximum depth of 11.5m (Box and Ski, 2007), with more typical lake depths values reported in the literature being between 3m and 5m (Box and Ski, 2007; McMillan et al., 2007; Tedesco and Steiner, 2011).

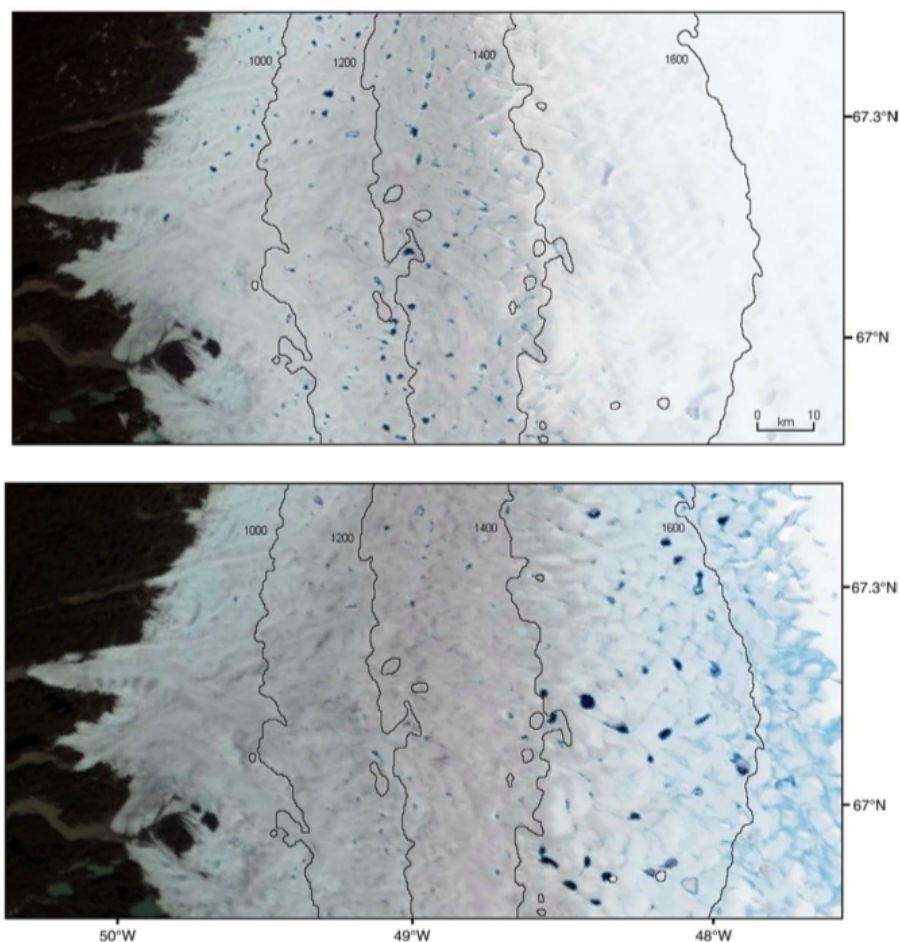


Fig. 2.3 MODIS true color images showing the difference in supra-glacial lake location and size between day 162 (above) and 199 (below) on the Western Coast of Greenland during the 2003 melt season. [Reprinted from Sundal et al. (2009)]

Lakes form on the surface of the GrIS through accumulation of surface meltwater in topographic depressions (e.g. Banwell et al. (2012a); Selmes et al. (2011)), and deepen due the increased melting rate at the lake bottom versus that of bare ice (Tedesco et al., 2012). Lake location is influenced by bedrock topography, and they appear in similar locations annually instead of advecting with the ice (Echelmeyer et al., 1991; Selmes et al., 2011). Studies reveal a seasonal and spatial evolution of lake development (Figure 2.3), whereby lakes form low on the GrIS early in the melt season, and fill at progressively higher elevations as the melt season progresses (Arnold et al., 2014; Sundal et al., 2009). A similar temporal and spatial up-sheet progression of lake drainage is observed (Sundal et al., 2009) and modelled (Arnold et al., 2014).

Supraglacial lake drainage is a widely documented phenomena (e.g. Banwell et al. (2012a); Das et al. (2008); Liang et al. (2012); Tedesco et al. (2013a)). Selmes et al. (2013) observed a mean of 263 drainage events per year across the GrIS between 2005-2009 in MODIS imagery, 61% of which were in the SW region, and only 1% were in the SE region. Drainage of supraglacial lakes is known to occur by two different mechanisms, which are characterized by their drainage rates. Slow drainage is characterized by a lake overflowing over the ice surface, resulting in an outlet channel being incised into the ice surface through which the lake drains. Fast drainage is characterized by hydrofracturing beneath a lake, which results in the lake being drained from underneath through the resulting fracture and moulins (Tedesco et al., 2013b). Fast drainage is hypothesized to be promoted by water drainage to the ice-bed interface through nearby moulins and crevasses, leading to tensile stresses beneath the lake, which then allows for hydrofracturing (Stevens et al., 2015). The timescale of slow-drainage is approximately 24hrs to a few days, while fast drainage occurs on the scale of a few hours (Tedesco et al., 2013b). Of the lake drainage events between 2005-2009 reported by Selmes et al. (2013), approximately 13% drained rapidly, approximately a third drained slowly, and approximately half did not drain and froze at the end of the melt season (Figure 2.4). It was also observed that lakes did not necessarily terminate by the same mechanism each year Selmes et al. (2013).

Over the last decade, there has been a substantial inland expansion of supraglacial lakes on the order of hundreds of meters to tens of kilometers (Howat et al., 2013). During warmer years the median elevation of lakes has been shown to increase, with drainage events occurring both earlier in the season, and at a higher frequency (Liang et al., 2012). Whether the additional melt during warmer years results in larger lakes forming is unclear. Liang et al. (2012) found no strong correlation between the two, while Sundal et al. (2009) report an increase in the total peak lake area with an increase in total melt.

In an increasingly warmer climate, the trend of supraglacial lakes forming at higher elevations is expected to continue. (Liang et al., 2012; Luthje et al., 2006; Sundal et al., 2009). However, the impact of gentler slopes and reduced surface topography due to thicker ice masking bed topography at higher elevations on lake formation and lake drainage is not well understood (Liang et al., 2012; Selmes et al., 2013). It may be that there is an upper limit to lake formation due to these physical characteristics (Liang et al., 2012). Selmes et al. (2013) report that lakes at the highest elevations tended to terminate by freezing at the end of the season, with only a very limited number terminating by fast drainage due to the shorter melt season at higher elevation. Slow lake drainage can also be expected to be inhibited at high elevations, as small surface gradients and low water throughput are unfavourable for outlet channel growth. Currently available data does not show whether lakes at progressively higher elevations will result in surface-to-bed connections at higher elevations (Selmes et al., 2013). Poinar et al. (2015) suggest a likely upper limit of $\sim 1600\text{m}$ elevation for the formation of moulins/lake hydrofracture based on strain rates from mean winter velocities. It is important to note, however, that ice acceleration during the summer will lead to a different strain pattern than during the winter months, which could allow for hydrofracture at higher elevations.

Models of the supraglacial hydrological system based on the routing of water along a DEM have been applied to alpine glaciers (Arnold et al., 1998; Flowers and Clarke, 2002, e.g.), ice caps (e.g. Clason et al. (2012)), and the GrIS (e.g. Banwell et al. (2012a)). However, they have limited functionality for modelling surface to bed connections such as moulins and crevasses, as well as slow lake drainage, preventing their generalized application to the GrIS.

Clason et al. (2012) applies a physically based routing algorithm to investigate surface to bed connections on the Devon Ice Cap, in Northern Canada. Lakes form in boundaries prescribed from Landsat imagery and surface to bed connections are modeled in DEM cells based on a comparison of tensile stresses and crevasse locations. Surface tensile stresses are calculated from surface velocities, and then used to calculate the Von Mises stress. By comparing the Von Mises stress distribution to observed crevasse distribution, a threshold stress criterion was determined. In the model, cells which have a Von Mises stress greater than the criterion capture all water that flows into them. When the volume of water captured in a cell is sufficient to propagate a fracture to bed, a surface-to-bed connection is formed. Similarly, when the volume in a lake reaches a similar threshold, it simulates hydrofracturing and a surface-to-bed connection is formed.

Leeson et al. (2012) apply a surface routing model to a DEM to investigate characteristics of surface lakes. The model is driven with a regional climate model, and predicted lake

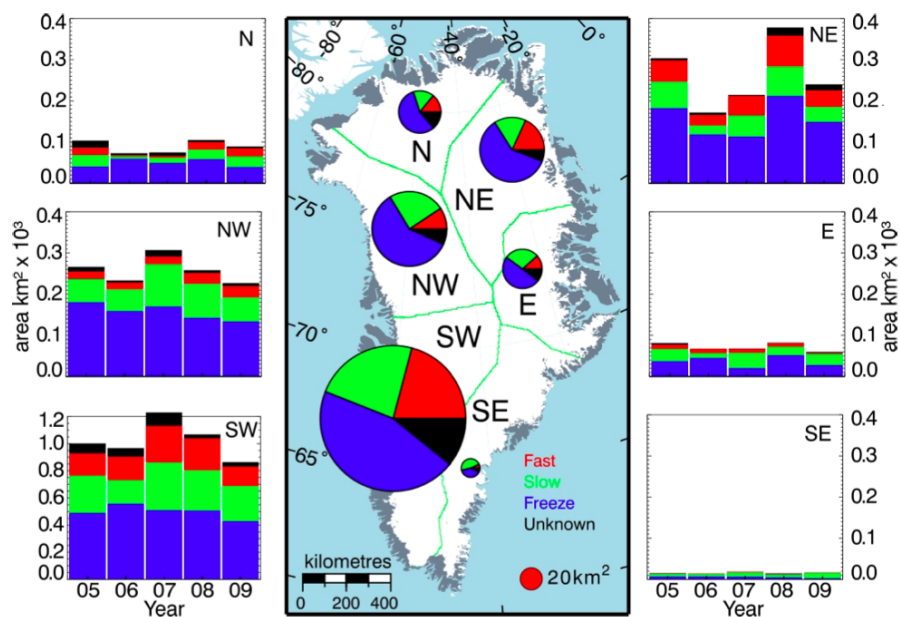


Fig. 2.4 The distribution of lake drainage types on the GrIS. Lakes are represented by maximum surface surface area in each year. The central figure shows the mean area of lake types over the period area in each year. The central figure shows the mean area of lake types over the period 2005?2009. The bar charts show the area and proportions of lake drainage type per year. Fast-draining lakes (red), slow draining lakes (green), and freezing lakes (blue) are shown. Lakes of unknown drainage type are also shown (black). Note that a different vertical scale is used for the SW bar chart for clarity. [Reprinted from Selmes et al. (2013)]

locations and surface areas are compared to lakes observed in MODIS imagery. Because neither surface to bed connections nor lake processes were simulated, the authors report an upper bound for the number of lakes, surface area, and lake volume for their study site in Western Greenland.

Progress towards an integrated model began at SPRI with the development of the Surface Routing and Lake Filling Model (SRLF) by Dr. Neil Arnold, which is described and applied to the Paakitsoq region (Figure 2.5) in Arnold et al. (2014); Banwell et al. (2012a, 2013). Model input consists of a surface Digital Elevation Model (DEM), a corresponding bed DEM (or ice depth), an hourly snow cover time series, and an hourly melt runoff time series. Melt water is routed along the surface, forming lakes in depressions, or running off of the edge of the model. Using a critical threshold parameter dependent on lake volume and ice depth, the model allows lakes to hydrofracture and form a surface-to-bed connection. The modelling of hydrofracture is based on linear elastic fracture mechanics (LEFM), described and applied to ice sheets in van der Veen (2007). This connection can remain for the duration of the melt season, and melt within a lake's watershed will exit the system through the connection. With this model formulation, water can either: run off the edge of the ice sheet, exit through a moulin caused by lake hydrofracture, or be stored in a lake.

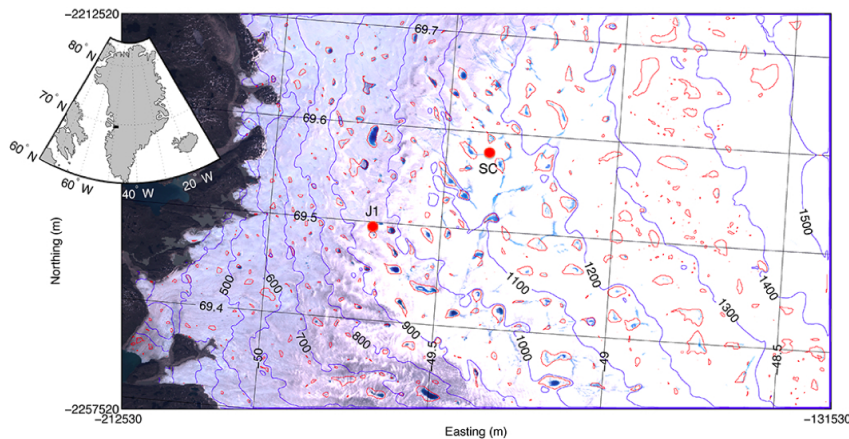


Fig. 2.5 Location map of the Paakitsoq Region. Detailed map shows Landsat true-colour image for 7 July 2001. Red lines show maximum possible lake extents calculated from the DEM in Arnold et al. (2014). Black rectangle in inset map shows study area location within Greenland. Red circles show locations of JAR-1 (J1) and Swiss Camp (SC) GC-Net stations [Reprinted from Arnold et al. (2014)]

The model is implemented using an explicit numerical method. Standard model runs use a DEM of 90m resolution, and a time step of one hour. An explicit method with these spatial and temporal resolutions were selected in order to constrain computational cost. Since model

validation is based on lake drainage events observed in satellite imagery, where the time of lake drainage is constrained to a specific day, time dependence of the solution is not expected to be a limiting source of error.

The SRLF model currently has limited functionality to model surface-to-bed connections. Surface-to-bed connections are only allowed following hydrofracture of lakes, with neither moulins nor crevasses specifically modeled. In Arnold et al. (2014), the SRLF model is run over a 30kmx40km area in the Paakitsoq region. A surface feature map from the Greenland Geological survey from 1985 reveals that a large portion of that area is crevassed, and Colgan et al. (2011b) report that the crevassed area has increased by 10% since then. Similarly, Phillips et al. (2011) report the locations of 318 moulins over a similar study site. Since crevasses and moulins decrease the amount of water available for surface lakes to form, and prevent lake formation in parts of the study area, the SRLF model overestimates the number of lakes, and the volume of water that can be routed into lakes. Current model functionality allows water from lakes to overflow, but does not allow channel incision and a positive feedback for lakes to drain slowly. Since Selmes et al. (2013) report that approximately a third of lakes drain through slow overflow, a similar number of lakes in the model may be incorrectly modelled.

Modelled lake volumes and lake locations were compared against data from Landsat imagery in Arnold et al. (2014) as validation of the model. Depending on the band ratio chosen to identify lakes in remote imagery, either 179 of the 225 observed lakes had centroids in predicted lake locations, or 252 of 505 observed lakes had centroids in predicted lake locations. Lake volume performance was reported as good, with performance depending on the threshold used for lake hydrofracture drainage.

Physical modelling of the supraglacial system is complimentary to remote sensing. While remote sensing is limited by image resolution, cloud cover, and temporal resolution, physical modeling heavily relies on the accuracy of the input DEM and melt input. However, physical models are heavily dependent on remotely sensed data for calibration. Ground based datasets such as proglacial discharge have been used, but are subject to high uncertainty and are available in a very limited number of locations.

Supraglacial lake datasets can be compiled from Landsat, MODIS and ASTER datasets using both automated and manual methods. Leeson et al. (2013) compared lake areas derived from ASTER data (Figure 2.6) using manual tracing methods and lake areas from MODIS data using automated methods. The root mean square deviation in lake area between the manually delimited results and the automated methods presented in Sundal et al. (2009) and Johansson et al. (2013) was 0.39km^2 and 1.47km^2 respectively. Fitzpatrick et al. (2014) reports a 15% error in lake volume derived from semi-automated digitized MODIS imagery

combined with an empirically derived depth-reflectance relationship. Limitations in remote sensed lake identification include mis-categorization of ice covered lakes, and the difficulty of categorization of lakes in MODIS less than 0.1km^2 due to pixel size (Sundal et al., 2009).

Hydrological modelling of slow drainage of supraglacial lakes is important to model since approximately a third of lakes drain through this mechanism (Selmes et al., 2013). The modelling of slow lake drainage and channel incision at the lip has been approached analytically by Raymond and Nolan (2000), and more recently by Kingslake (2013). Whether a lake drains through channel incision depends on the slope, water temperature, lengthscale over which heat dissipates from the water to the ice, and lake volume. Raymond and Nolan (2000), apply their model to surface lake in Alaska, and were able to fit their model to an observed slow lake drainage. However, their model has not been tested on variety of lake hypsometries. To apply their method to a large study area, it is necessary to carefully consider an appropriate choice of water temperature, and the lengthscale over which heat dissipates from the water to the ice in open channel flow. A limitation of both Raymond and Nolan (2000) and Kingslake (2013) is that the width of the outlet channel is fixed, and channel initiation is not modelled.

2.3.2 Englacial Hydrology

Moulins, crevasses, and fractures serve as pathways for water transport between the supraglacial and subglacial components of the hydrological system. Understanding the spatial and temporal characteristics of water delivery to the base enhances our ability to predict the impact of surface melt on water pressure and storage at the base, key variables in predicting the evolution of the subglacial hydrological system.

Crevasses form in regions of tensile stress, when the net stress intensity factor exceeds the ice fracture toughness (Nye, 1952; Van der Veen, 1998). In a study of the Sermeq Avannarleq ablation zone in Western Greenland, Colgan et al. (2011b) found that there is little overlap between regions occupied by crevasses, and regions occupied by supraglacial lakes and streams. In the same study, the extent of crevassing in the region is reported to have increased $13 \pm 4\%$ between 1985 and 2009. This expansion has been attributed to: a) increase in melt supply which propagates hydrofracture; b) an increase in surface slope in the ablation area; c) dynamic thinning of the ablation zone (Colgan et al., 2011b).

Moulins are deep vertical shafts in glaciers, often fed by supraglacial streams. As water flows through moulins, potential energy is converted to heat through friction, melting the ice walls. This outward growth is counteracted by the inward creep of ice (Cuffey and Paterson, 2010). Ice-radar survey data and theoretical consideration by Catania and Neumann (2010) show that moulins can persist for several seasons. This suggests that glaciers can contain

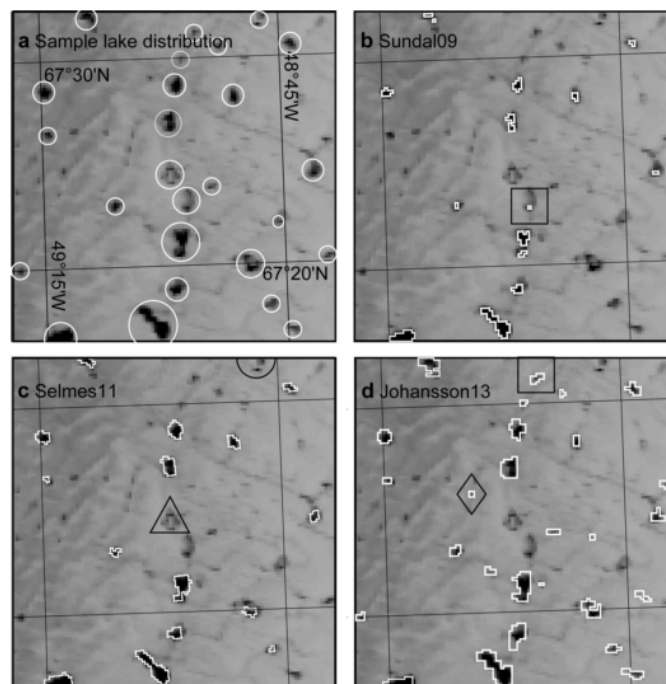


Fig. 2.6 Comparison of manually and automatically derived lake distributions on 14 June 2005 (day 165) in a small subsection of the study region. Background is the original MODIS image. In (a) circles surround SGLs identified manually. Squares in (b) and (d) illustrate lakes reported in a single dataset. In (c) the triangle indicates an ice-covered lake and the semicircle indicates an ice-free lake, neither of which is identified by any of the three automatic lake detection algorithms. The diamond in (d) indicates a reported lake that has been identified as a false positive. [Reprinted from Leeson et al. (2013)]

persistent and well developed conduit systems (Catania and Neumann, 2010). Conditions that favour moulin formation are: a) thinner ice b) warmer surface temperature c) large water supply d) previous crevassing (Catania et al., 2008; Phillips et al., 2011). Moulins are most common in the ablation zone, where there is a strong correlation between their distribution and elevated tensile stresses (Catania et al., 2008). There is only a moderate correlation between moulin distribution and supraglacial lake locations, which supports Selmes et al. (2013) findings that the majority of lake drainages are due to the slow drainage mechanism.

A study by Fountain et al. (2005) on a small glacier in Sweden found that the body of the glacier contained a network of hydraulically connected fractures. Of the 48 boreholes drilled on the glacier, about 80% intercepted a cavity, and approximately 50% hit more than one cavity. Cavities were observed at all depths. Using video cameras and dye tracers, Fountain et al. (2005) determined that many cavities were hydraulically connected, with water flowing at a slow rate ($.5\text{cm s}^{-1}$ - 4cm s^{-1}). Due to the slow rate of water flow, frictional melting of ice walls would not generate sufficient heat to maintain the cavities. The source of the cavities was hypothesized to be advected surface crevasses, and fractures within the ice. Both the drilling and ice radar survey of the glacier indicated that these cavities were widespread (Fountain et al., 2005).

Recent analysis of remote sensing data has begun revealing patterns of surface distribution of the interface of englacial and subglacial features (Colgan et al., 2011b; Liang et al., 2012; Phillips et al., 2011; Selmes et al., 2011). However, our means to investigate englacial distribution of features is limited. Ice radar surveys and borehole drilling reveal localized results, and are expensive to conduct at a widescale. The composition of the englacial system is important to understand, as moulins are thought to rapidly deliver water to a point at the base, while crevasses have the potential to dampen time-varying input oscillations (Colgan et al., 2011b; McGrath et al., 2011).

Crevasses occur when stresses in the ice exceed a threshold. Surface stresses in the ice can be derived from surface velocities obtained through remote sensing such as InSAR (e.g. Clason et al. (2012)), or from numerical models (e.g. Albrecht and Levermann, 2014). Failure criterion used include the von Mises yield criterion (Vaughan, 1993), maximum shear stress criterion (Vaughan, 1993), and a criterion based on linear elastic fracture mechanics (Van der Veen, 1998). The failure threshold can be determined by comparing the failure criterion to a known distribution of crevasses in a similar area. However, this approach does not model advection of crevasses.

The penetration depth of a crevasse is determined by the net stress, which is the superimposition of the effects of the tensile stress, the weight of the ice, and the water pressure if the crevasse contains water (van der Veen, 2007). Using a linear elastic fracture mechanics

model, van der Veen (2007) reported that water filled crevasses could penetrate to the base of glacier. Applying similar techniques to the hydrofracture beneath surface lakes, Krawczynski et al. (2009) provided volumetric constraints on the water necessary to fracture through 1km of ice; they calculated that a lake with diameter 250-800m and depth 2-5m would be sufficient to drive a crevasse to the base of an ice sheet 1km thick. Models based on the LEFM model developed by Van der Veen (1998) have been applied by Banwell et al. (2013), Arnold et al. (2014), and Clason et al. (2012) to determine surface to bed connections.

Crevasse fields precondition the ice for moulin formation. As the ice is advected downstream, the thermal energy of meltwater and heat generated from friction allows a moulin to form even if the crevasse closes due to compression. However, there is no physical model available in the literature to predict where moulins form. Phillips et al. (2010) present a model based on fuzzy logic to predict the location of moulins. This model is based on statistically relating the parameters of a DEM, specifically aspect, slope, and elevation, to the known locations of moulins over a study area. On the assumption that the relationship holds outside the study area, the model can be used to predict the likelihood a DEM cell in a similar area contains a moulin.

Modelling of connections between the surface and the bed has been limited, despite being an important component of the hydrological system (Fountain and Walder, 1998). Because of the sparsity of direct observations, moulins and crevasses are often treated as reservoirs with idealized geometries (e.g. Colgan et al., 2011b; Flowers and Clarke, 2002). Models also have incorporated englacial water storage connected to the basal hydrological system in the form of bottom crevasses with idealized geometries, or an englacial aquifer based on an ice void ratio (Flowers and Clarke, 2002; Werder et al., 2013).

2.3.3 Subglacial Hydrology

Water drains along the ice-bed interface through the subglacial hydrological system, modulating ice velocities through changes in water pressure. The overall direction of water flow in the system is determined by the hydraulic gradient, which is a function of water pressure and elevation potential. These are controlled by the surface topography, and to a lesser extent, the bed topography (Shreve, 1972). Two broad categories of glacier hydrological system are predicted to evolve beneath glaciers: a channelized system, and a distributed system. The channelized system is comprised of channels (Figure 2.7a) incised into the overlying ice (Rothlisberger or R-channels) or channels into the bedrock or sediments (Nye or N-channels). A distributed system can consist of a water sheet (Creys and Schoof, 2009; Weertman, 1972), flow through permeable sediments (Shoemaker and Leung, 1987), or connected system of cavities (Figure 2.7b) that form on the lee side of bedrock bumps

(Kamb, 1987; Walder, 1986). Spatial and temporal transitions between the drainage configurations occur in response to changes in water input (Schoof, 2010; Werder et al., 2013). Our understanding of these configurations is largely based on theoretical work, and observation from alpine glaciers. The degree to which we can apply this model to the GrIS is still a current field of research.

Channelized systems drain water efficiently compared to the relatively slow distributed system. An important distinction between channelized drainage and distributed types of drainage is that channelization typically leads to a reduction in water pressures. Water pressure varies inversely with flux in channels, leading to larger channels growing at the expense of smaller channels. This creates an arborescent network of channels at the bottom. In both linked-cavity drainage and sheet flow, water pressure is proportional to water flux. Observations show that distributed drainage exists during periods of low water flux, and as melt water input to the system increases (i.e. spring/summer), water flow localizes into channels (Cuffey and Paterson, 2010).

The dynamic nature of the subglacial hydrological system means an increase in average water input to the base does not necessarily increase water pressures. This is because a distributed subglacial system can channelize in response to increased meltwater input, and channelized systems have decreasing water pressures with increased flux. Higher water pressures occur when the rate of water input to the system overwhelms the capacity of the current system. Thus, variability in water supply to the base is thought to drive ice velocities, rather than the total volume of melt to the base (Schoof, 2010).



Fig. 2.7 The physics of channels (a) and cavities (b). [Reprinted from Schoof (2010)]

At the beginning of the melt season, the hydrological system of Greenland is thought to be in a distributed system. In the initial stages of the melt season, water input to the subglacial system is predicted to raise water pressures and increase discharge. As melt input increases, and melting occurs at progressively higher elevations, channels are thought to form first near the ice margins. This leads to reduced water pressures beneath the ice sheet. These channels are thought to expand upglacier with the progressing melt season in a manner similar to alpine glaciers (e.g Sharp et al. (1993)). At the end of the melt season, when water

input decreases, channels will not be able to sustain themselves, and inward creep of ice will close the channels. During the winter season, the subglacial hydrological system is thought to revert to a distributed drainage system. It is unknown whether some parts of a channelized system survive the winter.

Conditions at ice sheet margins are more favourable for channelization than inland. Thinner ice reduces creep closure rate, while higher discharge and steeper gradients increase melting of channel walls. Evidence from dye tracing experiments (Chandler et al., 2013; Cowton et al., 2013) on land terminating glaciers in Greenland supports the hypothesis of a transition from distributed to channelized hydrological system through the melt season. Chandler et al. (2013) report development of channelized drainage up to 41km from the margin, where ice depths are approximately 1km. In contrast, Meierbachtol et al. (2013) found no evidence for high-capacity basal melt channels from 10 boreholes drilled 17km and 34km inland. However, the probability of a borehole directly intercepting a channel is low, especially with a limited number of boreholes. Further, Andrews et al. (2014) argue that there are spatial-temporal patterns of connectivity within the subglacial hydrological system. They argue that parts of the subglacial hydrological system may remain hydraulically isolated through the melt season, or may only intermittently become connected.

A variety of hydrological models have been developed in the literature. However, the majority containing both channelized drainage and distributed drainage have been zero-dimensional box models or one dimensional flowline models (Werder et al., 2013). Many two dimensional models have assumed only channelized drainage (e.g Banwell et al., 2013), or distributed drainage (e.g. Flowers and Clarke (2002)). Arnold and Sharp (2002) presented a 2D model containing both distributed and channelized drainage, but this was limited in that only one of the components could be active at a time.

Following observations of the GrIS suggesting a feedback between surface melt and ice sheet acceleration, efforts were made to develop a two dimension model able to model both systems, and the dynamic switch between the two. Schoof (2010) developed a 2D network model in which grid edges model both linked cavities and channels. Using an idealized model geometry and synthetic input, Schoof (2010) found that acceleration due to increasing steady supply of water input to the subglacial system is suppressed by channelization. However, variation in melt supply leads to spikes in water pressure, and can lead to faster ice flow. This suggests rain events, large diurnal cycles, and lake drainage events are important to account for in future models.

A limitation of the Schoof (2010) model is that water flow occurs only on network edges. Two similar models have been created recently, which allow distributed flow through a continuum approximation across the whole model, with channel formation confined to

network edges. While mathematically similar, Werder et al. (2013) selects an unstructured mesh, while Hewitt (2013) uses a grid mesh with channels allowed on both network edges and diagonally across cells.

In Hewitt (2013), the model is applied to understanding the impact of melt to the subglacial system near the margin of the GrIS. The model broadly conforms with observations (it is run with idealized geometry and synthetic input rather than modelling a specific site), with greatest speedup predicted in early summer. Contrary to some observations, Hewitt (2013) indicates that while channelization does offset early summer speedup, increased melt will lead to an increase in annual velocities. This is because channelization occurs near the margin, and is suppressed inland. Hewitt (2013) reports that accounting for variability in melt input only slightly increases mean annual velocities.

Werder et al. (2013) also run a model with an idealized geometry and synthetic data to investigate model sensitivities, and then applies it to an alpine glacier. Important new findings from the model include: 1) Channelization does not necessarily lead to lower pressures, as channels can lie on pressure ridges leaking discharge into a distributed system. For time varying-input, water pressure may exceed that of the surrounding system at high water inputs into the channelized system. 2) Channels often lay oblique to the pressure gradient in the direction of the bed slope, due to enhanced heat dissipation in downward sloping channels.

Both models acknowledge deficiencies including: inability to deal with sudden large water inputs, extended periods of high water pressure, channel formation depending on grid formulation, as well as more theoretical issues, such as whether averaging out water pressure over cells is appropriate, or the the assumption that channels are always full. Whether modelling of the subglacial system in Greenland requires channelization is not universally accepted, as Bougamont et al. (2014) argued that modelling the subglacial system as a till layer results in good agreement with GPS velocities.

Fundamentally, the subglacier system is difficult to study due to the sparsity of available observational data. What data is available is either point measurement (borehole), or integrated over time and space (dye tracer experiments). Spatial and temporal variations in connectivity, bed properties, and water input are all poorly constrained.

2.4 Ice Dynamics

The presence of water at the base of glaciers impacts basal shear stresses. Higher water pressures reduce ice-bed coupling and lead to increased basal sliding. Ice velocities on the GrIS are observed to increase during periods of high water availability, with local acceleration

during rapid lake drainage events, and widespread acceleration in the ablation zone during the melt season.

High water input over short time periods via supraglacial drainage events result in localized short term, high magnitude, horizontal and vertical velocity fluctuations (Das et al., 2008; Tedesco et al., 2012). Ice velocities as high as 1500% of pre-drainage speeds have been observed during rapid lake drainage, and velocity increases of 400% have been recorded during slow drainage of a lake into a moulin (Tedesco et al., 2012). Following rapid lake drainage events, ice velocities have been reported to both return to previous speeds (Das et al., 2008) and remain 50-100% above pre-drainage speeds (Tedesco et al., 2012). This may depend on whether following lake drainage events, the surface-to-bed connection drains a large enough area to keep a moulin open for the rest of the season (as suggested by Banwell et al. (2013)).

During summer, ice velocities in the ablation zone of Western Greenland increase up to 220% of their winter background (Bartholomew et al., 2010; Joughin et al., 2008; Shepherd et al., 2009; van de Wal et al., 2008; Zwally et al., 2002), with speed up progressing up glacier through the melt season (Bartholomew et al., 2010). Measurements of ice velocities show summer velocity increases extending to at least 60km upglacier (van de Wal et al., 2008), with the magnitude of speedup attenuating upglacier (Sole et al., 2013).

Ice velocities are observed to increase early in the melt season, while during the later part of a melt season there is an observed slowdown. This is hypothesized to be controlled by the switch from a distributed to channelized system, and the resulting reduction in water pressure (Bartholomew et al., 2010, 2011a; Fitzpatrick et al., 2013; Schoof, 2010; Sundal et al., 2011). Understanding the impact changing patterns of surface melt on subglacial hydrology, and hence, ice velocities is important to constraining the future contribution of the GrIS to sea level rise. In particular, the connection between surface melting and mean annual velocities is of interest due to the potential for positive feedback.

In a comparison of ice velocities on six glaciers over five years to modeled surface runoff, Sundal et al. (2011) report that although peak rates of ice flow correlate with the amount of melting, mean summer velocities do not (Figure 2.8). Rather, warmer years result in a slower mean ice flow over the summer, as the measured period of increased ice velocities is approximately three times shorter than in colder years. In contrast to Sundal et al. (2011), Sole et al. (2013) report a positive correlation between melt and ice flow during the three years of the study period. However, there is no significant correlation between surface melt and annual ice displacement. Sole et al. (2013) hypothesize that years with greater melt have a larger channelized system, resulting in more extensive drainage of the subglacial system, preconditioning the bed for slower winter velocities by causing a net reduction in water

pressures. Hence, while Sundal et al. (2011) suggest that slower mean annual velocities are the result of slower summer mean velocities, Sole et al. (2013) argue that the reduced mean annual velocities are the result of reduced winter mean velocities.

Two decadal time-scale observational studies suggest that increased melt does not increase annual ice flow at low elevations. A long-term (1985-2013) annual velocity dataset has also been derived from Landsat imagery using a feature tracking methodology (Tedstone et al., 2015). The study area was a predominately land-terminating region of Southwest Greenland, covering 170 km of the margin and extending ~ 50 km inland to approximately 1100 m elevation. Tedstone et al. (2015) report that despite a 50% increase in meltwater production over the area over the time period, mean annual ice velocities decreased by 12% from 1984/1985 to 2007-2014. In contrast to van de Wal et al. (2008), Tedstone et al. (2015) determine that while changes in ice thickness and slope can potentially account for slowdown within 10 km of the margin, between 10-50 km the changes in ice geometry can only account for up to 50% of the observed change in ice velocity.

An analysis of 17 years of ice velocity data derived from GPS measurements by van de Wal et al. (2008) found a 10% decrease in the mean annual ice velocity over the time period 1990-2007. Mean annual velocities were not correlated with annual ablation, and van de Wal et al. (2008) hypothesize that the decrease in ice velocity can be attributed to decreases in ice thickness or decreases in surface slopes. An extended analysis of the same area with the time series extended by three years is presented in van de Wal et al. (2015). The authors report that ice velocity response to summer melting depends on elevation. In the lower ablation zone, mean annual velocities are not significantly correlated to summer melt. In the upper ablation zone however, increased summer melt leads to decreased annual velocities due to a decrease in mean winter velocities (consistent with Sole et al. (2013)).

An exception to this pattern occurs in the study area at the highest GPS station, which is located at 1850 m elevation, 140 km from the ice margin, and ~ 40 km into the accumulation zone (Doyle et al., 2014; van de Wal et al., 2015). At this GPS station, Doyle et al. (2014) report an increasing trend of summer, winter, and annual ice velocities from 2009-2013. Both Doyle et al. (2014) and van de Wal et al. (2015) hypothesize that velocities increases at this station were driven by increased water drainage to the ice-bed interface at greater distances from the margin. Hence, they caution against extrapolating the results from the ablation zone into the interior of the ice sheet, as thicker ice and shallower surface slopes suppress channel formation.

Modelling summer ice flow of the GrIS is challenging as spatial and temporal patterns in ice velocities result from coupling between surface processes, basal hydrology, and ice dynamics. Knowledge or simulation of each of these components is required. Marine-

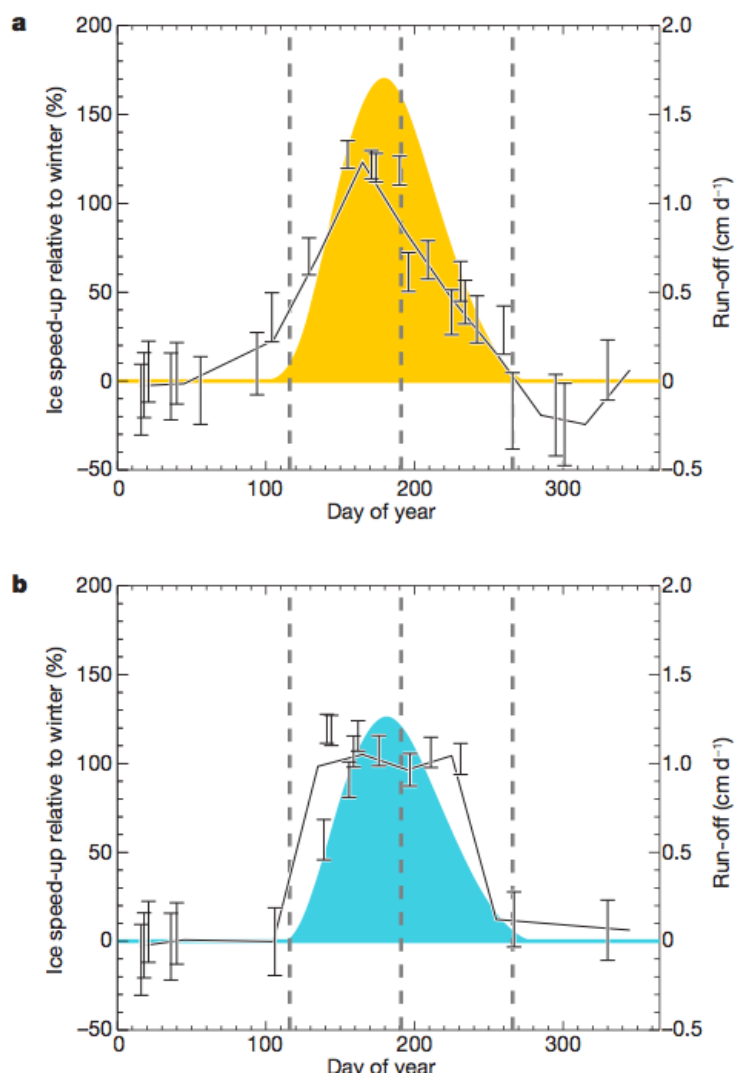


Fig. 2.8 Ice speed-up relative to winter during years of high and low surface melting. a) Speed-up in years of high melting (1995 and 1998). b) Speed-up in years of low melting (1993, 1996 and 1997). Point data are 35-day ice-velocity averages relative to the winter mean within the elevation band 500-600m above sea level from three glaciers and the elevation band 400-500m above sea level from one glacier. Error bars show the one-sigma uncertainty of speed-up measurements at each epoch. Monthly averaged data are shown as solid lines. Also shown (in colour) are model estimates of daily surface run-off rates within the study area averaged during the years of high (orange) and low (blue) melting. Vertical dashed lines indicate the shoulders and midway-point of the run-off period, which are used to define the summer period over which average speed-up is calculated [Reprinted from Sundal et al. (2011)]

terminating sectors of the GrIS present additional challenges compared to land terminating sectors, due to complex ice-ocean interactions at their terminating edge. It is important to note that much of the theory applied to land-terminating sectors of the GIS results from extending previous work on alpine glaciers. We present work about these two systems somewhat interchangeably due to their similarity, in contrast to marine terminating glaciers or Antarctica. However, the extent to which alpine glaciers can be used as an analogue for land-terminating sectors of the GrIS is unclear due to the difference in scale.

Integrated models have a long history in the glaciological literature. A detailed review focused on subglacial hydrology models, including their integration with ice flow and surface hydrology is found in Flowers (2015). Here, we limit our discussion to a brief overview of approaches to coupled modelling, recent advances applicable to alpine glaciers and land-terminating section of the GRIS, and those studies applied to the Russell Glacier area of western Greenland.

A variety of simplifications are used to make modelling the coupled ice flow problem more tractable. These include: 1) reducing the problem to a 1-D flowline (Colgan et al., 2011a; Pimentel et al., 2010); 2) modelling using an idealized domain/geometry (Hewitt, 2013; Hoffman and Price, 2014); 3) neglecting one of the components of the system (e.g. ice flow, (Banwell et al., 2016; de Fleurian et al., 2016)).

Individual components of the coupled system have been modelled with a variety of approaches and assumptions. Banwell et al. (2016, 2013) apply the SRLF model described previously. de Fleurian et al. (2016) mapped moulin locations and delineates catchments from observed supraglacial rivers in a Landsat 8 image. A routing model is then applied to route water to the identified moulins, with runoff predicted using RACMO2.3. Although this approach neglects lake drainage events, manually mapping moulins allowed for accurate spatial input to the ice-bed interface. In contrast, Bougamont et al. (2014) focuses on lake hydrofracture events, and use a time series of observed lake drainage events as supraglacial input to the bed.

Basal hydrology can be simplified by assuming that only channels exists, and prescribing the network morphology. (Banwell et al., 2016, 2013; Colgan et al., 2011a). Bougamont et al. (2014) assume the subglacial hydrology network is dominated by a till layer at the bottom and neglect channels. de Fleurian et al. (2016) uses a double continuum model, emulating a 'fast' and 'slow' system corresponding to channelized and distributed flow. Both Hewitt (2013) and Hoffman and Price (2014) use a subglacial hydrology component consisting of both distributed and channelized components. The limitation of Hoffman and Price (2014) is that channel initiation is not modelled. Rather, when a channel is predicted to exist, it is initiated at a size corresponding to the depth of the distributed system.

Ice flow is often simplified by omission. Banwell et al. (2016, 2013) and de Fleurian et al. (2016) assume that patterns of basal water pressure (given as either as effective pressure, or a ratio of water to overburden pressure) allow for broad interpretation of the impact of subglacial hydrology on ice flow. This approach neglects the feedbacks between basal hydrology and sliding (Hoffman and Price, 2014), and the non-local affect of longitudinal stresses. Ice flow models can also employ different level of approximations of the Stokes equations. Rather than solving the full Stokes model, the Blatter-Pattyn approximation, shallow shelf approximation, or a mixed shallow shelf/shallow ice approximation can be used. These equations allow for much greater computational efficiency, and can be justified due to a high sliding ratio at the margin of the GrIS (Colgan et al., 2012; Ryser et al., 2014). For a discussion on ice sheet models, we refer the reader to Chapter 4.

When coupling subglacial hydrology to ice sheet models, a sliding law must be selected to couple the components, providing the basal boundary condition for the ice flow model. There is no consensus in the glaciology community about a correct sliding law, and coupled models use a variety of forms. In general, the coupling between subglacial hydrology and ice flow is implemented via: a) a generalized Weertman sliding law; b) a sliding law for cavitation over a hard bedded surface; c) a sliding law based on failure of soft sediments (Bougamont et al., 2014; Hewitt, 2013).

Two papers applying coupled models to the Russel Glacier region have been recently published. Although papers differ in their approach, both Bougamont et al. (2014) and de Fleurian et al. (2016) report good matches to observations. Bougamont et al. (2014) compare modelled velocities to data from a GPS station near the margin of the ice sheet, and multiple eleven day average velocity maps obtained through TerraSAR-X satellite data. Both datasets are for 2010. Model output compares well to both datasets, and in particular, only the very earliest speedup measured by GPS is not captured in the model. However, modelled velocities are not compared at high elevations. Since de Fleurian et al. (2016) does not incorporate an ice flow model, the authors compare their modelled water pressures to vertical GPS displacement (ice sheet uplift). Four years of model output and GPS data are compared. Data from seven GPS stations are used, ranging in elevation from approximately 200m to 1700m. Although the authors claim good agreement with GPS data, the model has difficulty capturing the behaviour at low elevations. Similarly, although for some years the predicted vertical uplift is in phase with GPS data, there are also stations which are antiphase.

The results of Bougamont et al. (2014) suggest that supraglacial lake drainage are a key driver of summer ice acceleration, and that a basal boundary condition determined by a sliding law for plastic till rheology, or a sliding law with similar behaviour for hard beds is appropriate. They find the best fit when their model is driven by supraglacial

lake hydrofracture events, or supraglacial lake hydrofracture events and differences in melt between subsequent days of melt. Driving their model with lake events and total melt input leads to divergence from GPS data. The authors suggest that mean melt would be handled by an efficient system, which is not included in their model. However, the inclusion of an efficient system may have a more complicated impact than simply handling mean melt. The results of (de Fleurian et al., 2016) may be improved by the inclusion of supraglacial lakes. However, the observed agreement at higher GPS stations suggests that supraglacial lakes can not fully explain the observed signal.

Chapter 3

Surface Hydrology

3.1 Overview

In this chapter, a current surface hydrology model (Arnold et al., 2014; Banwell et al., 2012a) is enhanced to allow water to drain into moulins outside of lake basins and crevasses. Additionally, lake drainage over the ice surface via channel incision at the lake edge is implemented. The updated model is applied in the Paakitsoq Region, Western Greenland to investigate the partitioning of meltwater into different pathways for three contrasting melt seasons. This chapter has been published in the *Journal of Glaciology* in an article titled 'Quantifying supraglacial meltwater pathways in the Paakitsoq region, West Greenland'. Coauthors on the paper are: Neil Arnold, Allen Pope, and William Colgan (Koziol et al., 2017).

This chapter is independent of Chapter 4 of the thesis. In Chapter 5, the supraglacial hydrology model developed in this chapter is interfaced with the ice flow model/inversion code developed in Chapter 4 along with a previously published subglacial hydrology model.

This chapter begins with a short overview of the contents of this chapter and their relation to other chapters. It is followed by an introduction covering surface hydrology on the GrIS. The methods section presents the study site, datasets, and updated model. The results show the partitioning of melt between different pathways in the Paakitsoq region, modelled hydrographs of lake drainage via channel incision, and a sensitivity analysis. The discussion focuses on the melt partitioning, including spatial and annual variability. The conclusions include that the model agrees qualitatively with a suite of observed behaviours, and that there is inter-annual variability in the partitioning of meltwater between different drainage pathways. The impact of inter-annual variations in melt partitioning between drainage pathways on ice velocities will depend on the configuration of the subglacial hydrological system.

3.2 Introduction

The GrIS has experienced elevated rates of melt since the 1990s (Fettweis et al., 2013, 2011; van den Broeke et al., 2009). In addition to driving surface mass loss, observations and modelling suggest that higher rates of surface melting may lead to dynamic changes of the ice sheet (Doyle et al., 2014; Hewitt, 2013; Moon et al., 2014; Tedstone et al., 2015; van de Wal et al., 2015). Correlations between the summer melt season and increased summer ice velocities indicate that surface meltwater entering the subglacial system modulates water pressures, influencing ice velocities through changes in basal drag (Bartholomew et al., 2011a; Fitzpatrick et al., 2013; Joughin et al., 2013; Moon et al., 2014; Zwally et al., 2002). Recent modelling studies of the subglacial hydrological system report that the temporal variability of meltwater input (Hewitt, 2013; Schoof, 2010) is an important control on basal drag. However, the role of the supraglacial hydrological system in determining spatial and temporal patterns of meltwater delivery to the ice sheet bed remains poorly understood. Water draining into the englacial system can be trapped in crevasses, leading to modest increases in ice velocities due to cryohydrologic warming of the ice sheet (Harrington et al., 2015; Lüthi et al., 2015; Phillips et al., 2013; Poinar et al., 2016; Van Der Veen et al., 2011).

A significant proportion of surface meltwater drains via the subglacial system, with observations at the ice margin showing the majority of water exiting through subglacial channels and only limited flow over the ice edge (Zwally et al., 2002). Meltwater enters the subglacial system via crevasses, moulins, and surface to bed connections created during lake hydrofracture events. Mapping of supraglacial stream networks in the ice sheet watershed of Leverett glacier, Southwest Greenland shows all meltwater rivers draining into the englacial hydrological system prior to reaching the ice margin (Smith et al., 2015). However, Poinar et al. (2015) predict that surface stresses limit the formation of pathways from the surface to the ice bed to below ~ 1600 m elevation; above this, observations show water draining over the ice sheet surface many kilometers downstream to lower elevations before entering a meltwater pathway.

Surface meltwater on the GrIS forms stream networks and collects in lakes. Lakes may drain slowly by incision of a channel at their edge releasing water downstream, or drain rapidly through hydrofracture to the ice-bed interface (Tedesco et al., 2013a). Hydrofracture events are hypothesized to be triggered when increased basal slip generates tensile stresses beneath lakes (Stevens et al., 2015). Since the observation that lake hydrofracture events temporarily increase local ice velocities (Das et al., 2008; Doyle et al., 2013; Tedesco et al., 2013a), much work has focused on understanding the relation between surface melt and lake distribution (Fitzpatrick et al., 2014; Leeson et al., 2013; Liang et al., 2012; Morriss et al., 2013; Selmes et al., 2011; Sundal et al., 2009).

Supraglacial modelling of the GrIS has focused on lake development and hydrofracture. Such models demonstrate that although lakes have limited storage capacity relative to annual surface melt (Leeson et al., 2012), hydrofracture events and the subsequent surface to bed connections created can transfer significant amounts of water to the bed (Arnold et al., 2014; Banwell et al., 2012a; Clason et al., 2015). To date, only Clason et al. (2015) include surface drainage other than by lake hydrofracture, applying the method developed in Clason et al. (2012) for the Devon Ice Cap. Drainage into crevasses and moulins outside of lake basins is simulated by applying a hydrofracture criterion, similar to that of lakes, to grid cells in the model where surface stresses exceed a prescribed surface tensile strength. Clason et al. (2015) report that while surface to bed connections via lake hydrofracture have the dominant role above ~ 1000 m elevation, moulins and crevasses are the key transport mechanism below ~ 1000 m.

In this paper, we enhance the surface routing and lake filling (SRLF) component of the model of Banwell et al. (2012a) and Arnold et al. (2014) to allow drainage into crevasses and moulins outside of lake basins. Additionally, we also simulate the slow surface drainage of lakes via channel incision at their edge, following Raymond and Nolan (2000), allowing water to escape from closed lake basins and potentially flow into downstream moulins, crevasses, or lakes. We apply the updated model to the Paakitsoq region of Western Greenland over three melt seasons with contrasting melt intensities, incorporating moulins identified from high resolution satellite imagery, and crevassed areas determined from surface stresses derived from mean winter velocities. Water storage in aquifers is neglected. In order to better understand surface drainage, we use the model to quantify the partitioning of meltwater draining into moulins, crevasses, and surface to bed connections from lake hydrofracture. We also investigate the spatial variability of surface drainage and the impact of higher intensity melt seasons.

3.3 Methods

The SRLF model simulates surface flow and lake formation across the GrIS. It has been previously applied to a ~ 100 km² area of the Paakitsoq region by Banwell et al. (2012a) to successfully predict the filling of a supraglacial lake. When applied over a wider ~ 3600 km² area of the Paakitsoq region, SRLF model predictions using the Greenland Mapping Project (GIMP) Digital elevation model (DEM) (Howat et al., 2015) show good agreement with observed lake depths and extents, as well as the generally observed spatiotemporal pattern of lake hydrofracture drainages (Arnold et al., 2014). Previous work with the model however, has neglected drainage into moulins outside of lake basins, as opposed to those caused by

hydrofracture, and into crevasses. We develop the model in this paper to allow drainage into these surface features, as well as to allow lakes to drain through supraglacial channel incision.

The SRLF model requires a DEM of the study area, an ice thickness map, and the locations of moulins and crevasses. The model is driven by time series of distributed melt runoff and distributed snow depth. We first discuss the formulation of the model itself, before describing the study area, and the datasets used as model inputs and driving variables. We then discuss the design of the model runs used to explore the sensitivity of the model to certain parameters, and to assess the impact of different melt season intensities on the model results.

3.3.1 Model Formulation

Water flow is modelled as Darcian flow (Eq 3.1) in a saturated layer at the base of the snowpack when snow depth is greater than 0.7 m, and as open channel flow (Eq 3.2) otherwise. From Arnold et al. (1998):

$$v_{snow} = \frac{\rho_w g k \theta}{\mu \kappa} \quad (3.1)$$

$$v_{channel} = \frac{R^{\frac{2}{3}} \theta^{\frac{1}{2}}}{m} \quad (3.2)$$

where ρ_w is the density of water, g is the acceleration due to gravity, μ is the viscosity of water, k is the permeability of snow, θ is the surface slope, κ is the porosity of snow, R is the hydraulic radius of supraglacial channels, and m is the Manning roughness coefficient. These equations determine the speed of water flow across cells. The 0.7 m snow depth threshold for stream formation is based on calibration simulations performed by Banwell et al. (2012b). A single flow direction algorithm is used to determine water routing. In this scheme, water is assumed to flow from a grid cell to the adjacent cell with the lowest elevation. For each sink cell in the model domain, the SRLF model calculates an input hydrograph by integrating the travel time of water in the cells forming the upstream catchment. Sink cells may be moulins, crevasses, lake depressions, or exit points on the lateral domain boundaries. All water entering moulins and crevassed cells is captured. We assume that these cells have either sufficient storage capacity or drain into the englacial system, and that overflow does not occur. Once water enters a sink cell, no further routing occurs. Hence there is no internal routing of water within crevasse fields. Water entering a cell denoted as crevassed is removed from the model upon entry, with the volume and timestep saved.

Depressions in the DEM collect water, forming lakes. Lake hydrofracture is modelled to occur when the volume of water in a lake is sufficient to fill a fracture penetrating the local ice thickness to the base. The length and width of the potential fracture are prescribed, using a fracture surface area parameter (F_a). The F_a parameter is constant across the whole model domain following Arnold et al. (2014). Sensitivity analysis by Arnold et al. (2014) show that a value of F_a in the range of 4000-8000 m² results in the best agreement between modelled and observed lake volumes from satellite imagery. If a lake induces hydrofracture, all additional water input into the lake depression is assumed to drain via a surface to bed connection located in the lowest cell of the depression, which remains open for the remainder of the melt season. Alternatively, a lake that is filled to capacity will route additional water into the downstream catchment; this can lead to incision of a channel at the lip, and can result in channelized supraglacial drainage.

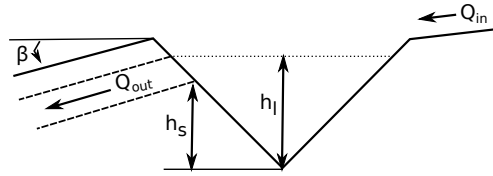


Fig. 3.1 Schematic cross-section of a lake undergoing channelized drainage, which is modelled by Equations (3.3) and (3.4), adapted from Raymond and Nolan (2000).

Analysis of supraglacial lake drainage in Moderate-resolution Imaging Spectroradiometer (MODIS) imagery by Selmes et al. (2013) shows that approximately a third of supraglacial lakes drain slowly over the surface of the ice. This is thought to occur through a channel incised at the edge of the lake into the ice by water draining from the lake (Selmes et al., 2013; Tedesco et al., 2013a). Raymond and Nolan (2000) developed a spillway model (Figure 3.1) to investigate lake drainage through such an exit channel, which we apply to lakes on the GrIS in the SRLF model. Our modelling implements Eq. 3.3 and Eq. 3.4, which describe the evolution of the channel and the lake surface height (Raymond and Nolan, 2000).

$$\frac{d}{dt}(h_s) = \frac{-\rho_w g k \beta^{1/2}}{\rho_i L} (\beta + \gamma) (h_l - h_s)^{5/3} \quad (3.3)$$

$$\frac{d}{dt}(h_l) = \frac{-k \beta^{1/2} W_s}{A_l(h_l)} (h_l - h_s)^{5/3} + \frac{Q_i}{A_l(h_l)} \quad (3.4)$$

where h_s is the height of the channel floor, h_l is the height of the lake surface, ρ_w is the density of water, ρ_i is the density of ice, g is the acceleration due to gravity, k is a channel discharge parameter related to channel roughness and cross-section shape, β is channel slope, L is the

latent heat of fusion per unit mass, W_s is channel width, Q_i is water input into the lake, and A_l is the surface area of the lake as a function of the height of the lake. The dimensionless heat transfer parameter γ is defined as $\gamma = \frac{C_w T}{gx}$, where C_w is the heat capacity per unit mass of water, T is the temperature of water in a lake above the freezing point, and x is the distance over which the water temperature drops to the freezing point in a channel. A list of model parameters is given in Table 3.1. Creep closure of the channels is neglected in this model formulation, as hydrostatic ice pressure near the surface are low. Numerical modelling of channels including creep closure is detailed in Jarosch and Gudmundsson (2012).

Description	Symbol	Value	Units
Acceleration due to gravity	g	9.8	ms^{-2}
Density of water	ρ_w	1000	kgm^{-3}
Density of ice	ρ_i	916	kgm^{-3}
Channel discharge parameter	k	10	$m^{1/3}s^{-1}$
Latent heat of fusion	L	3.35×10^5	Jkg^{-1}
Fracture area threshold	F_a		m^2
Initial Channel Depth	C_i		m
Yield Strength	σ_y		kPa
Heat Transfer Parameter	γ		
Lake Elevation	h_l		m
Channel Elevation	h_c		m
Surface area of lake	A_l		m^2
Water input to lake	Q_{in}		m^3s^{-1}
Water output from lake	Q_{out}		m^3s^{-1}
Channel slope	β		
Channel width	W_s	5	m

Table 3.1 Table of parameters and values for SRLF model simulations. The first section lists physical constants, the second section lists model parameters

The channel floor is melted due to heat dissipated from the water flowing in the channel. The model assumes two sources of heat. The first is the conversion of gravitational potential energy to heat, while the second is the thermal energy of the water exiting the lake. These are transferred to the channel floor according to the average slope of the channel and the rate of cooling of water in the channel. This is represented by the sum $(\beta + \gamma)$ in Eq. 3.3 (Raymond and Nolan, 2000).

Lakes form in depressions in the DEM, and are assumed to have an idealized conical hypsometry, the dimensions of which are derived from the topographic depression. Lakes overflow when the height of the water in the lake exceeds the lowest cell of the edge of the depression. Once a lake fills, we allow for two methods of drainage: overflow drainage and

channelized drainage. Overflow drainage refers to when water beyond the capacity of the lake is removed and routed downstream from the lake outlet without contributing to channel incision. Channelized drainage refers to when a channel forms at the lake outlet, allowing water above the channel base to drain, with drainage deepening the channel; in this case, water drains from the lake, decreasing the volume of water stored.

In the SRLF model, all lakes which do not hydrofracture have the potential to drain over the ice sheet surface. Channelized drainage is assumed to occur only if the channel elevation decreases faster than the lake water height (i.e. $\frac{d}{dt}(h_s) < \frac{d}{dt}(h_l)$). Otherwise, only simple overflow drainage is assumed to occur. Channelized and overflow drainage occur simultaneously if water drainage through a channel is not sufficient to prevent the lake surface height from rising above the limit of the topographic depression.

The model requires a fixed initial channel geometry. The initial depth is set as a model parameter, while the width is set to a fixed value of 5 m, which was selected as a representative value of the range of channel widths observed in WorldView imagery. The top of the channel is set at the elevation of the lake edge. Fixed channel dimensions are necessary since channel initiation is not modelled, and since channels in the model only incise downwards, not outwards. We use the same initial geometry for all channels in the model domain. Channels are assumed to open instantaneously once drainage begins, simulating rapid removal of blocking snow. This assumption implies that any channelization from previous years' will only have an effect up to the initial channel depth, neglecting the impact of previous years melt intensity on channel formation. Once a channel opens, the channel begins to incise following Eq. 3.3 and Eq. 3.4. Since channel drainage depends on Q_i , the method of drainage for lakes undergoing overflow drainage is re-evaluated each time step. Alternatively, if channelized drainage does not occur, excess water is removed via overflow drainage.

The change in lake height and channel bottom height are modelled using the ode15s solver in Matlab. If the lake is draining via a channel, and there is an input of water greater than the channel can discharge, causing the water volume in the lake to exceed the volume of the DEM depression, excess water is removed via simple overflow. There is no mechanism for channels to close, and all water entering a fully drained lake is routed downstream.

Following Arnold et al. (2014) we initiate each model run with a DEM devoid of water. This assumption is based on statistics from Johansson et al. (2013), who reported that for a study area south of the Paakitsoq region 78-88% of lakes below 2500 m drained during the 2007 to 2009 melt seasons. Similar to Arnold et al. (2014), we impose no-inflow boundary conditions, while allowing water to flow out of the model domain. This is justified on the eastern boundary as it extends beyond 1500 m, where melt is limited. The northern and southern boundaries of the model were selected to be approximately perpendicular

to elevation contours leading to limited outflow; modelling results (see 3.4) show that approximately 11% of surface melt generated in the study area exits through the northern and southern boundaries. Outflow from the western boundary represents water flowing off the ice sheet.

3.3.2 Study Area and DEM

We apply the SRLF model to a land terminating sector of the GrIS in the Paakitsoq region of Western Greenland (Figure 3.2). The study area is ~ 31 km in width, ~ 84 km in length, and ~ 2368 km² in area. The GIMP DEM at 90 m resolution is used as input to the SRLF model for all three melt seasons. Following Arnold et al. (2014), we smooth the DEM using a 2x2 cell median filter to remove small scale noise, and then an 11x11 cell Gaussian filter to remove the ‘terracing’ effect of the 1 m vertical resolution of the data.

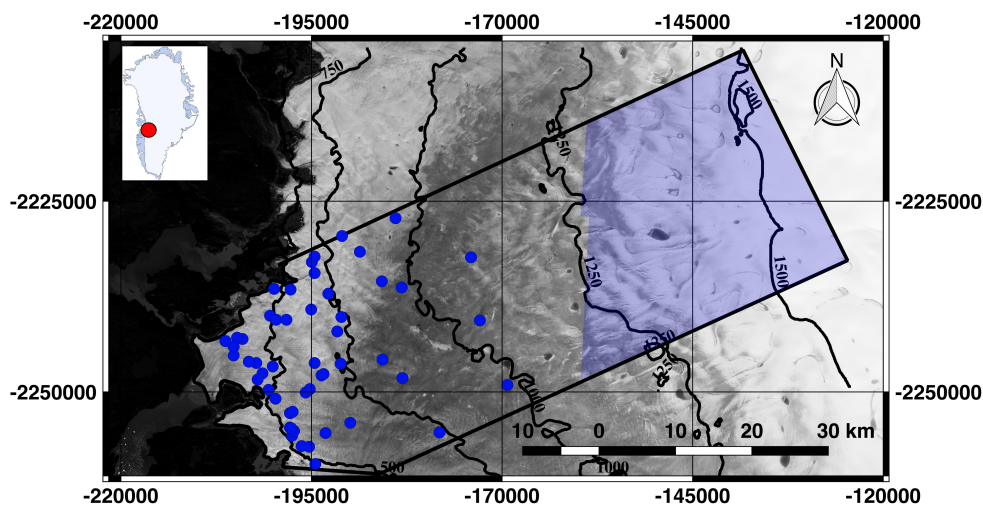


Fig. 3.2 Location map of the study area. Black outline shows the model domain, while blue markings denote moulin locations derived from WorldView imagery. Blue highlight indicates where appropriate WorldView imagery was unavailable. Base-map shows a Landsat-8 image from 4 Aug 2014; contour lines are from the GIMP DEM (Howat et al., 2015). Red dot in inset locates the Paakitsoq region in Greenland. Map projection is NSIDC Sea Ice Polar Stereographic North.

Previous work (Arnold et al., 2014) found good agreement between the GIMP DEM and observed lake locations and volumes in Landsat imagery. Since lake forming depressions are controlled by basal topography, and are not observed to advect with ice flow (Echelmeyer et al., 1991; Selmes et al., 2011), we expect the locations of lake depressions in the DEM to be valid over multiple melt seasons.

Yang et al. (2015) report that calculated stream networks from DEMs match the broad scale drainage patterns mapped from satellite imagery. Comparison of stream locations (Figure 3.3) mapped for 2009 to those in 1985 (Thomsen, 1988) over a portion of the Paakitsoq region shows that streams develop over a similar area. We therefore also expect stream locations derived from the DEM to be applicable over multiple melt seasons.

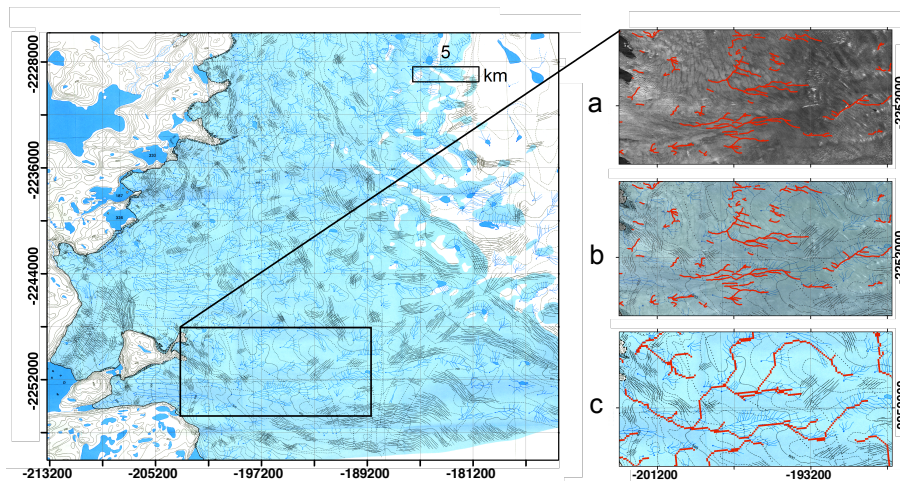


Fig. 3.3 Supraglacial hydrological features delineated within the Paakitsoq region. Main panel: Map of Paakitsoq region showing surface features, including stream locations (Thomsen, 1988). Stream positions were visually delineated from optical imagery by Thomsen (1988) Inset: a) Supraglacial stream positions visually delineated in 2009 WorldView imagery (red markings) overlain on the same WorldView image. B) Supraglacial stream positions visually delineated in 2009 WorldView imagery (red markings) overlain on the map by Thomsen (1988) highlighting coincidence of stream locations. C) Calculated supraglacial stream locations from the GIMP DEM overlain on the map by Thomsen (1988). Map projection is NSIDC Sea Ice Polar Stereographic North. [Note: This image was created in collaboration with William Colgan.]

Lake hydrofracturing can be conceptualized as dependent on the ice thickness and threshold water volume (Krawczynski et al., 2009). To determine ice thicknesses, we employ the BedMachine dataset (Morlighem et al., 2014, 2015a).

3.3.3 Crevasse and Moulin Locations

We use the von Mises yield criterion (Clason et al., 2015; Vaughan, 1993) to predict the occurrence of crevassed areas in the study site (Figure 3.4). Surface stresses derived from winter velocities (Joughin et al., 2010a,b) are used to determine von Mises stresses across the study area. Mean winter velocities are used as a dataset of annual velocities is not currently available. Surface stresses are calculated from winter strain rates using:

$$\sigma_{jk} = A^{-\frac{1}{n}} \dot{\epsilon}_e^{\frac{1-n}{n}} \dot{\epsilon}_{jk} \quad (3.5)$$

where $\dot{\epsilon}_e$ is the effective strain rate, A is a creep parameter, and n is the flow law exponent. A is assigned a value of $9.3 \cdot 10^{-25}$, corresponding to an ice temperature of -5 C° (Cuffey and Paterson, 2010). n is set to 3.

Following Clason et al. (2015), we visually compare the distribution of von Mises stress to areas of crevassing observed in satellite imagery to determine a yield strength (σ_y). Crevasses are predicted to form in cells where the von Mises stress exceeds the yield strength. A yield strength of 132.5 kPa is determined to have the best visual match between predicted crevasses and the prominent crevasse fields in the lower study area. We perform a sensitivity test using yield strengths of 125 kPa and 140 kPa, which increase and decrease the crevassed area by 32% and 25% respectively.

WorldView images acquired during the 2009 and 2010 melt seasons were visually inspected to determine moulin locations. Although these images provide good coverage of the lower and mid elevations of our study area, suitable WorldView imagery is unavailable for the uppermost region of the study site (Figure 3.2). However, since we observe moulin density to decrease away from the ice margin in the available imagery, we do not expect moulins to occur outside of lake basins in the upper region of the study site.

Moulins are identified in the imagery as the abrupt ending of a stream. Forty five moulins are identified which are located outside of topographic depressions in the DEM. The SRLF model is initialized with moulins at these locations. Moulins with locations coincident with depressions in the DEM are not used; rather, we allow the SRLF model to predict whether a surface to bed connection will form by lake hydrofracture in these locations. The locations of the 45 moulins outside of DEM depressions are compared to the drainage paths calculated for the DEM with an upstream area calculation using a single flow direction algorithm. Similarly to Yang et al. (2015), we find that simulated supraglacial stream channel positions deviate slightly from those observed in imagery. We therefore adjust the position of these 45 observed moulin positions to align with simulated stream channels. Any moulins not falling on a simulated stream location are relocated to the nearest DEM cell with a simulated stream. The mean distance these 45 moulins are moved is 198 m, which is approximately two DEM grid cells. For moulins on potential stream paths which were calculated to be greater than 1 cell wide (90 m), the effective moulin radius was set so that the moulin would capture all water in the stream, rather than allowing some water to effectively bypass the adjacent moulin.

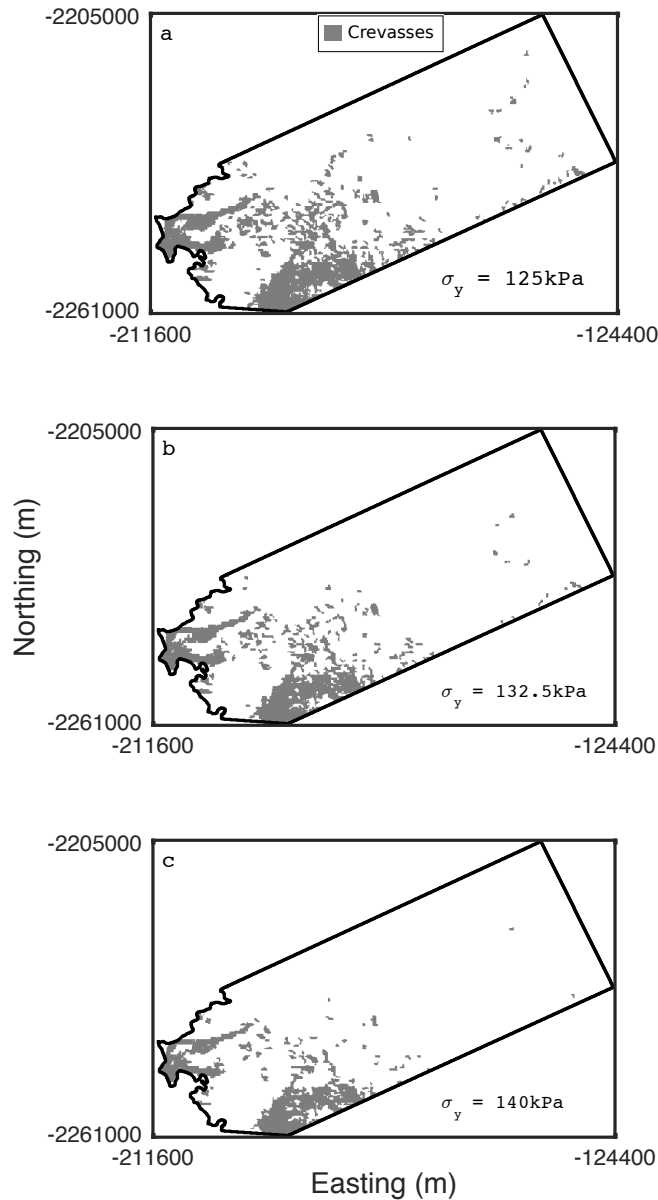


Fig. 3.4 Predicted crevassed areas in the study domain for three different ice yield strengths. a) 125kPa. b) 132.5kPa. c) 140kPa. Map projection is NSIDC Sea Ice Polar Stereographic North.

3.3.4 Driving Variables

Daily melt runoff and snow depth input data for the SRLF model is provided by RACMO2.3 regional climate model simulations (Noël et al., 2015). Melt runoff is defined as the total volume of melt in a cell minus the volume of melt which refreezes. The years 2009, 2011, and 2012 are selected on the basis of their contrasting melt intensities (Figure 3.5). Total

study area melt volumes for the three years selected are $3.46 \times 10^9 \text{ m}^3$, $4.24 \times 10^9 \text{ m}^3$, and $5.39 \times 10^9 \text{ m}^3$, respectively. These three melt years are used as analogues for average, elevated, and extreme melt years. RACMO2.3 model output was provided on a daily temporal resolution, at 11 km spatial resolution. The data are bilinearly interpolated to 90 m resolution. Snow depth is updated daily in the SRLF model. To simulate an idealized diurnal melt cycle, melt runoff is interpolated to hourly time steps using a normal distribution with peak melt between 14:00 and 15:00 (in line with McGrath et al. (2011)), with a standard deviation of two hours. Melt outside a nine-hour window centered on peak melt is set to zero. The area within the nine-hour window is normalized such that the total volume of daily melt is unaltered. We run the SRLF model for the summer melt season, which we define as day 135 of the year (May 15th) to day 274 of the year (October 1st), based on daily melt volume (Figure 3.5).

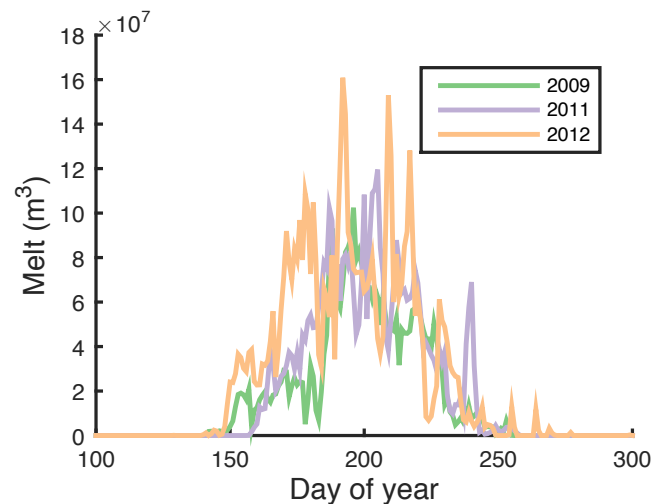


Fig. 3.5 Time series of daily melt in the study area for the 2009, 2011, and 2012 melt seasons modelled by RACMO2.3 (Noël et al., 2015). We use these three years as analogues for average, elevated, and extreme melt years respectively.

3.3.5 Simulation Design

We calibrate the SRLF model using lake drainage statistics for Southwest Greenland during the 2009 melt season (Table 3.2) and perform eleven model simulations (Table 3.3). Lake drainage statistics were provided by Nick Selmes (personal communication, Oct 31st, 2014), derived from data presented in Selmes et al. (2013). R1 is the standard calibrated model run for 2009, and gives the best match to lake drainage statistics. We perform sensitivity analyses on channelization parameters (runs R2-R5), the fracture area parameter (runs R6-R7), and

	Hydrofracture Drainage	Channelized Drainage	None	Unknown
Observed	11.7%	38.9%	43.8%	5.6%
Modelled (R1)	10.7%	37.8%	51.5%	0%

Table 3.2 Remotely sensed and modelled lake drainage statistics for 2009. Remote sensing statistics are for the whole of Southwest Greenland, while model output is limited to the study site (Selmes et al., 2013)

crevasse extent (runs R8-R9) to understand the impact of the updated model components. The standard model is then run with different climate input (runs R10-R11) to investigate the impact of contrasting melt season intensity on supraglacial drainage. Parameter values for runs R1-R11 are shown in Table 3.3. There is the potential for 225 lakes with an area greater than the minimum MODIS pixel size (0.0625 km^2) to form within the study area. In model run R1, all of these lakes filled sufficiently to cover one MODIS pixel. Our analysis focuses on these lakes, as the lake statistics we employ to calibrate our model result from an analysis of MODIS imagery (Selmes et al., 2013). This is in line with the results of Yang et al. (2015), who report that errors in DEM lead to an overprediction of small lakes when compared to satellite imagery. The area threshold 0.0625 km^2 we employ, however, is smaller than the range of values $0.1 \text{ km}^2 - 0.2 \text{ km}^2$ suggested from their preliminary analysis.

Model Run	C_i	γ	F_a	σ_y	Melt Intensity
R1	0.15	0.075	4000	132.5	Average
R2	0.01	0.075	4000	132.5	Average
R3	0.3	0.075	4000	132.5	Average
R4	0.15	0.05	4000	132.5	Average
R5	0.15	0.1	4000	132.5	Average
R6	0.15	0.075	2000	132.5	Average
R7	0.15	0.075	6000	132.5	Average
R8	0.15	0.075	4000	125	Average
R9	0.15	0.075	4000	140	Average
R10	0.15	0.075	4000	132.5	Elevated
R11	0.15	0.075	4000	132.5	Extreme

Table 3.3 Values of parameters which are varied between each of the model runs. Model run R1 is the calibrated model run, R2-R5 are sensitivity tests to channelized drainage parameters, R6-R7 are sensitivity tests of hydrofracturing, R8-R9 are sensitivity tests to crevasse extent, and R10-R11 are sensitivity tests of melt season intensity.

3.4 Results

3.4.1 Standard Run

Simulation results show the majority of water in the study area drains into the englacial hydrological system (Figure 3.6). Of the total surface melt, 15% drains into moulin outside of lake basins, while surface to bed connections from the 24 lakes which hydrofractured capture 24.3%. We divide the volume entering the englacial system through hydrofracturing into two components, the water that is in a lake when hydrofracture occurs, and subsequent drainage into the moulin that results from hydrofracture. We refer to the former as 'LHL' ('Lake Hydrofracture Lake'), and the latter as 'LHM' ('Lake Hydrofracture Moulin'). Only 3.3% of total surface melt drains via LHL, while 21% of total surface melt drains via LHM. Crevasses in run R1 drain 46.6% of surface melt. Only a small proportion of water drains over the ice edge or remains on the surface of the ice sheet, with 3% flowing over the ice margin and 0.6% remaining in lakes at the end of the model run. 9.2% of surface melt leaves the model domain across the northern and southern edges.

The volume of surface drainage decreases away from the ice margin, with the exception of the 0-8.4 km band (Figure 3.7). Surface drainage is greatest in the 8.4-16.8 km band, where 20.25% of the total surface runoff generated in our study area drains. Crevasses drain water throughout the study area. Within 42 km of the ice margin, crevasses are responsible for over 54% of the surface drainage in each distance band. Water drained by moulin is concentrated between 8.4 km and 25.2 km from the study site margin. Approximately 83% of the water entering into moulin does so within this area. Lake hydrofracture and subsequent surface to bed connections drain water upstream of 16.8 km. Except for the interval between 33.6 km and 42 km, lake hydrofracture captures over 34% of meltwater in each distance band above 25.2 km.

Figure 3.8 shows the location and extent of lake basins within the study area, and whether the lakes which formed within them drained via channelized drainage, hydrofracture, or remained at the end of the melt season. We assume any lakes remaining at the end of the melt season freeze. The majority of lake hydrofracture events occurred inland of 25 km from the ice margin, with only one out of 24 hydrofracture events occurring closer to the ice margin. The low fraction of surface drainage via lake hydrofracture between 33.6 km and 42 km corresponds to an area where only two hydrofracture events occur. The model predicts that channelized drainage and lake freezing can occur throughout the study site.

Model calibration results in 85 out of 225 lakes draining over the ice sheet through a channel at their edge. Two representative hydrographs of lakes that completely drained over the ice sheet via channelization are shown in Figure 3.9. In the early stages of channelized

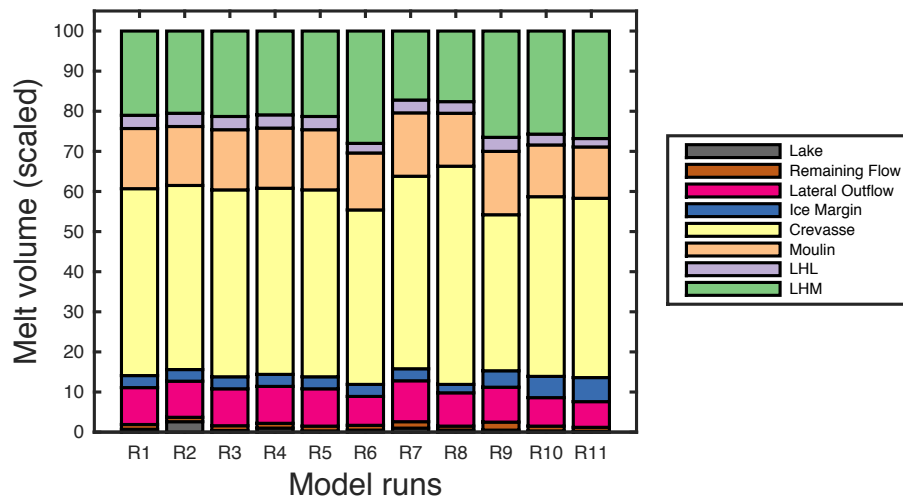


Fig. 3.6 Partitioning of surface melt for the standard run (R1), model sensitivity analysis (R2-R9), and for different melt season intensities (R10-R11). Water stored in category 'Lake' is defined as the volume that remains in lakes at the end of the melt season. 'Remaining Flow' is the amount of water that is still in transit at the end of the simulation. 'Lateral Outflow' is defined as the volume of water that exits our model through the northern and southern boundaries. Water flow off the ice sheet edge is partitioned into the 'Ice Margin' category. The volumes of water captured in crevasses and moulins are partitioned into 'Crevasse' and 'Moulin' respectively. We divide the volume of water drained by surface to bed connections resulting from lake hydrofracture into two categories: 'lake hydrofracture lake' (LHL) and 'lake hydrofracture moulin' (LHM). The initial volume of water in a lake when hydrofracture occurs is partitioned into 'LHL', while subsequent drainage into the surface to bed connection is partitioned into 'LHM'.

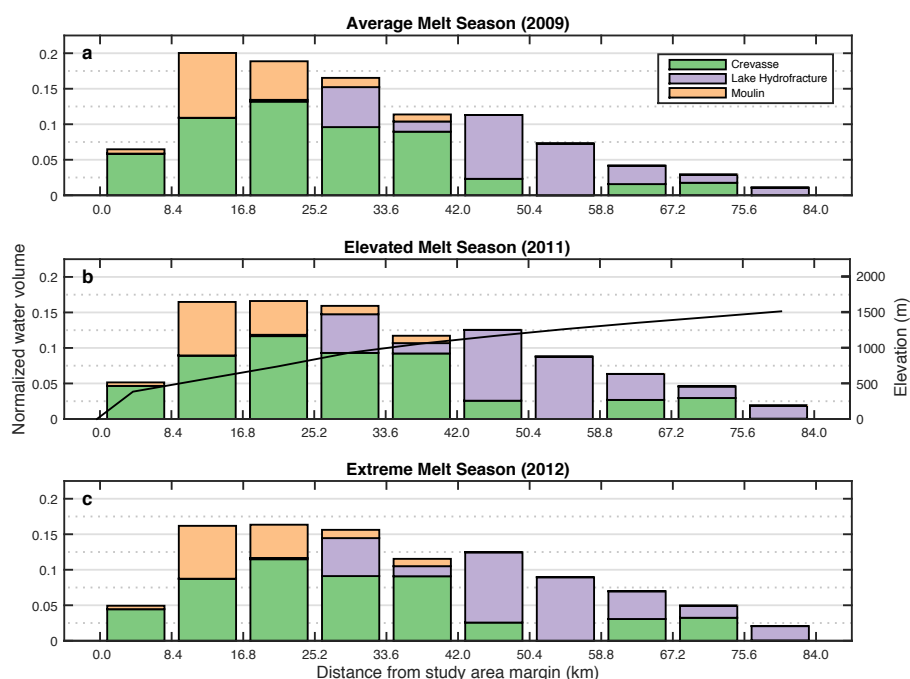


Fig. 3.7 Bar chart showing partitioning of water into different pathways at different distance bands from the study site margin. The three charts correspond to each of the melt season intensities tested: a) average melt year (2011), b) elevated melt year (2011), c) extreme melt year (2012). Black line in middle plot shows width-averaged elevation profile of the study area.

drainage, channel depth increases while lake elevation and volume remain close to, or at, the level of maximum lake capacity. Because the lake is at capacity, any water input must be balanced by the equivalent outflow.

Figure 3.9a/b shows an unstable channelized lake drainage where the rate of channel incision accelerates throughout the lake drainage. Channel incision continues when the channel elevation drops below the bottom of the lake, and the final channel elevation can be metres below the lake bottom elevation. The observable lake drainage event, from the time the lake is last full to complete drainage, occurs on the timescale of days. During this period, the output hydrograph shows a rapid increase in lake output to a sharp peak, followed by a steep decline. Peak lake discharge is $36.4 \text{ m}^3 \text{ s}^{-1}$. Diurnal variations in water output are masked during the observable lake drainage event.

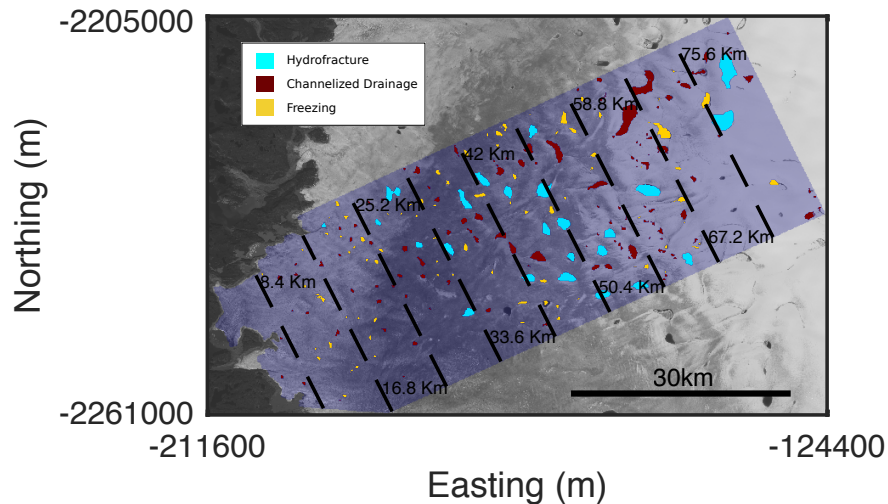


Fig. 3.8 Lake depressions with areas greater than 0.0625 km^2 . The colour of the lake depression corresponds to the fate of the lake which formed in the depression during model simulation R1. Lake hydrofracture and channelized drainage processes are modelled, while lakes which remain at the end of the melt season are assumed to freeze. Blue highlight shows the model study area, with distance bands overlain. Map projection is NSIDC Sea Ice Polar Stereographic North.

Figure 3.9c/d shows a representative lake drainage event where the rate of channel incision decelerates during the observable lake drainage event, increasing the period over which the lake drains. Although the observable lake drainage event takes place over many weeks, the bulk of the lake drains over a period of one to two weeks. The output hydrograph is broader than in the unstable lake drainage, and the lake output flux does not exceed the maximum diurnal input flux. Diurnal cycles in lake output are dampened but remain visible.

As the lake approaches being completely drained, lake output progressively mirrors water input.

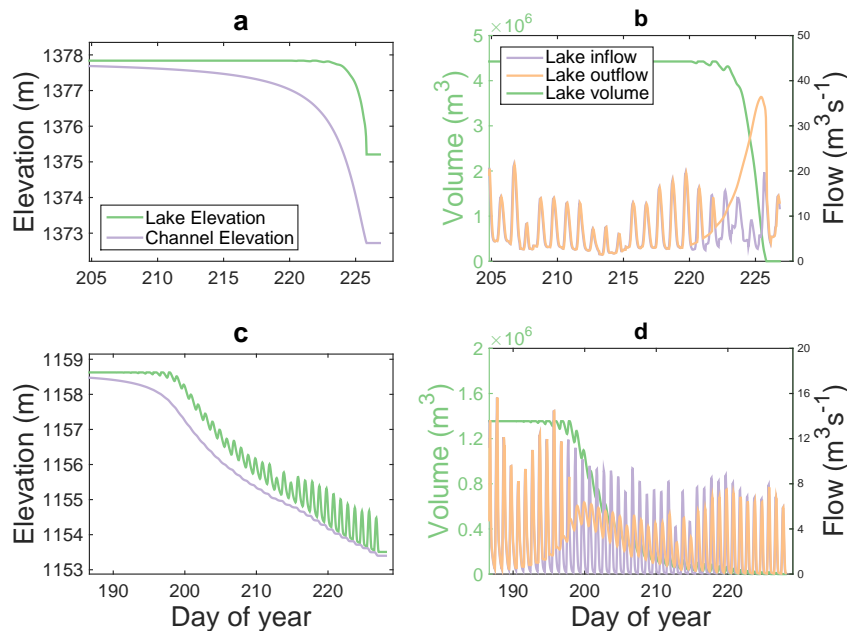


Fig. 3.9 Plots detailing channelized drainage of two different lakes which are representative of lakes which drain unstably (a/b), and of lakes which have initially unstable drainage but which do not continue draining unstably (c/d). Plots a and c show the lake and channel elevations, while plots b and d show the lake volume, lake input, and lake output.

3.4.2 Sensitivity Analysis

Channelization Parameters (R2-R5)

We test the sensitivity of our model to two channel drainage parameters, the initial depth of the channel that forms (C_i), and the heat transfer parameter (γ). The influence of these parameters on lake drainage is shown in Table 3.4. The number of lakes with channelized drainage was not sensitive to these parameters; however, the number of lakes which completely drain varies considerably with the channel drainage parameters. Although changes to the lake drainage parameters have a large proportional impact on the storage capacity of the system, the absolute change in the partitioning of surface melt is relatively small (Figure 3.6). At the end of run R1 0.6% of the total surface melt is stored in lakes. In our sensitivity analysis of lake drainage parameters, the percentage of surface melt stored in lakes at the end of

simulations increases to a maximum of 2.5% in run R2, and decreases to a minimum of 0.3% in R4.

	R1	R2	R3	R4	R5	R6	R7	R8	R9	R10	R11
Lakes hydrofractured	24	24	24	24	24	35	16	20	27	24	24
Lakes with channelized drainage	190	190	186	190	190	176	199	182	196	190	190
Lakes drained completely via channelization	85	1	110	47	115	79	86	83	98	98	124

Table 3.4 Statistics of lake hydrofracture and lake drainage via channelization for each of the modelled runs.

Fracture Area (R6-R7)

The fracture area parameter (F_a) determines the volume at which a lake hydrofractures. Simulation R1 is run with a parameter value of 4000 m² (within the range of best fit of Arnold et al. (2014)), and predicts 24 lakes hydrofracturing. The number of lakes which hydrofracture is sensitive to F_a , increasing to 35 in R6 and decreasing to 16 in R7. This has a negligible impact on surface storage in lakes ($\leq 0.4\%$ of total surface runoff), but changes the total proportion of surface melt drained by lake hydrofracture and the subsequent surface to bed connection from 24.3% in R1, to 30.4% in R6 and 20.4% in R7.

Crevasse Extent (R8-R9)

To quantify the uncertainty associated with the extent of crevassed areas, we perform two model simulations (R8-R9) with crevasse extent determined by different ice yield strengths. Simulation R1 is run with a yield stress of 132.5 kPa, which we perturb by ± 7.5 kPa in simulations R8 and R9. A yield strength of 125 kPa (R8) increases the crevassed area extent by 32%, and the proportion of water entering crevasses from 46.6% to 54.4%. Similarly, increasing the yield strength to 140 kPa (R9) decreased the crevasse extent by 25%, and decreases proportion of water entering crevassed areas to 38.9% of total surface runoff.

3.4.3 Interannual Comparison

Model simulations R10 and R11 correspond to the 2011 (elevated) and 2012 (extreme) melt seasons. In both simulations, the number of lakes which hydrofractured was the same as in simulation R1. However, the proportion and volume of water drained by lake hydrofracture and the subsequent surface to bed connection increases from 24.3% (0.84 km³) in R1 to 28.4% (1.20 km³) in R10 and 28.9% (1.55 km³) in R11. Because lake drainages are triggered

by a volumetric threshold, the volume of water draining via LHL remained constant at 0.11 km^3 in all three melt seasons. This results in the proportion of total melt draining via LHL decreasing from 3.3% in R1 to 2.7% in R10, and 2.1% in R11. Increases in the proportion of water drained by lake hydrofracture therefore come from increased drainage in LHM. Between R1 and R10, drainage via LHM increased from 21% (0.73 km^3) to 25.7% (1.09 km^3). Between R10 and R11 there is a smaller increase of 1.1%, from 25.7% to 26.8% (1.44 km^3) in drainage via LHM. While the proportion of water drained by lake hydrofracture increases, the proportion drained by crevasses and moulins outside of lake basins decreases. In R1, moulins capture 15% of melt, while in R10 and R11, moulins capture 12.9% and 12.8% of surface runoff respectively.

Although the proportion of total surface meltwater draining via moulins decreases, the volume of surface melt draining via moulins increases from 0.52 km^3 in R1, to 0.55 km^3 and 0.69 km^3 in R10 and R11. Similarly, crevasses capture 46.6% of surface runoff in R1, but only 44.8% of surface runoff in R10. In R11, this proportion remains approximately the same at 44.7%. However, the volume of surface melt draining via crevasses increases from 1.61 km^3 to 1.90 km^3 and 2.41 km^3 as melt intensity increases.

As melt intensity increases from average to elevated, a higher proportion of meltwater is predicted to drain further from the ice margin (Figure 3.7). Compared to simulation R1, each distance band up to 33.6 km from the study margin in simulation R10 drains a smaller proportion of water, while each distance band above 33.6 km drains an increased proportion of water. Changes in each distance band are limited to a few percent of total surface runoff. The maximum decrease was in distance band 8.4-16.8 km which drained 3.5% less of total surface runoff, while the maximum increase was in distance band 58.8-67.2 km which drained 2.3% more total surface runoff.

Although the proportion of total melt runoff drained by the distance band 8.4-16.8 km decreased, the volume of water drained in this band remained approximately the same at 0.60 km^3 . In the distance band 58.8-67.2 km, the volume of water drained increased from 0.12 km^3 to 0.23 km^3 . While there is a marked upslope shift in surface drainage between R1 and R10, between R10 and R11 there is only a small change in the spatial distribution of water drainage.

The cumulative proportion of surface runoff drained above 58.8 km ($\sim 1300 \text{ m}$) in our study area is 7.16% in R1, 11.18% in R10, and 12.21% in R11.

Although the number of lakes with channelized drainage does not increase in simulations R10 and R11, the number of lakes which completely drain over the ice sheet through channelization increases from 85 to 98 in R10, and up to 124 in R11 (Table 3.4).

3.5 Discussion

A key overall prediction from our modelling results is that only 3-6% of surface melt flows off the edge of the ice sheet, and under 1% remains in storage in lakes on the surface of the ice sheet. Over ~85% percent of water is modelled to drain into the ice sheet, with ~9% percent leaving through the lateral study area margins. Assuming the water leaving through the lateral margins remains in lakes and drains off the ice margin in a similar proportion, then over 95% of water drains into the englacial system.

This is in clear agreement with the results of Smith et al. (2015), who report that surface storage during 2012 in their study area was limited compared to the amount of melt generated, and that all observed surface rivers drained into the ice sheet. This is also consistent with other studies of the Paakitsoq region which suggest that water draining into deep crevasses contributes to cryohydrological warming of the ice sheet (Lüthi et al., 2015; Phillips et al., 2013). Of the different meltwater pathways, drainage into crevassed areas is the most significant route for water to enter the ice sheet (47% of overall melt). Drainage via the moulins established by lake hydrofracture accounts for ~24% (but the hydrofracture events themselves only account for ~3%), and other moulins account for ~15%.

Similarly to Yang et al. (2015) we find agreement between observed moulins and predicted supraglacial stream locations. We also similarly find broad scale agreement between calculated stream networks and those observed in recent WorldView imagery. A comparison of stream networks observed in 1985 and 2009 reveals similar network structure, suggesting that the broad-scale pattern of stream networks remains similar over decadal timescales. Previous work (Arnold et al., 2014) has found good agreement between lakes predicted from the GIMP DEM and observed locations/depths. Since surface storage on the ice sheet surface is low, false positive filling of lakes should have a negligible impact. This suggests that current high resolution DEMs, in conjunction with moulins and crevasse locations derived from remote sensing, provide a suitable dataset for surface hydrology models.

The partitioning of drainage is spatially variable over the study area. Similarly to Clason et al. (2015), and consistent with Joughin et al. (2013), we find that drainage via lake hydrofracture is a significant drainage pathway at higher elevations (above ~850 m). Moulins are shown to primarily drain water near the ice margin. Crevasses drain water throughout the study area, although drainage into crevasses is concentrated at lower elevations where their extent is greatest. The spatial distribution of different meltwater pathways may have an important role in modulating the variability of surface runoff to the bed, as crevasses are predicted to dampen diurnal meltwater fluctuations reaching the ice-bed interface relative to moulins (McGrath et al., 2011). Thus, within the Paakitsoq region, we would expect changes in runoff variability to be more effectively transmitted to the ice-bed interface at

higher elevations, where crevasses drain a smaller proportion of surface runoff. Given that subglacial hydrological models suggest that it is the variability of water inputs, rather than the total amount of input that is the key control on basal drag (Hewitt, 2013; Schoof, 2010) this could imply that the seasonal variability of ice sheet velocity could be larger at higher elevations on the ice sheet.

While channelized lake drainage has minimal impact on meltwater partitioning in our model due to the limited capacity of lakes relative to total surface runoff, channelized lake drainage changes the timing and characteristics of water flow downstream of lakes. As observed by Tedesco et al. (2013a), channelized drainage events which flow into a downstream moulin can temporarily increase ice velocities. Our study reproduces the observed timescale of days to several weeks for lakes draining over the ice sheet via channelization (Selmes et al., 2013; Tedesco et al., 2013a). In our model, rapid drainage of lakes on the timescale of days occurs if channel incision is unstable such that the decrease in the elevation of the bed of the channel is faster than the lowering of the lake surface. Our model also shows a different mode of channelized drainage, on the timescale of weeks, in which drainage switches from unstable to stable drainage in which the rate of channel incision matches the lowering of the lake surface. The diversity of behaviour agrees with Kingslake et al. (2015), who find that the stability of channelized drainage is controlled by lake geometry, channel slope, and melt input.

The sensitivity analysis can be divided into simulations testing model parameters (R2-R7) and simulations testing model inputs (R8-R11). We find that while the number of lakes which undergo channelized drainage is insensitive to channelization parameter values, the number of lakes which drain completely is strongly controlled by the initial depth of the channel that forms (R2-R3) and the heat transfer parameter (R4-R5). The sensitivity to the initial depth parameter suggests that features below our DEM resolution, particularly relic channelization from previous years and small scale topography around the rim of the lake (which we do not directly allow for, but which the initial channel depth simulates to some degree) could have a significant role in determining whether channelized drainage occurs, and the timescale over which lakes drain. Because of the sensitivity to the heat transfer parameter, possible spatial and temporal variation in lake temperature (due to different meteorological conditions) could also impact the pattern and timing of lake drainages.

Our results (R8-R9) show that whilst varying yield strength can make a large difference in the overall area predicted to be crevassed ($\sim 30\%$), the impact on the overall partitioning of meltwater is more muted ($\sim 8\%$ of total surface runoff). Whilst Colgan et al. (2011b) show an increase in the crevassed area of 13% between 1985 and 2009 (using satellite imagery), our results suggest that such a change would have a relatively minor impact on melt partitioning.

However, if this rate of expansion continues, long term changes in crevasse distribution may become important for melt partitioning.

Melt availability (R10-R11) affects two aspects of model behaviour. Higher meltwater production causes hydrofracture events to occur earlier in the melt season (as lakes will reach the critical volume for fracture more quickly). This has no impact on the volume of water drained during the event itself, but could lead to an earlier development of an efficient subglacial drainage system, resulting in an earlier summer slowdown (Bartholomew et al., 2010; Cowton et al., 2013; Schoof, 2010; Sundal et al., 2011). Higher melt availability also increases the number of modelled lakes which drain completely by channelized drainage. This reduces the total amount of water stored on the ice sheet at the end of the summer (though as stated, this is a very small proportion of the overall melt). Warmer melt seasons may also increase the temperature of water in lakes, increasing the amount of energy available for channels to incise into the ice sheet surface (simulated at present using the heat transfer parameter, γ).

The spatial distribution of surface drainage shows some sensitivity to melt availability. As melt season intensity rises from average to elevated, the proportion of water drained beyond 58.8 km (~ 1300 m) from the ice margin increases by $\sim 5\%$ of total surface runoff. Drainage via surface to bed connections created by lake hydrofracture forms an increased proportion of meltwater, while crevasses and moulins outside of lake basins drain a decreased proportion of melt water. However, the partitioning of water between elevated and extreme melt seasons remains similar, with only a small increase ($\sim 1\%$ of total surface runoff) in the proportion of water drained at higher elevations. This shows melt partitioning does not consistently vary inter-annually, nor linearly with melt season intensity.

There are some aspects of the observed behaviour of the supraglacial drainage system which our model cannot capture. The observed inter-annual variability of the behaviour of lakes suggests that a subset of the lake population is capable of both hydrofracture and channelized drainage (Selmes et al., 2013), with the mechanism of drainage determined by an unknown preconditioning. This competition is not directly captured in our model largely due to the limitations of the fracture area criterion, which effectively pre-determines lakes that can drain via hydrofracture; such lakes can never incise a channel at their lip, as hydrofracture will prevent them filling to the maximum volume determined by the ice sheet topography, a pre-condition in our model for channelized drainage. Lakes for which the topographically controlled maximum volume is smaller than the threshold volume for hydrofracture can never exhibit hydrofracture, but can only overflow. However, here the model does allow for some year-on-year variability, as the channelization mechanism does depend on the rate of incision of the channel versus the rate at which the lake surface elevation changes. Thus, in any given

year, a lake could show simple overflow drainage, or stable or unstable channelized drainage, depending on the rate of water inputs to the lake versus water outflow. We cannot however simulate the possible existence of a deeply incised channel from a previous year which could prevent a lake from forming at all in extreme cases, as has effectively been inferred by Smith et al. (2015), who observed that in certain cases, streams on the ice sheet had effectively cut through local topographic divides.

Ultimately, it seems very unlikely that a model could ever predict the possible behaviour over several years of any individual lake. At a catchment or regional scale, however, it may be that some form of stochastic variations in the fracture area threshold (potentially linked to a local strain threshold) could allow the statistical properties of a set of lakes to be simulated more effectively than in a deterministic model. Such a model, applied in a form of Monte-Carlo analysis, might allow the range of possible water inputs to a subglacial hydrological model to be simulated more effectively for a range of melt scenarios, in turn allowing more effective simulation of the possible impact of climate change on ice dynamics.

3.6 Conclusions

In this chapter we have applied a model of supraglacial hydrology to the Paakitsoq region of Western Greenland for three years: 2009, 2011 and 2012. The model is forced using melt rates and snow depths from a regional climate model (Noël et al., 2015), simulates water flow over a digital elevation model of the surface of the ice sheet (Howat et al., 2015), and allows surface water to accumulate as lakes in topographically controlled basins. Water can enter the englacial hydrological system via water-volume-driven lake hydrofracture events, through observed moulins, and via crevassed areas, determined from surface stresses derived from mean winter velocities. Lakes can also drain supraglacially via simple topographic overflow, and via the incision of supraglacial streams into the lips damming lakes.

The model has been used to better understand the partitioning of water routes into the en- (and potentially, therefore, the sub-) glacial drainage system. Previous modelling studies have typically focused on hydrofracture beneath supraglacial lakes (Arnold et al., 2014; Banwell et al., 2012a; Clason et al., 2015), although Clason et al. (2015) also allow for hydrofracture to occur outside lake basins. Observational studies have shown that drainage outside of lake basins can deliver significant volumes of water to the englacial system (Smith et al., 2015; Yang et al., 2015), so the incorporation of drainage into crevasses or moulins at locations derived from remote sensing data (rather than solely at locations depending on hydrofracture) allows our model to more realistically reflect these observations.

Our results produce a suite of behaviours that agree well with observations of lake behaviour. Modelled lakes can drain via hydrofracture, they can drain slowly (over days to weeks) via the incision of supraglacial channels, and some lakes simply remain full at the end of the melt season, and are assumed to freeze over winter. Overall, over 95% of available melt in the model likely enters the englacial drainage system. In our standard run (with parameter values chosen to match observed frequencies of lake behaviour), crevassed areas drain 47% of the available melt, 24% drains through the surface-to-bed connections established by lake hydrofracture events, and 15% via moulins located outside of lake basins. In the case of hydrofracture events, the bulk of this water actually enters the glacier after the fracture event itself, via streams flowing into the fracture established during the event; a very small proportion (3%) is drained during the events themselves. This reflects the small overall volume of supraglacial lakes compared with the total volume of melt produced in a typical melt season. These proportions are affected to some extent by the parameter values chosen, but the overall balance of partitioning of melt is robust, as is the finding that almost all water enters the ice sheet. Channelized surface drainage of lakes does not alter the overall partitioning of meltwater routing into the ice sheet, but has been observed to impact the timing of lake hydrofracture downstream (Banwell et al., 2012a; Tedesco et al., 2013a)

The model results show limited sensitivity to melt intensity; in the warmer years (2011 and 2012) the proportion of water which drains via hydrofracture increases at the expense of the other two routes, driven largely by the earlier occurrence of hydrofracture events as lakes reach the critical volume for hydrofracture earlier in the melt season.

The partitioning of melt drainage varies spatially over the ice sheet, with moulin drainage more common at lower elevations and hydrofracture more important at higher elevations. Drainage via crevasses occurs at all elevations, but is concentrated at lower elevations where they are more common. Higher melt intensity leads to a change in this spatial partitioning, with an increase in hydrofracture events at higher elevations at the expense of the other two routes.

Our results have important implications in terms of the potential impact of supraglacially-derived water on ice sheet dynamics. In terms of the overall partitioning of meltwater, we find that crevasses capture a significant proportion of supraglacial meltwater. This implies that the possible mechanisms which could link water in surface crevasses to the subglacial drainage system are important to understand. We also find that the total volume of water transported to the bed via lake hydrofracture events in themselves is small in comparison with the total amount of water entering the system subsequently via the newly created moulins. Whilst lake drainage events, and the very high discharges associated with them, seem likely to remain a key control on the development of subglacial drainage networks (e.g. Das et al.,

2008; Doyle et al., 2014), as melt increases, and lake drainage events potentially occur earlier in the melt season, the subsequent drainage (and the characteristics of such flow) could become increasingly significant in terms of ice sheet dynamics and potential summer velocity change. This also relates to our finding that the partitioning of meltwater can change with melt season intensity, but does not do so in a straightforward or linear manner. Whilst inter-annual variations in melt intensity could affect ice dynamics, this would depend on the nature of the supraglacial drainage system and its sensitivity to melt availability, and also on the sensitivity of the subglacial system itself to changes in the partitioning of water inputs.

The model developments we have implemented here allow a more diverse and realistic set of behaviours for supraglacial water than has been possible in previous studies. They have allowed us to estimate the proportions of water entering the ice sheet via different drainage paths, and how this balance varies spatially. This study has also allowed us to begin to estimate how changes in melt intensity could affect the balance in the routes by which meltwater enters the ice sheet, which could have implications for how the dynamics of the ice sheet may change in response to ongoing climatic changes. In the subsequent chapters, the model described here is linked to a coupled subglacial hydrology/ice dynamics model in order to begin to quantify these changes.

Chapter 4

Ice Sheet Modelling and Inversions

4.1 Overview

In this chapter an ice sheet model and corresponding inversion code are developed. The ice sheet model is verified using the Ice Sheet Model Intercomparison Project for Higher-Order ice sheet Models (ISMIP-HOM) simulations (Gagliardini and Zwinger, 2008), while the inversion code is verified using a series of identical twin tests (Goldberg and Heimbach, 2013). The inversion model is then applied to the Russell Glacier region of Western Greenland to invert for basal parameters using mean winter velocities. Inversions using non-linear sliding laws incorporate basal water pressures predicted by the current subglacial hydrological model (Hewitt, 2013).

This chapter is independent of Chapter 3 of the thesis. Chapter 3 and Chapter 4 are brought together in Chapter 5, where the ice sheet model is forced with the supra-glacial hydrology model of Chapter 3, and initialized with the inversions in this chapter.

This chapter begins with a short overview of the work presented and its relation to other chapters in this thesis. It is followed by a general introduction to ice flow and inversions. The methods section presents the ice sheet model and inversion code, as well as briefly describing the subglacial hydrology model. The section on simulations details the application of the model to both idealized and real-world simulations. The results section shows the predicted state of the subglacial hydrology system at the end of winter, and the corresponding predicted basal drag for different sliding laws. The discussion covers model verification, sensitivity of the subglacial hydrology model to parameters, and similarities/differences between the different inversions. This section concludes that the ice sheet model and inversion code are robust, and provides an initialization for the modelling in the next chapter.

4.2 Introduction

Ice sheets are sensitive to a variety of forcings. These include meteorological input at the upper surface, ocean conditions at marine terminating sectors, and basal conditions at the ice-bed interface. Numerical models are an important tool for understanding how these forcings drive dynamic changes of ice sheets. Models provide a method to test the response of ice sheets to changes in climatic and environmental variables. Moreover, models allow quantitative predictions of the future state of ice sheets. This is particularly relevant in the context of climate change, since ice mass loss from the GrIS is a major contributor to global sea level rise (Vaughan et al., 2013).

An ice sheet model solves a set of equations that determines the velocity field of an ice sheet, given the geometry and appropriate boundary conditions. The equations describing ice flow are the Stokes equations. These are derived from the more general Navier-Stokes equations by scaling arguments showing that the inertial terms are negligible. Ice is assumed to be incompressible, leading to following equations describing conservation of momentum and mass:

$$\nabla \cdot \boldsymbol{\sigma} + \rho \mathbf{g} = \mathbf{0} \quad (4.1)$$

$$\nabla \cdot \mathbf{u} = 0 \quad (4.2)$$

where $\nabla \cdot \boldsymbol{\sigma}$ is the divergence of the cauchy stress tensor ($\boldsymbol{\sigma}$), \mathbf{g} is the acceleration due to gravity, and \mathbf{u} is velocity.

In addition, a constitutive equation which describes the behavior of ice is required. A widely used model in glaciology is the generalized Glen's law (Cuffey and Paterson, 2010):

$$\dot{\boldsymbol{\epsilon}}_{ij} = A \tau_E^{n-1} \tau_{ij} \quad (4.3)$$

where $\dot{\boldsymbol{\epsilon}}$ is the strain rate tensor, τ_{ij} is the deviator stress tensor, τ_E is the second invariant of the deviator stress tensor (referred to as effective stress), and A is the creep parameter. Ice is assumed isotropic. Deviatoric stress is defined as:

$$\tau_{ij} = \sigma_{ij} - \delta_{ij} p \quad (4.4)$$

where pressure (p) is defined as:

$$p = \frac{1}{3} tr(\boldsymbol{\sigma}) \quad (4.5)$$

and $tr(\cdot)$ is the trace operator. The second invariant of a matrix M is defined as $tr(M \cdot M)$.

Laboratory experiments show that the exponent n in Glen's Flow law varies with applied stress, due to the different creep mechanisms (Goldsby and Kohlstedt, 2001). However, a constant value of three is often used in ice sheet models (Cuffey and Paterson, 2010). The ice creep parameter A in Glen's Flow law depends strongly on the properties of ice, including temperature, pressure, impurities, and water content (Cuffey and Paterson, 2010).

While the Stokes equations provide a complete description of ice flow, they are computationally expensive to solve. Hence, the Stokes equations have been simplified further by assumptions related to the high aspect ratio of ice sheets. If ice-flow in a regime where these simplifications are appropriate is modelled, then a simpler set of equations can be solved, with a tolerable loss of accuracy. The three main set of equations derived from the Stokes are the Blatter-Pattyn equations (BP) (Blatter, 1995; Pattyn, 2003), Shallow Shelf Approximation equations (SSA) (MacAyeal, 1989), and Shallow Ice Approximation equations (SIA) (Hutter, 1983).

The Blatter-Pattyn equations are derived from the Full Stokes equations based on two assumptions: 1) That the vertical force balance is hydrostatic; 2) horizontal gradients of the vertical velocity are small compared to the vertical gradient of horizontal velocities (i.e. bridging effects are negligible) (Greve and Blatter, 2009; Morlighem et al., 2013). The Blatter-Pattyn equations have been shown to be widely applicable over the Antarctic Ice Sheet (Morlighem et al., 2013). With additional assumptions, the Blatter-Pattyn equations can be further simplified to the SIA and SSA equations. These equations describe two contrasting flow regimes. The SIA equations assumes ice flow is dominated by horizontal shearing and there are negligible longitudinal stresses, making them well suited to slow flowing ice in the interior of ice sheets. The SSA equations are assumes ice flow is dominated by longitudinal stresses, and negligible horizontal shearing. In this regime, ice is modelled as plug flow, making these equations suited to fast flowing ice such as ice streams.

Models which combine the SIA and SSA equations have recently begun to be implemented in the glaciology community. These models retain much of the numerical simplicity/efficiency of the SSA and SIA equations while approximating the BP equations. The advantage of many of these schemes is that the vertical profile of horizontal velocity is accounted for implicitly. This profile can be reconstructed from the solution of the horizontal velocities if needed. Models combining the SIA and SSA equations are also valid in both the SIA and SSA flow regimes. A variety of specific schemes have been proposed (e.g Bueler and Brown, 2009; Goldberg, 2011; Hindmarsh, 2004).

To accurately simulate the present state of ice sheets, the parameters and state of an ice sheet model must be properly initialized. Data for initializing ice sheet models for the

present day is primarily from remote sensing. Satellite measurements provide a time series of data from the upper surface of ice sheets. These data products include: surface velocities, surface mass balance, and altimetry. In contrast, the interior and bed of ice sheets are less conducive to measurement. Bed topography is known through airborne radar campaigns. However, direct measurements of ice temperature and the basal hydrological system are only possible through boreholes, which provide a point data source. Hence, the interior state and basal boundary conditions of ice sheets remain extremely poorly constrained compared to the upper surface.

Inverse methods are an approach which can be used to constrain unknown variables or parameters in an ice sheet model. Inversions optimize the value of an unknown to minimize the discrepancy between model output and observed data. One of the least constrained inputs to an ice sheet model, and yet an important control on ice dynamics, is basal friction. A common application of inversions in glaciology therefore is to determine the field of basal drag which best reproduces observed surface velocities. A variety of inversion methodologies have been applied in glaciology. These include iterative methods (Arthern et al., 2015), automatic differentiation (Goldberg and Heimbach, 2013; Heimbach and Bugnion, 2009; Martin and Monnier, 2014), and Lagrangian multiplier methods based on control theory (MacAyeal, 1993; Morlighem et al., 2013).

Inverse problems in ice sheet modelling are ill posed, and have important limitations. One limitation is high sensitivity to input data. Small changes to known variables, such as surface velocity, can lead to large differences in the solutions of basal drag or ice viscosity. This is significant in the context of glaciology, as all data products feature errors. A second limitation is that the problem is typically underdetermined. To improve the stability of the problem, and prevent the overfitting of observations, a regularization term can be incorporated into the inverse problem. Regularization adds another assumption about the problem, such as that the parameter being inverted for varies smoothly in space. Although regularization incorporates a priori knowledge about the problem, the choice of regularization is typically done heuristically.

In this chapter, we develop an ice sheet model and inversion code. The ice sheet model uses the hybrid formulation of Goldberg (2011) and Arthern et al. (2015) and is numerically similar to Arthern et al. (2015). The ice sheet model is verified using the ISMIP-HOM set of experiments. The inversion procedure is based on automatic differentiation (Goldberg and Heimbach, 2013). The inversion code is verified through a series of twin tests. In this chapter, the inversion model is also applied to model the Russell Glacier area of Western Greenland to invert for basal drag during the winter. An inversion is run for each of the three different sliding laws implemented, including two non-linear sliding laws which are

functions of effective pressure. A current subglacial hydrology model is used to predict the state of the subglacial hydrology system. The application is novel in that inversions explicitly depend on the state of the system.

4.3 Methods

4.3.1 Hybrid Ice Sheet Model

Model Formulation

The ice sheet model implemented is based on the hybrid formulation described in Goldberg (2011) and Arthern et al. (2015), and uses the numerical implementation of Arthern et al. (2015).

Following Arthern et al. (2015); Goldberg (2011), the conservation of momentum equations for depth-averaged velocities are:

$$\partial_x(4h\bar{\eta}\partial_x\bar{u} + 2h\bar{\eta}\partial_y\bar{v}) + \partial_y(h\bar{\eta}\partial_x\bar{v} + h\bar{\eta}\partial_y\bar{u}) - \tau_{bx} = \rho_i g h \partial_x s \quad (4.6)$$

$$\partial_y(4h\bar{\eta}\partial_y\bar{v} + 2h\bar{\eta}\partial_x\bar{u}) + \partial_x(h\bar{\eta}\partial_y\bar{u} + h\bar{\eta}\partial_x\bar{v}) - \tau_{by} = \rho_i g h \partial_y s \quad (4.7)$$

where $u(x, y, z)$ and $v(x, y, z)$ are velocities in the x and y directions, $\eta(x, y, z)$ is dynamic viscosity, $h(x, y)$ is ice thickness, $s(x, y)$ is surface elevation, $\tau_{bx(x,y)}$ and $\tau_{by(x,y)}$ are basal drag in the x and y directions, g is the magnitude of gravitational acceleration, and ρ_i is the density of ice. The overbar ($\bar{\cdot}$) denotes the depth averaged value of a variable, so that $\bar{u}(x, y)$ and $\bar{v}(x, y)$ are depth averaged velocities and $\bar{\eta}(x, y)$ is depth averaged viscosity.

Basal drag is defined by the sliding law. Three different sliding laws are implemented in the ice sheet model:

$$\boldsymbol{\tau}_b = \beta^2 \mathbf{u}_b \quad (4.8)$$

$$\boldsymbol{\tau}_b = \mu_a N_+^p U_b^q \frac{\mathbf{u}_b}{U_b} \quad (4.9)$$

$$\boldsymbol{\tau}_b = \mu_b N_+ \left(\frac{U_b}{U_b + \lambda_b A_b N_+^n} \right)^{\frac{1}{n}} \frac{\mathbf{u}_b}{U_b} \quad (4.10)$$

where $\boldsymbol{\tau}_b = (\tau_{bx}(x, y), \tau_{by}(x, y))$ is the basal drag, $\mathbf{u}_b = (u_b, v_b) = (u(x, y, b), v(x, y, b))$ is the basal velocity, U_b is the sliding speed ($|\mathbf{u}_b|$), $N(x, y) = \rho_i g h - p_w$ is the effective pressure at the ice sheet bed, p_w is water pressure, $\beta(x, y)$ is a basal drag coefficient, $\mu_a(x, y)$ is a drag coefficient, p and q are positive exponents, $\mu_b(x, y)$ is a limiting roughness slope, λ_b is the characteristic bed roughness length, and A_b and n are coefficients in Glen's flow law (Hewitt, 2013). A_b is the ice creep parameter set to an appropriate value for basal ice. Following

Hewitt (2013), negative effective pressures are eliminated by setting $N_+ = \max(N, 0)$, and regularized with a small regularization constant.

The linear sliding law (Eq. 5.10) represents all ice-bed interactions by a single friction coefficient β . The second and third equations are a generalized Weertman sliding law and a Schoof sliding law respectively (Hewitt, 2013). These attempt to explicitly represent more complex interactions at the ice-bed-interface, in particular, the impact of basal water pressure. Equation 5.11 is a power law commonly used in glaciology to describe basal rheology (e.g. Bueler and Brown, 2009; Hewitt, 2013; MacAyeal, 1989), although typically with no dependence on effective pressure ($p = 0$). At high effective pressures the Schoof sliding law has a similar form ($\boldsymbol{\tau}_b \approx \mu_b (\lambda_b A_b)^{-1} U_b^{\frac{1}{n}}$), but transitions to a Coulomb description at low effective pressures ($\boldsymbol{\tau}_b \approx \mu_b N$).

It is useful to represent the sliding laws in a common form:

$$\boldsymbol{\tau}_b = C \mathbf{u}_b \quad (4.11)$$

where C is a function multiplying basal velocities. The form and parameters of C depend on the sliding law.

The boundary conditions at the terminating margin of the ice sheet are:

$$2\bar{\eta}h(2\partial_x\bar{u} + \partial_y\bar{v})\hat{n}_x + \bar{\eta}h(\partial_y\bar{u} + \partial_x\bar{v})\hat{n}_y = \frac{g}{2}(\rho_i h^2 - \rho_w d^2)\hat{n}_x \quad (4.12)$$

$$2\bar{\eta}h(2\partial_y\bar{v} + \partial_x\bar{u})\hat{n}_y + \bar{\eta}h(\partial_y\bar{u} + \partial_x\bar{v})\hat{n}_x = \frac{g}{2}(\rho_i h^2 - \rho_w d^2)\hat{n}_y \quad (4.13)$$

where ρ_w is the density of water, d is the ice draft (zero at land terminating portions of the margin), and \hat{n}_x and \hat{n}_y are the components of the unit vector normal to the terminating margin (Arthern et al., 2015; Goldberg, 2011).

Three further boundary conditions are used in the ice sheet model: a no-penetration condition at the margin of nunatoks, a dirichlet boundary condition at the lateral margins of the ice sheet domain which are not the termination edge, and periodic boundary conditions for model testing.

The equation for viscosity is:

$$\eta = \frac{1}{2} A^{\frac{-1}{n}} ((\partial_x u)^2 + (\partial_y v)^2 + (\partial_x v)(\partial_y u) + (\partial_x v + \partial_y u)^2 + \frac{1}{4}(\partial_z u)^2 + \frac{1}{4}(\partial_z v)^2 + \epsilon_0)^{\frac{1-n}{2n}} \quad (4.14)$$

where ϵ_0 is a regularization term. Vertical shearing in the hybrid formulation is approximated by:

$$\partial_z u \approx \partial_z u + \partial_x w = \frac{\sigma_{xz}}{\eta}, \quad \partial_z v \approx \partial_z v + \partial_y w = \frac{\sigma_{yz}}{\eta} \quad (4.15)$$

As in Arthern et al. (2015); Goldberg (2011), a linear relationship between vertical shear stresses and depth is assumed:

$$\sigma_{xz} = \tau_{bx} \frac{s-z}{h}, \quad \sigma_{yz} = \tau_{by} \frac{s-z}{h} \quad (4.16)$$

Viscosity is defined implicitly by Eq. (4.14). With the standard choice of $n=3$, this is a cubic equation, and can be solved exactly. Alternatively, a previous value of viscosity can be used to calculate an updated value. This process can be iterated upon, to create a fixed point-iteration. The default procedure in the model is to do two iterations (see Section. 4.4.1).

The hybrid formulation of the conservation of momentum equations depend on depth integrated viscosity:

$$\bar{\eta} = \frac{1}{h} \int_s^b \eta dz \quad (4.17)$$

This integral, and others, are numerically integrating using the Composite Simpson's Law. Following Arthern et al. (2015), the following integral is defined:

$$F_a = \int_s^b \frac{1}{\eta} \left(\frac{s-z}{h} \right)^a dz \quad (4.18)$$

This integral can be used to define expressions for surface velocity in terms of basal velocity, and basal velocity in terms of depth averaged velocity (Arthern et al., 2015):

$$\mathbf{u}_s = \mathbf{u}_b (1 + CF_1) \quad (4.19)$$

$$\bar{\mathbf{u}} = \mathbf{u}_b (1 + CF_2) \quad (4.20)$$

where F_1 and F_2 are determined using Eq. 4.18 .

Additionally, defining C_{eff} as follows,

$$C_{eff} = \frac{C}{1 + CF_2} \quad (4.21)$$

leads to an expression for basal drag in terms of depth averaged velocity (Arthern et al., 2015; Goldberg, 2011):

$$\boldsymbol{\tau}_b = C_{eff} \mathbf{u}_b \quad (4.22)$$

Model Implementation

As in Arthern, Eq. 4.6 and 4.7 can be written in the following form:

$$\mathcal{L}(\bar{\mathbf{u}})\bar{\mathbf{u}} = \mathbf{f} \quad (4.23)$$

where:

$$\mathcal{L} = \begin{bmatrix} \partial_x 4h\bar{\eta}\partial_x + \partial_y 2h\bar{\eta}\partial_y - C_{eff} & \partial_x 2h\bar{\eta}\partial_y + \partial_y h\bar{\eta}\partial_x \\ \partial_y 2h\bar{\eta}\partial_x + \partial_x h\bar{\eta}\partial_y & \partial_y 4h\bar{\eta}\partial_y + \partial_x h\bar{\eta}\partial_x - C_{eff} \end{bmatrix} \quad (4.24)$$

and

$$\mathbf{f} = \begin{bmatrix} \rho_i g h \partial_x s \\ \rho_i g h \partial_y s \end{bmatrix} \quad (4.25)$$

Equation 4.23 is a non-linear equation for depth integrated velocity. The non-linearity arises since depth integrated viscosity is a function of velocity, and in the case of a non-linear sliding law, since C_{eff} is also a function of velocity. The ice sheet model solves Eq. 4.23 on an Arakawa-C finite difference grid using a Picard iterative process.

Equation 4.23 is discretized following Arthern et al. (2015). The primary difference is that operators are appropriately extended to apply periodic boundary conditions in the ISMIP-HOM experiments. Discretization of Eq. 4.23 results in a linear system of equations, which can be written as:

$$\mathbf{L}\bar{\mathbf{x}} = \mathbf{b} \quad (4.26)$$

where the matrix (\mathbf{L}) corresponds to the operator \mathcal{L} , while the vector \mathbf{x} corresponds to $\bar{\mathbf{u}}$, and the vector \mathbf{b} corresponds to \mathbf{f} . Matlab's backslash operator is used to solve this system of equations. Alternatively, preconditioned iterative methods can be used (Arthern et al., 2015; Goldberg and Heimbach, 2013).

The Picard iteration linearizes Eq 4.23 by constructing \mathbf{L} using the velocity of the previous iteration. An initial velocity guess and viscosity guess form the initial \mathbf{L} . Eq. 4.23 is then solved for an updated velocity guess, which in turn can be used to update viscosity and C_{eff} . This process is repeated within a loop until the solution converges below a specified tolerance, or until a prescribed number of iterations are reached.

Evolution of surface-geometry is not included in the ice sheet model. This is appropriate since the ice-sheet model is applied on annual timescales, over which significant changes in ice sheet geometry are not expected.

4.3.2 Inversion Model

Model Formulation

This section describes the details of an inversion code developed in conjunction with the ice sheet model. The methodology is based on Goldberg and Heimbach (2013). However, the implementation developed in this chapter has a more limited capability due to software limitations.

The cost function returns a scalar which measures the fit of the model to the observations. For the inversion code developed in this chapter, the cost function is defined as:

$$J = \gamma_1 \int_{\Gamma_s} w \cdot (U_{obs} - U_s)^2 d\Gamma_s + \gamma_2 \int_{\Gamma_b} (\nabla \alpha \cdot \nabla \alpha) d\Gamma_b \quad (4.27)$$

where γ_1 and γ_2 are user-defined scaling factors, Γ_s is the surface domain, Γ_b is the basal domain, $w(x, y)$ is a weighting function, $U_{obs}(x, y)$ are observed surface ice speeds, $U_s(x, y)$ are modelled surface speeds, and $\alpha(x, y)$ is the control parameter,

The cost function defined above has two terms: $J = \gamma_1 J_0 + \gamma_2 J_{Reg}$. The first term (J_0) measures the weighted square of the difference between observed and modelled velocity. The second term (J_{Reg}) is a Tikhonov regularization term, which penalizes oscillations in α and stabilizes the inversion (Morlighem et al., 2013). Other formulations of the cost function are possible (e.g. Morlighem et al. (2013)).

The weighting function scales the mismatch between the observed and modelled surface velocities. It is used to incorporate a-priori knowledge about the quality of observations. Observations known to greater precision can be weighted higher, such that they have greater influence on the cost function than observations with a high error. The inverse of the variance of measurements is a statistically desirable weighting function.

The control parameter refers to the variable which the inversion process optimizes in order to best match model prediction and observations. Since the aim of this chapter is to determine the basal drag, the control parameter is a parameter in the basal sliding law. For the linear sliding law, $\alpha = \beta^2$. For the generalized Weertman sliding law, $\alpha = \mu_a$. Although the Schoof sliding law has two unknowns which can be inverted for, μ_b exerts a dominating control. Hence, λ_b is set to a constant while $\alpha = \mu_b$. In the numerical implementation of the adjoint, α is parameterized as $\alpha(x, y) = \exp(\zeta(x, y))$. This ensures that α remains positive, as expected for each of the three sliding laws. For simplicity, this is neglected in the remainder of the thesis, and the discussion focuses on recovering α rather than ζ .

The inversion process aims to determine the field of α which minimizes the cost function. This is an optimization problem. Starting with an initial guess for α , the gradient of the cost function with respect to α , is determined. The gradient provides a search direction for

the optimization algorithm, which updates α . This process is repeated iteratively until α converges below a tolerance or until a maximum number of iterations occur. The critical component in this process is the gradient $\frac{dJ}{d\alpha}$. The process to calculate this gradient is described in the next two subsections.

Adjoint model description

The methodology to obtain the gradient $\frac{dJ}{d\alpha}$ follows from Goldberg and Heimbach (2013). The key concepts of this approach are first explained for a generic algorithm, before showing how they can be applied to the ice sheet model. This explanation follows that of Errico (1997) and Goldberg and Heimbach (2013).

Consider the model:

$$b = B(\boldsymbol{\phi}) \quad (4.28)$$

where $\boldsymbol{\phi}$ is an arbitrary variable (or array of variables), and B can be considered a sequence of operations:

$$B(\boldsymbol{\phi}) = B_N(\dots(B_2(B_1(B_0(\boldsymbol{\phi})))))) \quad (4.29)$$

and each operation can be written as $b_N = B_N()$

Further, define a function J:

$$J = J(b) \quad (4.30)$$

where J returns a scalar. In the context of the adjoint model, the function is known as the cost function, objective function, or target function (Goldberg and Heimbach, 2013). This function quantifies an aspect of the model output which is of interest, such as the mean error of model output relative to observations.

The aim is to determine the gradient of the cost function J with respect to in the initial input $\boldsymbol{\phi}$. To provide context for the adjoint model, the tangent linear model (TLM) is presented first. In the TLM, a small perturbation in the input is propagated forward through the model to determine the corresponding perturbation in the output. Applying the chain rule to $J = J(b) = J(B(\boldsymbol{\phi}))$ leads to the corresponding TLM:

$$\delta J = \left(\prod_{i=N}^1 \frac{\partial b_i}{\partial b_{i-1}} \right) \frac{\partial b_0}{\partial \phi_i} \delta \phi_i \quad (4.31)$$

There are several observations about the TLM. First, the TLM determines the perturbation of δJ from the perturbation of a single element ϕ_i . As the perturbation $\delta \phi_i$ approaches zero, $\frac{\delta J}{\delta \phi_i}$ converges to $\frac{dJ}{d\phi_i}$. Second, to determine $\frac{dJ}{d\phi}$, the TLM needs to be run for each entry in $\boldsymbol{\phi}$. Although for small models this approach is feasible, the computational cost is too great

for glaciological problems on domains of the size of interest. Finally, the TLM acts in a similar direction as the model B, in that the functions are applied successively starting with the counterpart to B_0 (Errico, 1997).

The concept behind the adjoint model is that rather than determining how changes in the input ϕ impact the cost function J, it can be more efficient to determine how changes in the cost function J impact the initial input ϕ . In the adjoint model, sensitivities of J are propagated backwards through the model, to determine the resulting change in ϕ . Similar to the TLM, the adjoint model is derived by applying the chain rule to $J = J(b) = J(B(\phi))$:

$$\frac{\partial J}{\partial \phi} = \left(\prod_{i=1}^N \left[\frac{\partial b_i}{\partial b_{i-1}} \right]^T \right) \frac{\partial J}{\partial b_N} \quad (4.32)$$

Key observations about the adjoint model are: 1. In contrast to the TLM, which acts upon a perturbation, the adjoint model acts upon the sensitivity of the cost function. 2. A single run of the adjoint model is sufficient to determine the gradient $\frac{\delta J}{\delta \phi}$. 3. The adjoint model runs in reverse relative to both the model and the TLM, in that the adjoint model applies functions beginning with the counterpart to B_N and ending with the counterpart of B_0 (Errico, 1997).

Adjoint model implementation

The adjoint model is generated based on automatic differentiation (AD, Griewank and Walther (2008)) of the Matlab code implementations of the forward model. AD tools process an input code to generate a counterpart code which returns the corresponding gradient (or Jacobian). The central concept behind AD is that a computer program is fundamentally a sequence of elementary operations and functions. This admits the repeated application of the chain rule to generate a derivate of high accuracy.

Multiple methodologies exist for AD tools to generate the derivate code. Previous application of AD software to generate the adjoint in glaciology (Goldberg and Heimbach, 2013; Heimbach and Bugnion, 2009; Martin and Monnier, 2014) have used reverse accumulation AD tools (e.g. Giering et al., 2005; Hascoet and Pascual, 2004). These types of AD software are conceptually similar to the adjoint model. They are designed to determine the gradient of function (input code) by propagating sensitivities of the output variables backwards to the input variables. Hence, an ice sheet model can be processed with relatively little modification by reverse accumulation AD tools to generate the adjoint model.

In this chapter we apply the open source AD tool ADiGator (Weinstein and Rao, 2016), which in contrast to previous work is a forward accumulation AD tool. The methodology of forward accumulation is conceptually similar to the TLM. It is designed to determine the

gradient of a function (input code) by propagating sensitivities of the input variables forward through the program to the output. Applying a forward AD tool to generate the adjoint of an ice sheet model is not feasible due to the size of the control space.

Before describing the process of constructing the adjoint model, the application of ADiGator to a simple piece of code is shown. Algorithm 1 is a matlab function implementing the function $f(x) = 2 * x^2 + 1$. Algorithm 2 shows the corresponding AD function $f_AD(x)$ generated by ADiGator. The function $f_AD(x)$ returns the value of $\frac{df(x)}{dx}$. In contrast to $f(x)$ which takes a scalar as input, the function $f_AD(x)$ takes an object defined by ADiGator as input. This object is used to track how perturbations in the input propagate through the function. Elementary operations such as `sum()` and `prod()` are overloaded by ADiGator to allow them to act upon this object. Similar to the function $f(x)$, which can also take an array of arbitrary dimensions as input, an ADiGator object representing an array of arbitrary dimensions can be passed to $f_AD(x)$. In Algorithm 2, lines 8 to 13 correspond to the line 2 in Algorithm 1, which performs the algebraic operations. Algorithm 2 also loads the datafile 'f_AD.mat'. This is automatically generated by ADiGator during the processing of Algorithm 1, and stores information about the function and its inputs. This simple example also illustrates that processing a function with ADiGator generates a second function. From a programming perspective, using the AD generated code is as simple as calling any other function, and there is no prerequisite of understanding/manipulating the AD generated code. Processing a function which outputs a vector with ADiGator to calculate the Jacobian is implemented the same way as calculating the derivative of a function which outputs a scalar.

Algorithm 1 Sample matlab function

```

1: function [ y ] = f( x )
2: y = 2*x.^2 + 1;
3: end

```

Pseudocode of the main ice sheet model routine is shown in Algorithm 3, and the corresponding code to calculate the adjoint is shown in Algorithm 4. Two new functions, S1 and S2 appear in the adjoint code. These encapsulate segments of code from the forward model and can be processed by ADiGator. The function S2 contains code which spans over two Picard iterations. The adjoint does not contain a for loop corresponding to iterating through the Picard iterations in reverse (c.f. Goldberg et al. (2016)). Rather, values from the final two Picard iterations of the forward model are saved and used as input for the adjoint code. The adjoint model is also modified to solve the cubic equation (following Arthern et al. (2015)) to determine η , rather than storing values from the previous iterations and

Algorithm 2 Automatically differentiated sample Matlab function using ADiGator

```
1: function y = f_AD(x)
2:
3: global ADiGator_f_AD
4: if isempty(ADiGator_f_AD); ADiGator_LoadData(); end
5: Gator1Data = ADiGator_f_AD.f_AD.Gator1Data;
6:
7: %ADiGator Start Derivative Computations
8: cada1f1dx = 2.*x.f^(2-1).*x.dx;
9: cada1f1 = x.f.^2;
10: cada1f2dx = 2.*cada1f1dx;
11: cada1f2 = 2*cada1f1;
12: y.dx = cada1f2dx;
13: y.f = cada1f2 + 1;
14: %User Line: y = 2 * x.^2 + 1;
15:
16: y.dx_size = 1;
17: y.dx_location = 1;
18: end
19:
20:
21: function ADiGator_LoadData()
22: global ADiGator_f_AD
23: ADiGator_f_AD = load('f_AD.mat');
24: return
25: end
```

implementing a fixed point iteration. This impacts the η , $\bar{\eta}$, and F_a functions, but leaves the overall structure the same. This is a necessary modification for ADiGator.

The adjoint code explicitly calculates several Jacobian matrices (lines 15 to 23 in Algorithm 4). ADiGator is applied to the corresponding functions to generate the Jacobian matrices, except the solution to the system of linear equations, which requires special treatment. A counterpart to the linear solves which returns the corresponding derivate is manually programmed following the procedure detailed in the appendix of Martin and Monnier (2014). The adjoint is then calculated by multiplying out the sensitivities of the cost function with the transposes of the Jacobian matrices. Although this process is more complicated and less flexible than previous approaches, it is necessary as no non-commercial AD reverse accumulation tool is available for Matlab.

This implementation of the adjoint is equivalent to previously published adjoint implementations (Goldberg and Heimbach, 2013; Martin and Monnier, 2014) restricted to one reverse step in the Picard iteration. This is mathematically equivalent to the Lagrangian Multiplier method introduced by MacAyeal (1993) (Heimbach and Bugnion, 2009).

The gradient from the adjoint model is used to solve the optimization problem which minimizes the cost function. The inversion code relies on minFunc (Schmidt, 2005), a publicly available Matlab unconstrained optimization package. The L-BFGS routine, with a Wolfe Condition backtracking line search, is applied in the inversion code. The cost function is discretized using the same finite difference operators as the ice sheet model.

Algorithm 3 Ice sheet model main routine pseudocode

```

1: Initialize:  $u, \eta, C, C_{eff}, \alpha$  ▷ From SIA
2:
3: for  $j = 1, 2, 3, \dots, N$  do ▷ Picard Iterations
4:    $\eta = \boldsymbol{\eta}(u, \eta, C_{eff})$  ▷ Viscosity (Eq. 4.14)
5:    $\bar{\eta} = \bar{\boldsymbol{\eta}}(\eta)$  ▷ Depth integrated Viscosity (Eq. 4.40)
6:    $F_2 = \mathbf{F}_a(\eta, a = 2)$  ▷ F-integral (Eq. 4.18)
7:    $C = \mathbf{C}(u, \alpha, C, F_2)$  ▷ Basal drag parameter (Eq. 4.11)
8:    $C_{eff} = \mathbf{C}_{eff}(C, F_2)$  ▷ Effective basal drag parameter (Eq. 4.21)
9:
10:   $u = \mathbf{u}(C_{eff}, \bar{\eta})$  ▷ Velocities (Eq. 4.26)
11: end for
12:
13:  $J = \mathbf{J}(u, C_{eff}, \alpha)$  ▷ Cost Function Eq. 4.32

```

Algorithm 4 Pseudocode of the adjoint code

```

1: function S1( $u, \alpha, C, F2$ )                                ▷ Encapsulate segments of code into functions
2:    $C = \mathbf{C}(u, \alpha, C, F2)$ 
3:    $C_{eff} = \mathbf{C}_{eff}(C, F2)$ 
4:   return  $C_{eff}$ 
5: end function
6:
7: function S2( $u, \alpha, C, F2$ )
8:    $C = \mathbf{C}(u, \alpha, C, F2)$ 
9:    $C_{eff} = \mathbf{C}_{eff}(C, F2)$ 
10:   $\eta = \boldsymbol{\eta}(u, \eta, C_{eff})$ 
11:   $\bar{\eta} = \bar{\boldsymbol{\eta}}(\eta)$ 
12:  return  $\bar{\eta}$ 
13: end function
14:
15:  $DJ|_u = \mathbf{ADiGator}(\mathbf{J}, u^N, C_{eff}^N, \alpha)$                 ▷ Calculate Jacobian matrices ( $Df|_p = \frac{\partial f_i}{\partial p_j}$ )
16:  $DJ|_{C_{eff}} = \mathbf{ADiGator}(\mathbf{J}, u^N, C_{eff}^N, \alpha)$ 
17:  $DJ|_\alpha = \mathbf{ADiGator}(\mathbf{J}, u^N, C_{eff}^N, \alpha)$ 
18:
19:  $DS1|_\alpha = \mathbf{ADiGator}(\mathbf{S1}, u^{N-1}, \alpha, C_{eff}^{N-1}, F_2^N)$ 
20:  $DS2|_\alpha = \mathbf{ADiGator}(\mathbf{S2}, u^{N-1}, \alpha, C_{eff}^{N-1}, F_2^{N-1})$ 
21:
22:  $Du|_{C_{eff}} = \mathbf{U\_jac}(u^N, C_{eff}^N, \bar{\eta})$                 ▷ The Jacobian of the velocity solve is calculated
23:  $Du|_{\bar{\eta}} = \mathbf{U\_jac}(u^N, C_{eff}^N, \bar{\eta})$                 ▷ using a manually programmed function
24:
25:  $\frac{dJ}{d\alpha} = (DS1|_\alpha)^T (Du|_{C_{eff}})^T (DJ|_u) +$                 ▷ The adjoint (Eq. 4.32)
     $(DS2|_\alpha)^T (Du|_{\bar{\eta}})^T (DJ|_u) +$ 
     $(DS1|_\alpha)^T (DJ|_{C_{eff}}) + DJ|_\alpha$ 

```

4.3.3 Subglacial Hydrology Model

This subglacial hydrology model used is described in detail in Hewitt (2013) and Banwell et al. (2016), and similar conceptually to the model presented in Werder et al. (2013). In this thesis, the version employed in Banwell et al. (2016) is applied.

Both distributed and channelized flow are represented in the subglacial hydrology model. Distributed flow is described by an average thickness and flux over a representative area. As in Banwell et al. (2016), the distributed system is composed into two components: a cavity sheet, and an elastic sheet. The elastic sheet is included to simulate 'hydraulic jacking' from lake hydrofracture events, and is activated only when the effective pressure drops to zero and below. Channels have the potential to form along the edges and diagonals of the numerical grid. Channels are initiated by dissipative heating from the distributed system over an incipient channel width lengthscale. The model is written in Matlab, using a finite difference numerical grid, and an implicit forward time step method. For full details, consult Hewitt (2013) and Banwell et al. (2016). The model equations and parameter values can be found in Chapter 5, since the model calibration is described there.

4.3.4 Test Simulations

ISMIP-HOM

ISMIP-HOM provides a set of standardized simulations which can be used to verify ice sheet models. The ice sheet model developed in this chapter is verified using two experiments from ISMIP-HOM: A and C. We compare the results of our simulations with that of previous ice sheet models, and demonstrate that the outputs compare favorably.

Experiment A of ISMIP-HOM is on a square domain, with periodic boundary conditions on the lateral margins. Surface topography and basal topography are prescribed by:

$$s(x, y) = -x \cdot \tan(0.5^\circ) \quad (4.33)$$

$$b(x, y) = s(x, y) - 1000 + 500\sin(\omega x)\cos(\omega y) \quad (4.34)$$

where $\omega = \frac{2\pi}{L}$, $0 \leq x, y \leq L$, and L is the domain length. This experiment assumes no basal sliding. This is approximated in our model by using the linear sliding law with a high basal drag coefficient ($3 \cdot 10^{14} \text{ Pa s m}^{-1}$).

Experiment C of ISMIP-HOM is also on a square domain with periodic boundary conditions at the lateral margins. Surface topography and basal topography are prescribed by:

$$s(x, y) = -x \cdot \tan(0.1^\circ) \quad (4.35)$$

Symbol	Constant	Value	Units
A	Ice-flow parameter	10^{-16}	$\text{Pa}^n \text{yr}^{-1}$
ρ_i	Ice Density	910	kg m^{-3}
g	Gravitational constant	9.81	m s^{-2}
n	Exponent in Glen's Flow law	3	
t_y	Seconds per year	31556926	s yr^{-1}

Table 4.1 Constants for ISMIP-HOM experiments. Reprinted from Gagliardini and Zwinger (2008).

$$b(x,y) = s(x,y) - 1000 \quad (4.36)$$

Experiment C allows for basal sliding, using a linear sliding law, with the basal drag coefficient prescribed by:

$$\beta = [1000 + 1000 \sin(\omega x) \cos(\omega y)] \cdot t_y^{-1} \quad (4.37)$$

where t_y is the number of seconds in a year, converting β to SI units.

Both experiments are run at three domain lengths: 10 km, 40 km, and 80 km. The parameters used in the model run are prescribed for the ISMIP-HOM experiments, and are listed in Table 4.1.

Inversion Twin Tests

The inversion code is validated using a series of 'identical twin' tests. These tests are composed of a forward run of the ice sheet model, followed by an inversion run. The forward run utilizes a prescribed sliding law, with known values for all parameters, to solve for the velocity field. The inversion run attempts to recover the values of the sliding law parameters using the velocity field output by the forward run. Model validation results are shown in Section 4.4.1.

Three twin tests are performed, corresponding to the sliding laws implemented in the ice sheet model. Each of these tests uses the same basal and surface topography as Experiment C of ISMIP-HOM. In addition, we keep the same constants (Table 4.1). The domain length of the experiment are set to 40 km, and an 80x80 grid is used. Fifty vertical layers are used for integration with Simpson's rule. For the optimization algorithm, a limit of 100 iterations is set. The optimization algorithm minimizes the cost function (Eq. 4.27), with scaling factors set to $\gamma_1 = 10^{10}$ and $\gamma_2 = 0$. These factors scale the first term appropriately for the optimization routine and eliminate the Tikhonov regularization term. There is no observational error to account for in the ISMIP-HOM experiments, so the weighting function

is set to be one at all grid points. The control parameter is initialized with a value equal to the mean of the prescribed values in the forward model described below.

The twin test of the linear sliding law uses the prescribed basal drag from Experiment C (Eq. 4.37). Using the output of the forward run, the inversion procedure aims to reconstruct the basal drag coefficient field (β).

In both the generalized Weertman sliding law and Schoof sliding law twin tests, effective pressure is prescribed by:

$$N = 0.1 \cdot \rho_i g (s - b) \quad (4.38)$$

The forward run with the generalized Weertman sliding law uses a drag coefficient prescribed by:

$$\mu_a = 2.5 \cdot [10^4 + 10^6 \cdot \sin(\omega x) \cos(\omega y)] \quad (4.39)$$

This spatial distribution reflects that of the basal drag coefficient in Experiment C, with the magnitude of μ_a selected to result in a similar velocity profile. The exponents of the generalized Weertman law (p and q) are both set to $\frac{1}{3}$. The inversion component of the identical twin test aims to recreate the prescribed μ_a profile.

For the Schoof sliding law identical twin test, the state parameter is μ_b . For the forward run, it is prescribed to be:

$$\mu_b = 35 \cdot [10^{-3} + 10^{-4} \cdot \sin(\omega x) \cos(\omega y)] \quad (4.40)$$

The distribution and magnitude of μ_b was selected for similar reasons as μ_a in the generalized Weertman sliding law twin test. Following Hewitt (2013), the bed roughness scale (λ_b) is set to 1. In this twin test, the inversion process aims to reconstruct the distribution of μ_b .

4.3.5 Application to Russell Glacier Area

The Russell Glacier area is a land-terminating sector of the GrIS (Figure 4.1). It serves as a study site in this, and the following, chapter. In this chapter, the ice sheet model and inversion code are applied to determine the basal boundary condition at the end of the winter season. This serves the purpose of an initialization of the model for the work in the following chapter.

An outline of the study area is shown in (Figure 4.1). The northern and southern boundaries are selected to be roughly in line with basal watersheds determined using the Shreve (1972) approximation for hydraulic gradient. The northern boundary is approximately the same as used by Bougamont et al. (2014) and de Fleurian et al. (2016). The southern boundary is further south relative to Bougamont et al. (2014), but north of the southern

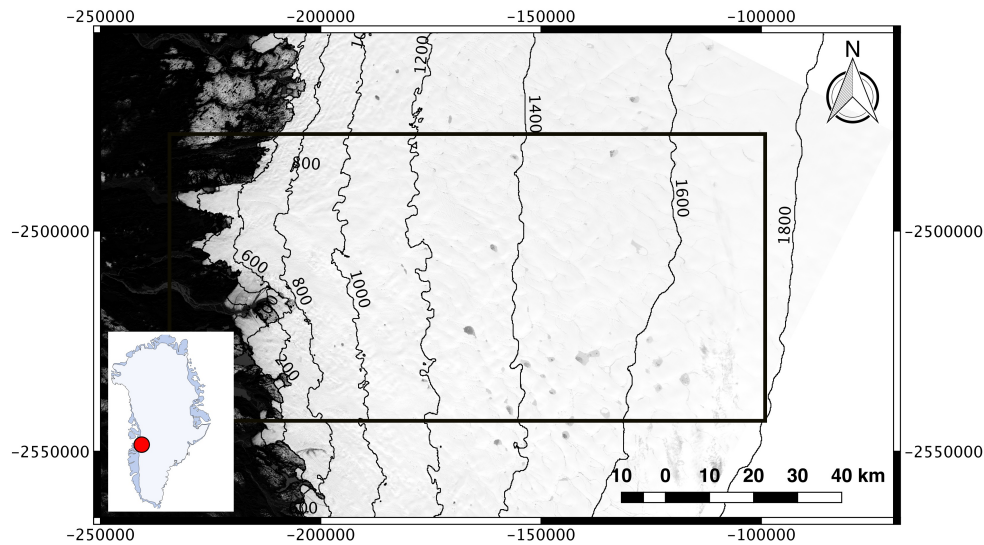


Fig. 4.1 Landsat 8 satellite image, band 2, showing the Russell Glacier area. Black box outlines the study area. Inset shows the location in reference to Greenland.

boundary in de Fleurian et al. (2016). The eastern boundary was selected to extend up ice of the GPS stations (Tedstone and Neino, 2017) in the area (see Chapter 5). The eastern boundary also extends up ice of moulines observed in the study site during the 2013 summer season by (Yang and Smith, 2016). The western boundary is the ice-margin. There is a nunatak near the western boundary.

The ice sheet model/inversion code are applied to determine the basal boundary condition at the end of the 2008-2009 winter season in the Russell Glacier study site. The end of the winter season is assumed to be day 120 of the year (April 30th). Although the exact day is somewhat arbitrary, this day was selected as it is shortly before surface runoff begins in the study area, and shortly before GPS records in the study site show enhanced motion. Hence, it is also appropriate as the start of the summer season for the next chapter.

Applying the ice sheet model/inversion code to the Russell Glacier area requires a number of datasets. Mean winter surface velocities for 2008/2009 (Figure 4.2) are provided by the MEaSUREs Greenland Ice Sheet Velocity Map at 500 m resolution (Joughin et al., 2010a,b). Surface and basal topography (Figure 4.3) are provided by the BedMachine2 dataset (Morlighem et al., 2014, 2015b), and are interpolated to 500 m resolution from 150 m resolution to match the velocity data. This is slightly coarser than the reported true resolution of 400 m for the ice thickness. The 500m grid resolution results in a grid size of 132x274 for the domain. Fifty vertical layers are used for integration using Simpson's rule.

An important assumption made is that the mean winter velocities are representative of both the beginning and end of winter. This assumption is justified by observing published

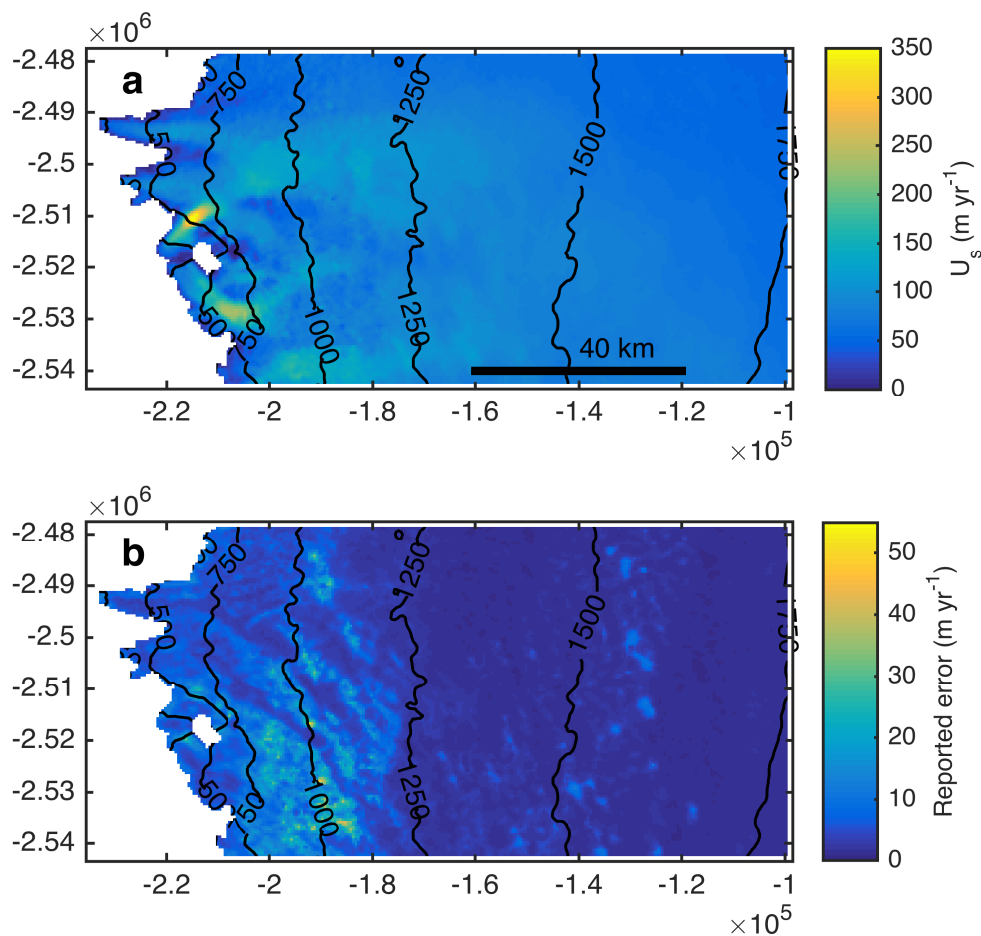


Fig. 4.2 a) Velocity measurements from the MEaSUREs Greenland Ice Sheet Velocity Map at 500 m resolution for the Russell Glacier area (Joughin et al., 2010a,b). b) Reported error for the measurements.

GPS records in Southwest Greenland (Colgan et al., 2012; van de Wal et al., 2015). These observations show that although velocities increase throughout the winter, the magnitude of the change is relatively limited.

Inversions are initialized using a basal drag set to the local driving stress smoothed by a 3x3 grid cell mean filter. The ice-margin boundary is described in the ice sheet model by Eq. 4.12 and 4.13 while on the three other boundaries a Dirichlet boundary condition is applied. The inverse of the errors provided with the surface velocity measurements are used as weights in the cost function.

The results of inversions depends on the relative values of the scaling factors γ_1 to γ_2 in the cost function (Eq. 4.27). For each sliding law, a series of inversions is performed with γ_1 set to 1 while varying γ_2 . A L-curve analysis is applied to select the inversion which best balances fitting the velocity observations while penalizing spurious oscillations in basal drag.

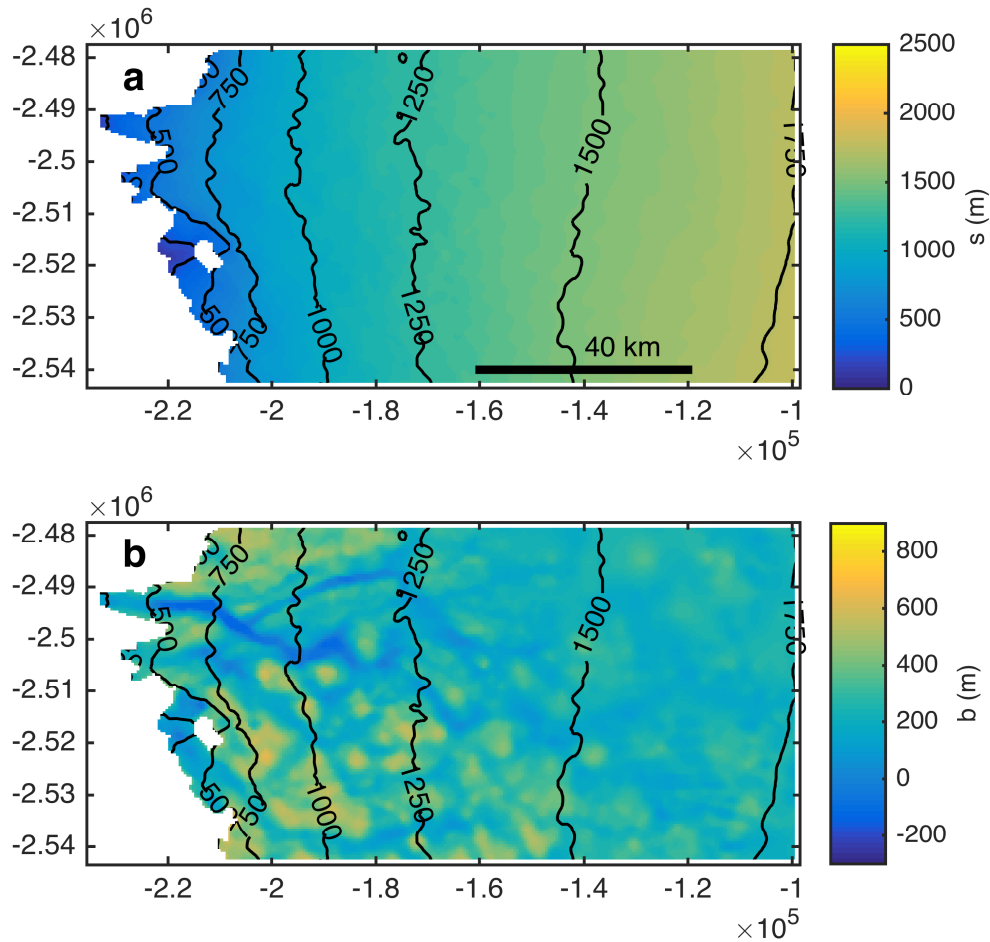


Fig. 4.3 a) Surface topography from BedMachine2 dataset (Morlighem et al., 2014, 2015b) reinterpolated to 500 m. b) Basal topography at same resolution.

Parameters for the ice sheet model/inversion code are listed in Table 4.2. Similar to Hewitt (2013), the ice flow creep parameter (A) is selected to be $7 \cdot 10^{-25} \text{ Pa}^3 \text{ s}^{-1}$. This corresponds to an ice temperature of approximately -7° (Cuffey and Paterson, 2010). This choice for A results in the ratio of basal velocity to surface velocity remaining greater than 0.5 throughout the study area.

The parameters for the subglacial hydrology are the result of an extensive parameter search using a coupled ice-flow/subglacial hydrology model in Chapter 5. Many of the parameters are the same as published in Banwell et al. (2016) and Hewitt (2013). However, testing of the reported optimal parameters for the Paakitsoq region reported by Banwell et al. (2016) using the integrated model showed poor agreement with GPS measurements due to insufficient volumes of water being evacuated from mid-elevations.

The workflow developed for incorporating modelled effective pressure into inversions using non-linear sliding laws is shown in Figure 5.4. This workflow is motivated by the idea

Symbol	Constant	Value	Units
A	Ice-flow parameter	$7 \cdot 10^{-25}$	$\text{Pa}^n \text{s}^{-1}$
A_b	Ice-flow parameter for basal ice	$7 \cdot 10^{-24}$	$\text{Pa}^n \text{s}^{-1}$
ρ_i	Ice density	917	kg m^{-3}
g	Gravitational constant	9.81	m s^{-2}
n	Exponent in Glen's flow law	3	
p	Exponent generalized Weertman sliding law	3^{-1}	
q	Exponent generalized Weertman sliding law	3^{-1}	
λ_b	bed roughness scale	1	m
t_y	Seconds per year	31536000	s yr^{-1}
ε	viscosity regularization parameter	$1 \cdot 10^{-14}$	m s^{-1}

Table 4.2 Constants used in the ice sheet/inversion model applied to the Russell Glacier area.

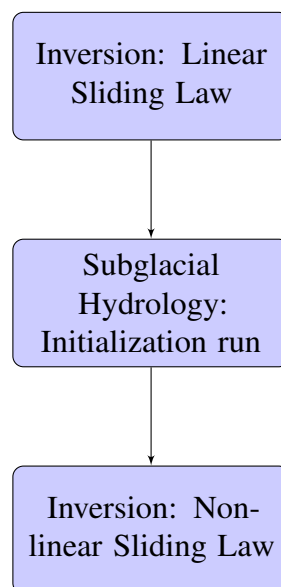


Fig. 4.4 Flow chart showing the work flow for non-linear inversions

that both the subglacial hydrological system and ice flow are in quasi-steady state during the winter. This allows us to invert for background values of the constants in the sliding laws. The initial step is to invert using a linear sliding law for the basal drag coefficient. Basal velocities are calculated from modelled depth integrated velocities (Eq. 4.20). The modelled basal drag and basal velocities then provide the necessary input for the subglacial hydrology model to calculate a distributed basal melt rate. The modelled distributed basal melt rate incorporates geothermal flux, but neglects heat loss to the interior of the ice sheet (Hewitt, 2013).

The subglacial hydrology model is then run for the winter season with the basal drag and basal velocities from the linear inversion. The model is run at 500m resolution (identical to the inversions), with no-flow boundary conditions at the northern, southern, and eastern boundaries. The ice-margin is assumed to be at atmospheric pressure. This boundary condition is modified at necessary places to prevent inflow of water from beyond the ice sheet margin. Similarly to Banwell et al. (2016), the subglacial hydrology model is initialized with the thickness of the sheet flow layer set to 0.10 m. Testing showed that varying initial thickness has negligible impact. At this stage, the ice sheet model remains unconnected, and the input basal velocities are assumed to be constant. The subglacial hydrology model run provides a modelled water pressure distribution over the study site.

Finally, the non-linear inversions are run using the modelled water pressure from the subglacial hydrology model winter run. Two sets of inversions are conducted, one for the generalized Weertman sliding law, and one for the Schoof sliding law. The first set of inversions seeks to determine the distribution of μ_a , while the second inverts for μ_b . Similar to the linear sliding law, an L-curve analysis is employed to determine the relative values of γ_1 to γ_2 .

4.4 Results

4.4.1 Model Verification

ISMIP-HOM

Model outputs for Experiments A and C at domain lengths of 10 km, 40 km, and 80 km are comparable to previously published results (Figure 4.5 and 4.6). See Goldberg (2011) for a published comparison of the hybrid model to ISMIP-HOM experiments, and an in-depth discussion of the characteristics of the hybrid model. As in Goldberg (2011), the hybrid model compares less favourably in the SIA regime, particularly at low domain lengths (Figure 4.5).

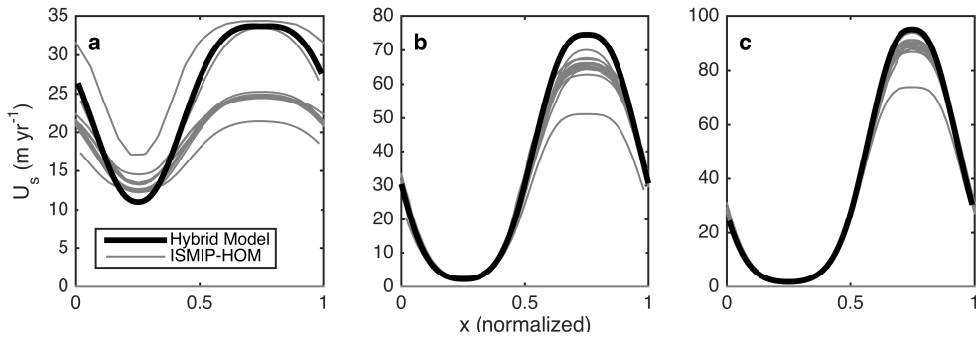


Fig. 4.5 Surface velocity for the ISMIP-HOM Experiment A at: (a) 10 km, (b) 40 km and (c) 80 km domain lengths along the profile at $y=0.25$ along the normalized y -axis.

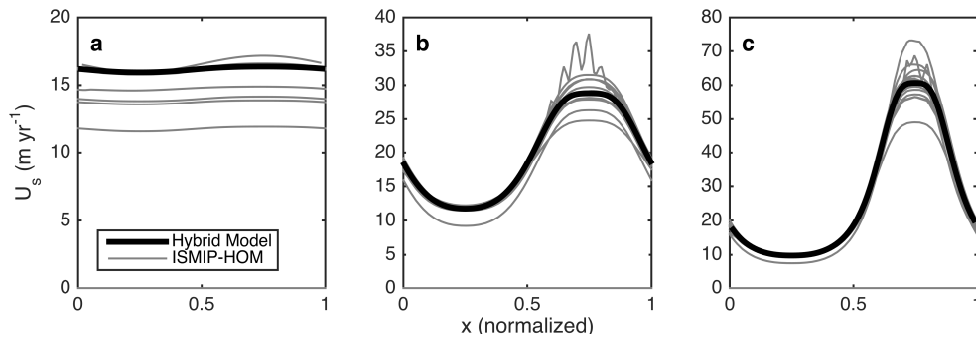


Fig. 4.6 Surface velocity for the ISMIP-HOM Experiment C at: (a) 10 km, (b) 40 km and (c) 80 km domain lengths along the profile at $y=0.25$ along the normalized y -axis.

Finite differences introduces truncation error into the numerical solution. As we refine our numerical grid, this error should reduce. The model output reflects this, with both ISMIP-HOM Experiments A and C converging with increasing grid resolution (Figure 4.7).

For Picard iterations to converge to the solution, the iterative process must be stable. However, instability during Picard iterations is observed in the hybrid model depending on the simulation and method employed to calculate effective viscosity. Four different approaches to calculating effective viscosity are tested: 1. solving Equation 4.14 by approximating viscosity in the vertical shearing terms (Equations 4.15) using the previous timestep's value (as in Goldberg (2011)); 2. Iterating method 1 twice (for $j=1 \rightarrow 2$, $\eta_{curr} = \boldsymbol{\eta}(u, v, \eta_{prev})$ end); 3. Same as method 2, but iterating three times (for $j=1 \rightarrow 3$); 4. Substituting Equations 4.16 and 4.15 into Equation 4.14 and solving the cubic equation (as in Arthern et al. (2015)). All four of these approaches lead to stable convergence of the Picard iterations for Experiment C at 40km domain length (Figure 4.8b). In contrast, only two of the approaches are stable for Exp A, at 10km. In the latter, both the three iteration fixed point iteration, and cubic equation solver show divergence in the Picard iterations (Figure 4.8a).

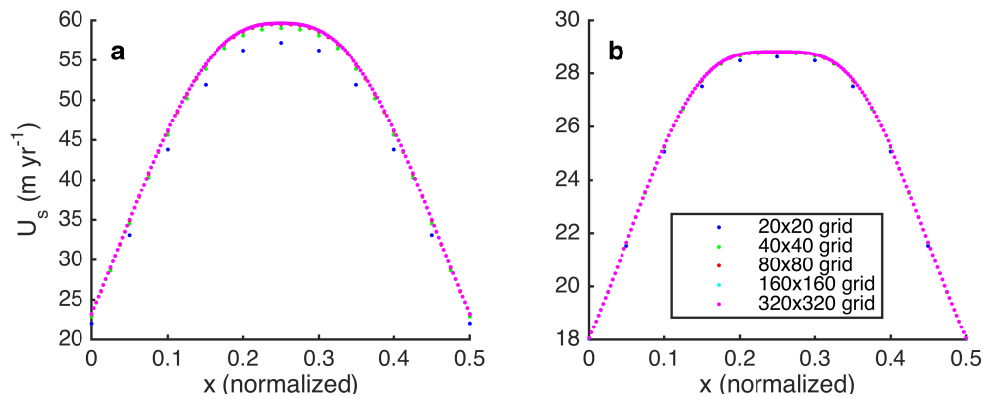


Fig. 4.7 Grid convergence for ISMIP-HOM Experiments at 40 km. a) Experiment A; b) Experiment C.

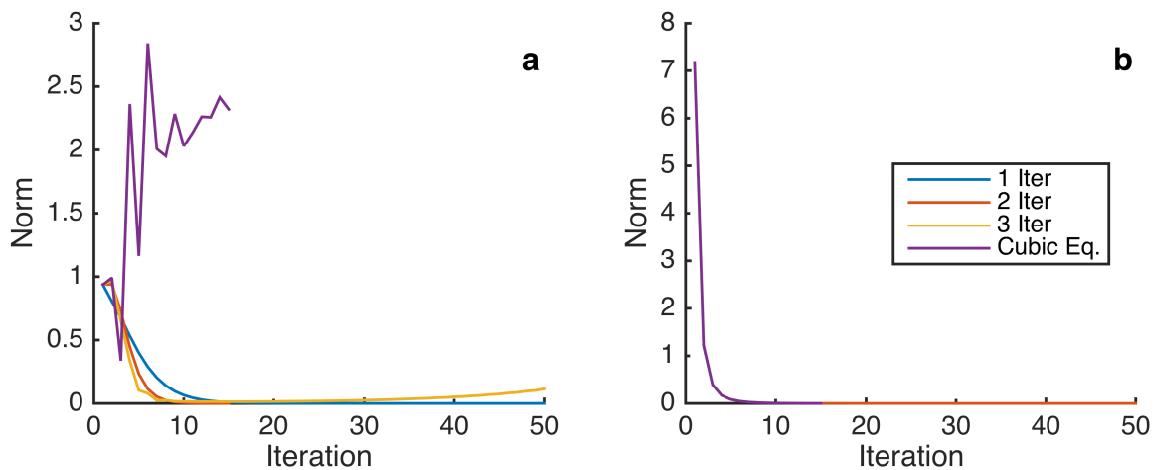


Fig. 4.8 Convergence of Picard Iterations for different methods of calculating viscosity. a) Experiment A at 10 km b) Experiment C at 40 km

Identical Twin Tests

The results of the identical twin test using the linear sliding law (Figure 4.9) show that starting from a uniform basal drag coefficient, the inversion procedure converges towards a basal drag field which produces a good match between the known velocity field and modelled velocity field. The velocity field produced by the inversion deviates by less than 0.04 m yr^{-1} from the control velocity field. The optimization routine terminates at the maximum iteration limit of 100. The basal drag coefficient field produced by the iteration process is similar to the known basal drag field. Deviation is greatest at 0.25 along the normalized x -axis. This does not coincide with the maximum difference between the known surface velocity and inversion surface velocity, which occurs at 0.75 along the normalized x -axis.

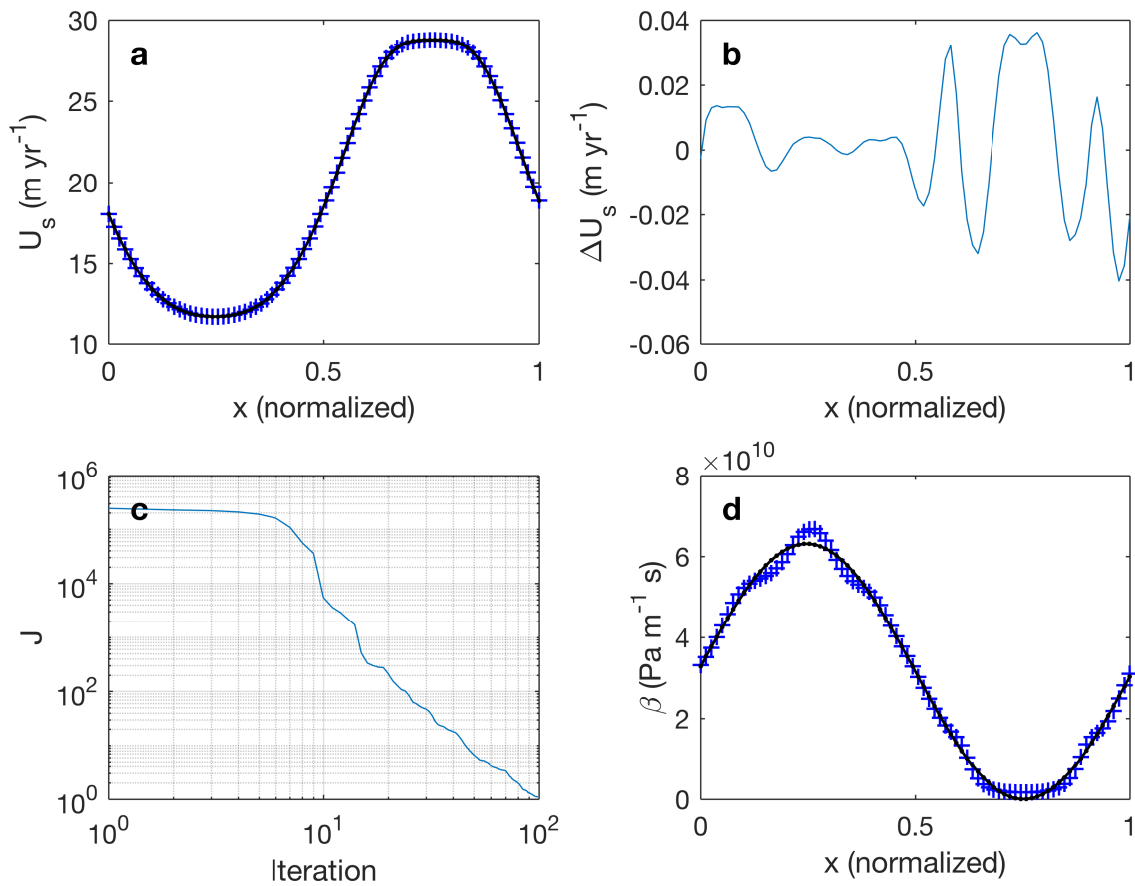


Fig. 4.9 Identical twin test for the linear sliding law, run on a 40 km square domain with a 80x80 grid. a) Surface velocities for the profile at $y = 0.25$ on the normalized y -axis, where black velocities are known values, and blue crosses show velocities from the inverted basal sliding law. b) Difference between known velocities and inversion velocities. c) Plot showing the minimization of the cost function with. d) Control parameter from the inversion overlaid (blue crosses) on the known values of the control parameter (black line) at the profile line at $y = 0.25$ on the normalized y -axis.

Solutions to the inversion problem are not unique. To investigate the equifinality of the solution, the twin test for the linear sliding law is repeated using the Tikhonov regularization term. Figure 4.10 demonstrates that different scalings of the Tikhonov regularization term lead to different basal drag distributions. However, the inversion surface velocity shows little change.

Twin tests with the non-linear sliding laws produce a good matches between the control velocity and modelled velocity (Figure 4.11 and 4.12). The mismatch between the control and inversion surface velocity shows a similar spatial pattern in all three twin tests. However the magnitude of the maximum difference increases to 0.26 when the generalized Weertman law is used, and 0.48 when the Schoof sliding law is used. Neither non-linear sliding laws

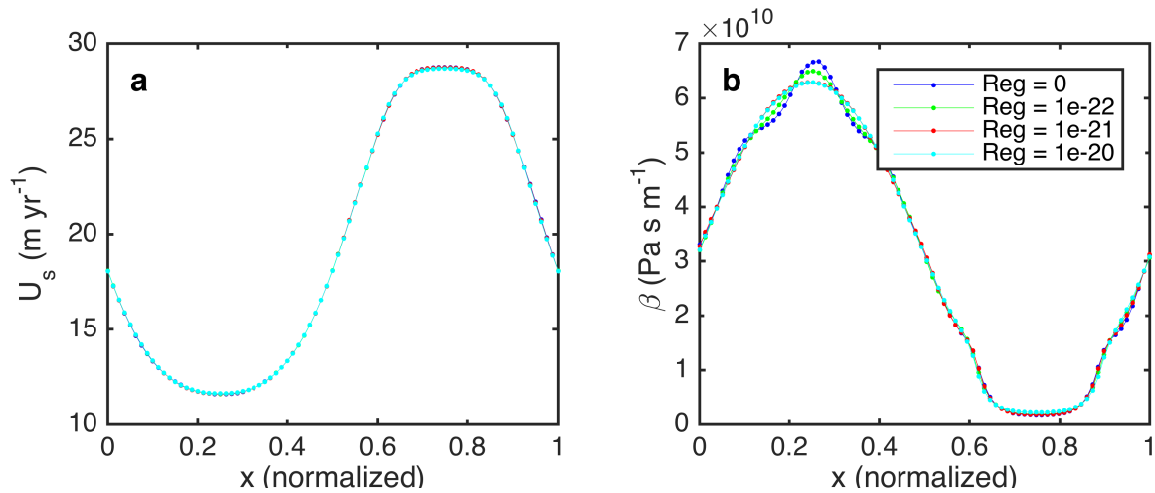


Fig. 4.10 Figure showing the equifinality of inversion results. a) Surface velocities for the profile at $y=0.25$ on the normalized y-axis for identical twin tests using different scaling factors for the Tikhonov regularization term in the cost function. b) Resulting control parameter from the inversion.

goes to 100 iterations in the minimization routine. Rather, they terminate from a lack of progress after 45 and 47 iterations for the generalized Weertman and Schoof sliding laws respectively.

The spatial pattern of the control parameter shows a similar pattern in the twin tests for all three sliding laws. Relative to the prescribed values, the inversion results in the control parameter having higher values and a narrower peak at around 0.25 along the normalized x-axis. The maximum value of the control parameter does not coincide with the maximum value of the prescribed value, but is slightly offset in the downhill direction (to the right). The values of points near the peak are not distributed symmetrically. The values of the control parameter reach a low that is greater than the low in the prescribed values, and show a broader depression around 0.75 of the normalized x-axis

4.4.2 Application to Russell Glacier Area

Linear Inversion

Six inversions using the linear sliding law are run (Figure 4.13). Using the L-curve plot, the inversion with $\gamma_2 = 1 \cdot 10^{-12}$ is selected as optimal. The value of J_0 for this inversion is $1.56 \cdot 10^{11}$.

The inversion converges in 46 iterations (Figure 4.14). The histogram of the the difference between observed and modelled velocities (Figure 4.15) has a maximum in the lowest bin,

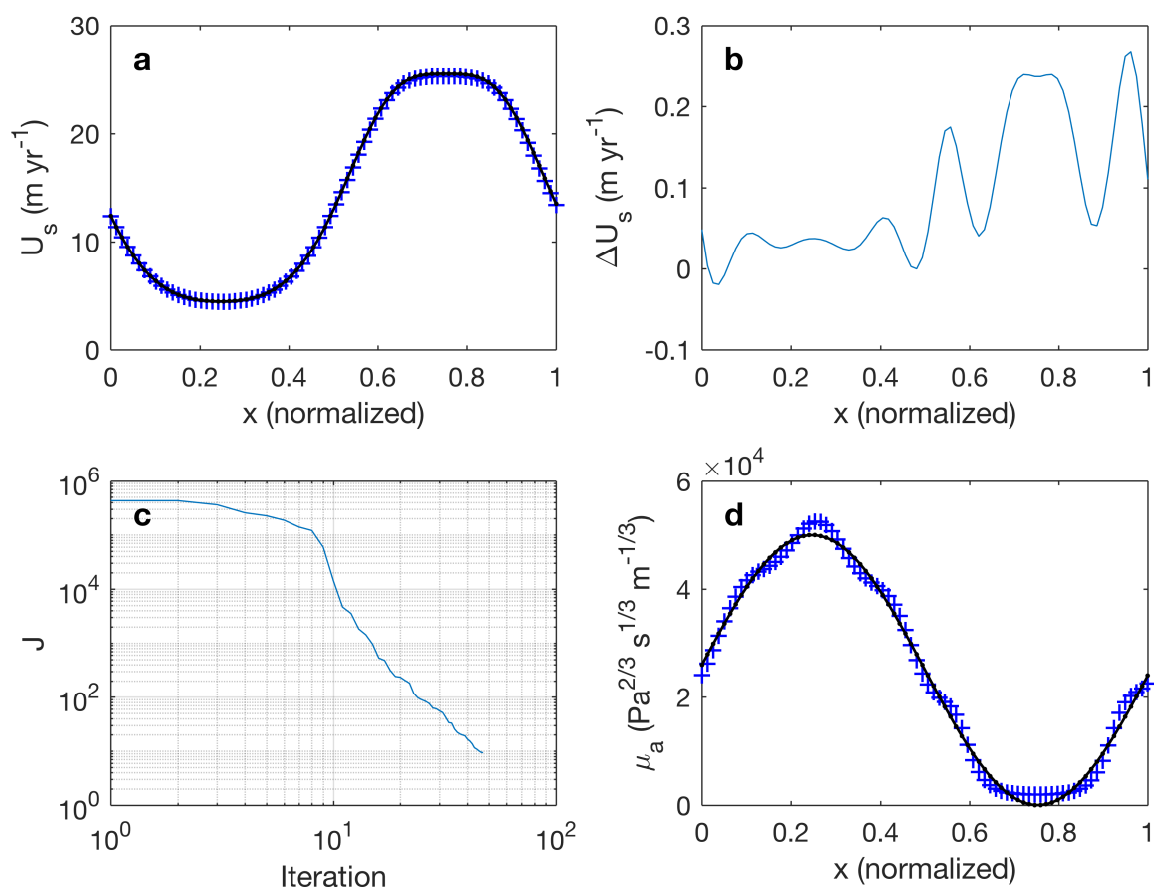


Fig. 4.11 Identical twin test for the generalized Weertman sliding law, run on a 40 km square domain with a 80x80 grid. a) Surface velocities for the profile at $y = 0.25$ on the normalized y -axis, where black velocities are known values, and blue crosses show velocities from the inverted basal sliding law. b) Difference between known velocities and inversion velocities. c) Plot showing the minimization of the cost function with. d) Control parameter from the inversion overlaid (blue crosses) on the known values of the control parameter (black line) at the profile line at $y = 0.25$ on the normalized y axis.

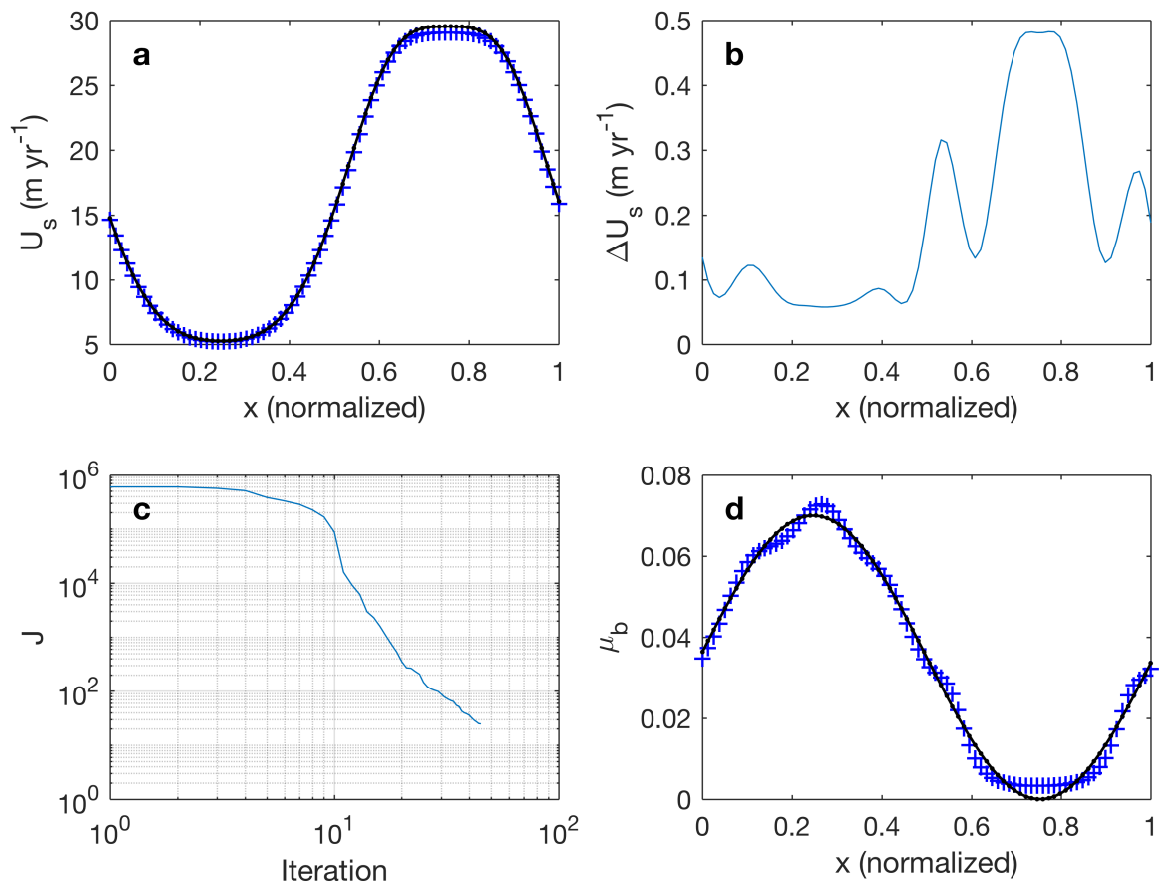


Fig. 4.12 Identical twin test for the generalized Schoof sliding law, run on a 40 km square domain with a 80x80 grid. a) Surface velocities for the profile at $y = 0.25$ on the normalized y -axis, where black velocities are known values, and blue crosses show velocities from the inverted basal sliding law. b) Difference between known velocities and inversion velocities. c) Plot showing the minimization of the cost function with. d) Control parameter from the inversion overlaid (blue crosses) on the known values of the control parameter (black line) at the profile line at $y = 0.25$ on the normalized y axis.

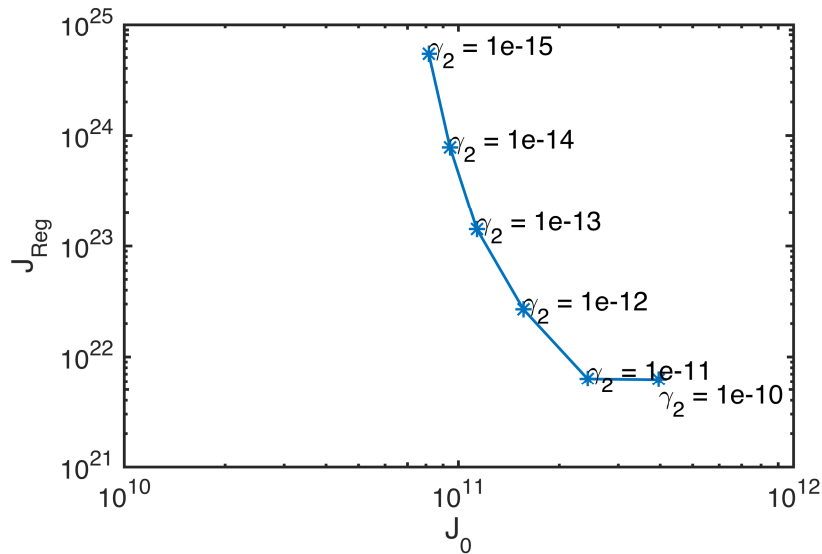


Fig. 4.13 Log-log plot for L-curve analysis of inversions of the Russell Glacier area employing a linear sliding law.

with a rapid decrease into a long tail. The maximum difference is approximately 165 myr^{-1} . The difference between modelled and observed velocities is less than 10 myr^{-1} for 88% of the cells in the study area, and less than 20 myr^{-1} for 96% of the cells in the study area. A map of the difference between observed and modelled velocities shows the highest difference occurs along the ice-margin and in the vicinity of the nunatak (Figure 4.15b). Figure 4.16 shows the inverted basal drag parameter, basal drag, and the sliding ratio for the linear sliding law.

Subglacial Hydrology Model

Basal melt during the winter is shown in Figure 4.17. Most values are between 0.015 and 0.03 myr^{-1} , with higher values predominately occurring near the nunatak. The spatial pattern of melt broadly reflects the patterns of surface velocities (Figure 4.2).

The subglacial hydrology model winter run evolves rapidly at the beginning of the run (Figure 4.18). By day 50 of the model run, the rate of change is significantly reduced. At day 240 of the run the model is in an approximate steady state. Relative to discharge at the base, changes in effective pressures have a much lower magnitude.

The distribution of sheet thickness at the end of winter mirrors basal topography, with the sheet thickest in topographic lows (Figure 4.19). The maximum sheet thickness is 0.36 m , which is less than the bed roughness scale of 0.5 m . The effective pressure also reflects the basal topography, with lowest effective pressures located in topographic lows. Since the

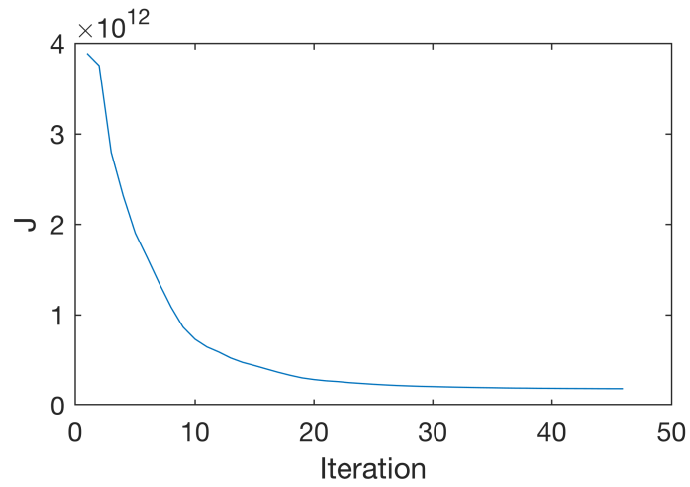


Fig. 4.14 Convergence of the optimization routine for the inversion using a linear sliding law.

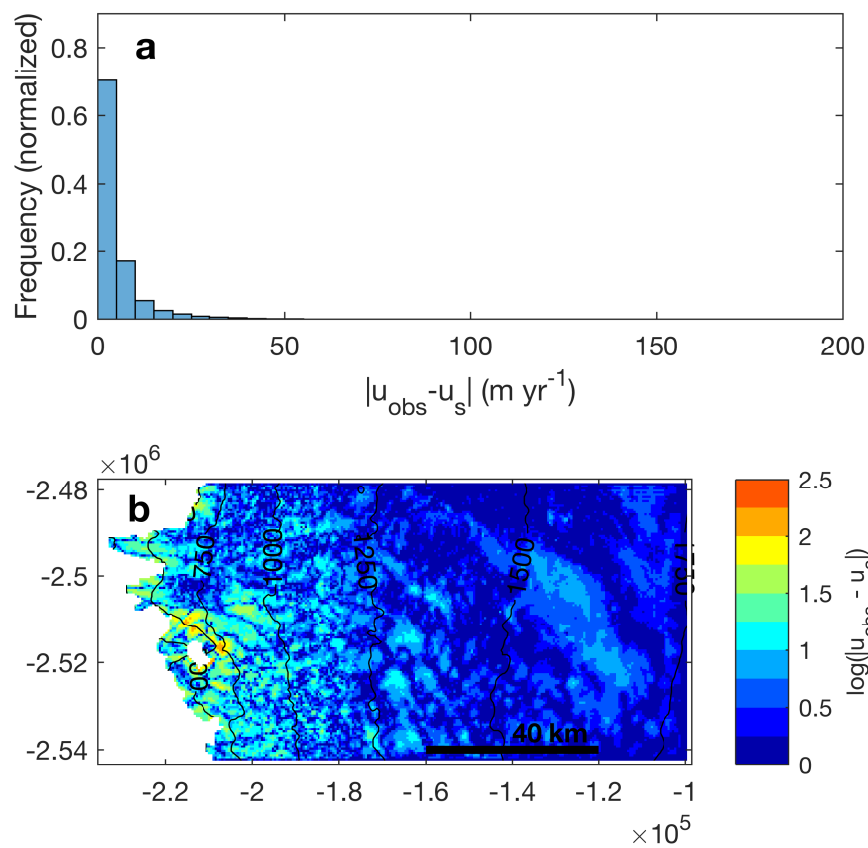


Fig. 4.15 a) Histogram of the absolute difference between the observed and modelled surface velocities for the inversion using a linear sliding law. b) Map of the log of the absolute difference between the observed and modelled surface velocities for the same inversion.

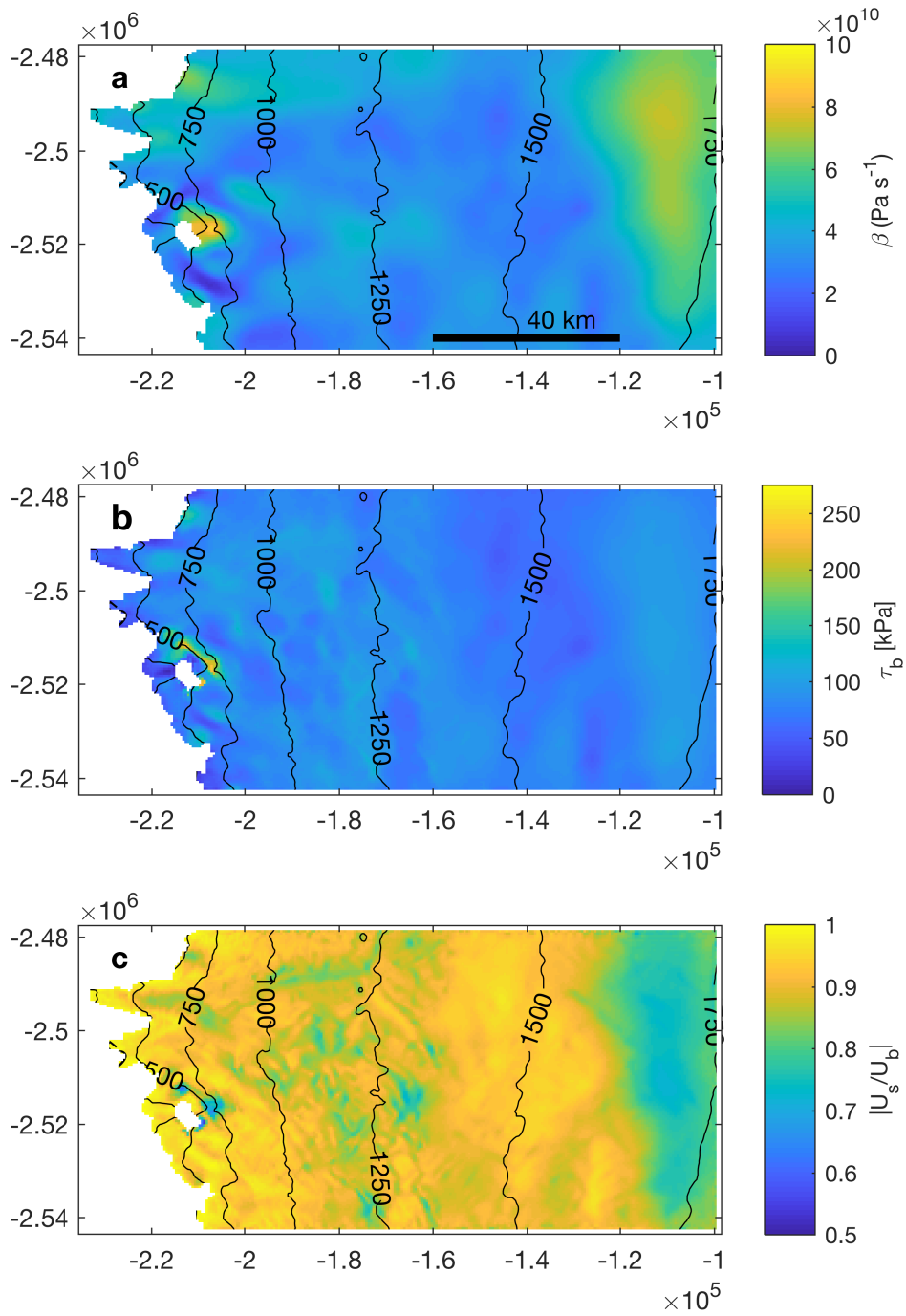


Fig. 4.16 Inversion results using the linear sliding law. a) Inverted drag parameter. b) Basal drag. c) Sliding ratio.

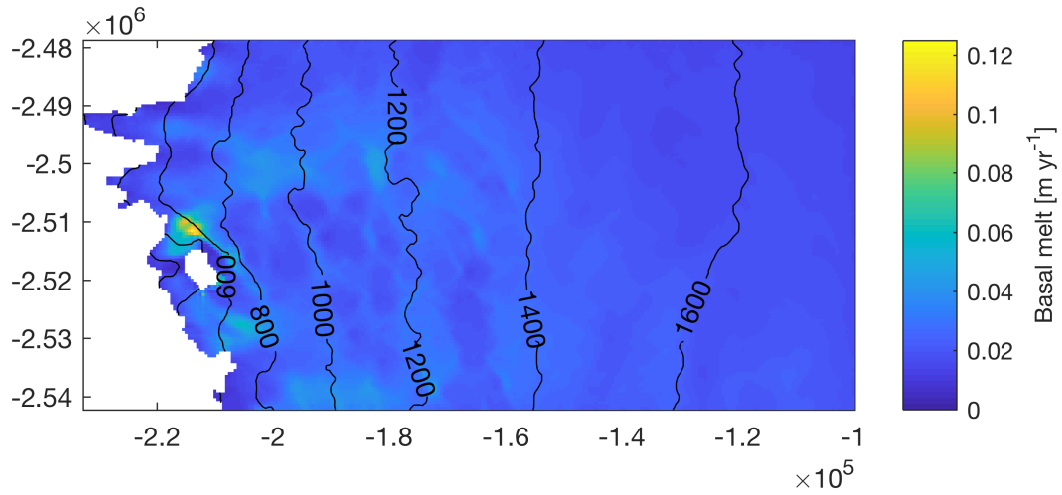


Fig. 4.17 Modelled basal melt rate using basal velocities from linear inversion.

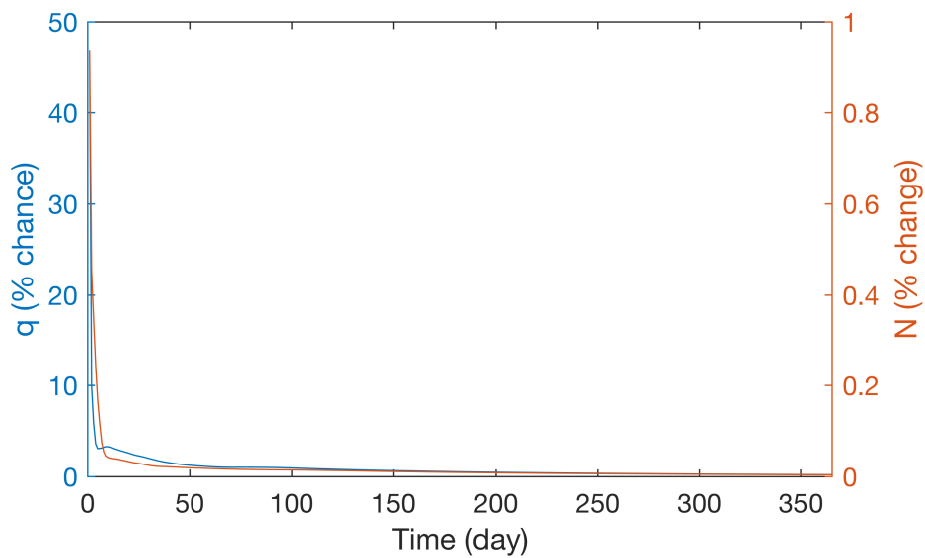


Fig. 4.18 Plot showing the mean daily % change in water flux and effective pressure for a one year run.

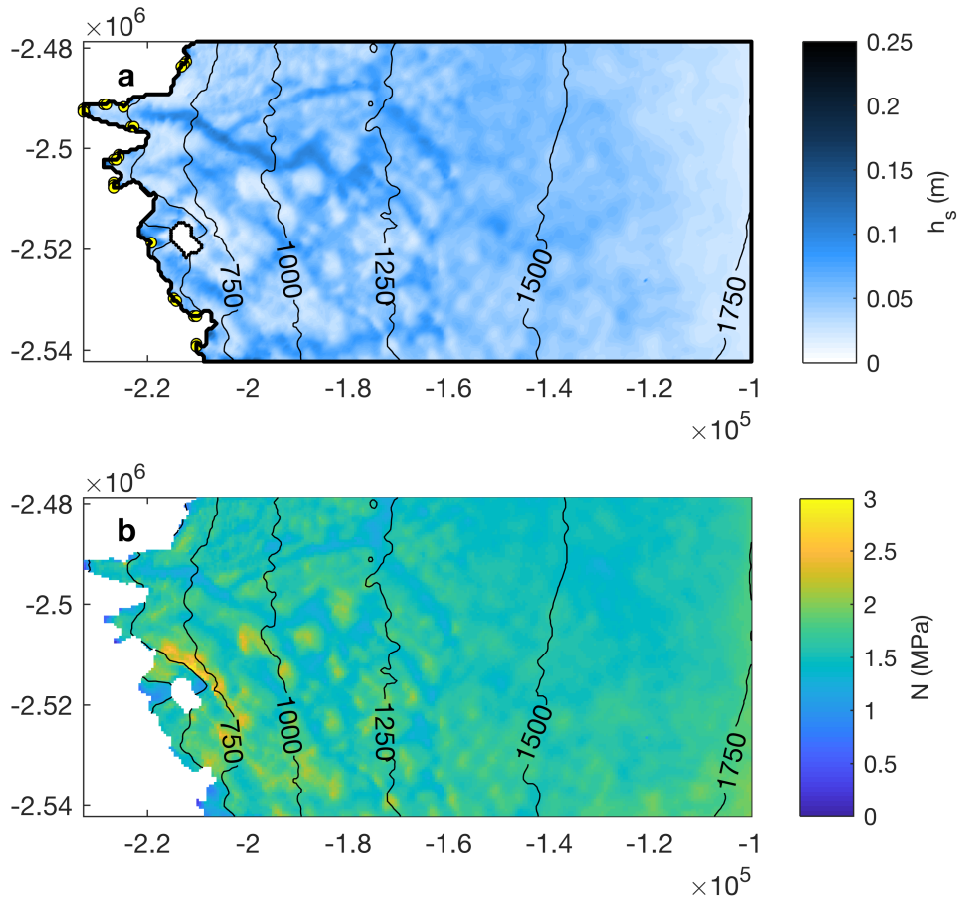


Fig. 4.19 Modelled state of the subglacial hydrology system at the end of the winter. a) Map of sheet thickness, with black contours showing surface elevation. b) Map of effective pressure overlaid with surface elevation contours.

lowest effective pressure is 0.44 MPa, no part of the ice sheet is near flotation. The model predicts minor channelization in two locations (not shown), with single channels extending from the margin several kilometres.

Non-linear sliding laws

An L-curve analysis (Figure 4.20 and 4.23) is used to determine the optimum inversion for each of the non-linear sliding laws. The inversions corresponding to $\gamma_2 = 1$ is selected for the Weertman sliding law, while the inversion corresponding to $\gamma_2 = 10^{11}$ is selected for the Schoof sliding law. These were selected so that the cost term of the inversions were similar to that of the linear sliding law. The two cost terms for the Weertman and Schoof sliding laws are $J_0 = 1.78 \cdot 10^{11}$ and $J_0 = 1.60 \cdot 10^{11}$ respectively.

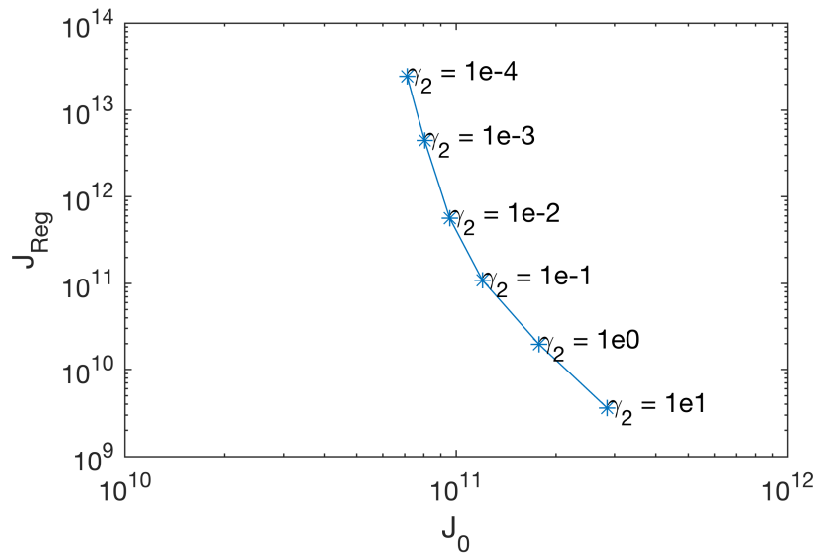


Fig. 4.20 Log-log plot for L-curve analysis of inversions of the Russell Glacier area employing generalized Weertman sliding law.

The histogram of the absolute difference between observed and modelled surface velocities for both non-linear sliding laws shows a similar distribution to the linear sliding law inversion (Figure 4.21 and 4.24). The Weertman sliding law results in a spatial distribution of misfit similar to the linear sliding law, while spatial distribution of error from the Schoof sliding law shows higher frequency variations. Model mismatch again is highest in the vicinity of the nunatak.

Figure (4.22 and 4.25) show the inversion results from the Weertman and Schoof sliding law respectively. Inverted basal drag using the Weertman sliding law is very similar to the results from the linear sliding law. In contrast, the inverted basal drag from the Schoof sliding law shows much higher frequency and magnitude spatial variations. This is reflected in the spatial distribution of the sliding ratio, with the Weertman sliding law resulting in a distribution similar to the linear sliding law, while the distribution from the Schoof sliding law shows much greater variation.

4.5 Discussion

4.5.1 Methods

The ice sheet model developed compares favourably with the ISMIP-HOM simulations, as well as to the results presented in Goldberg and Heimbach (2013) for another hybrid model implementation. Grid convergence shows that as the numerical grid becomes finer,

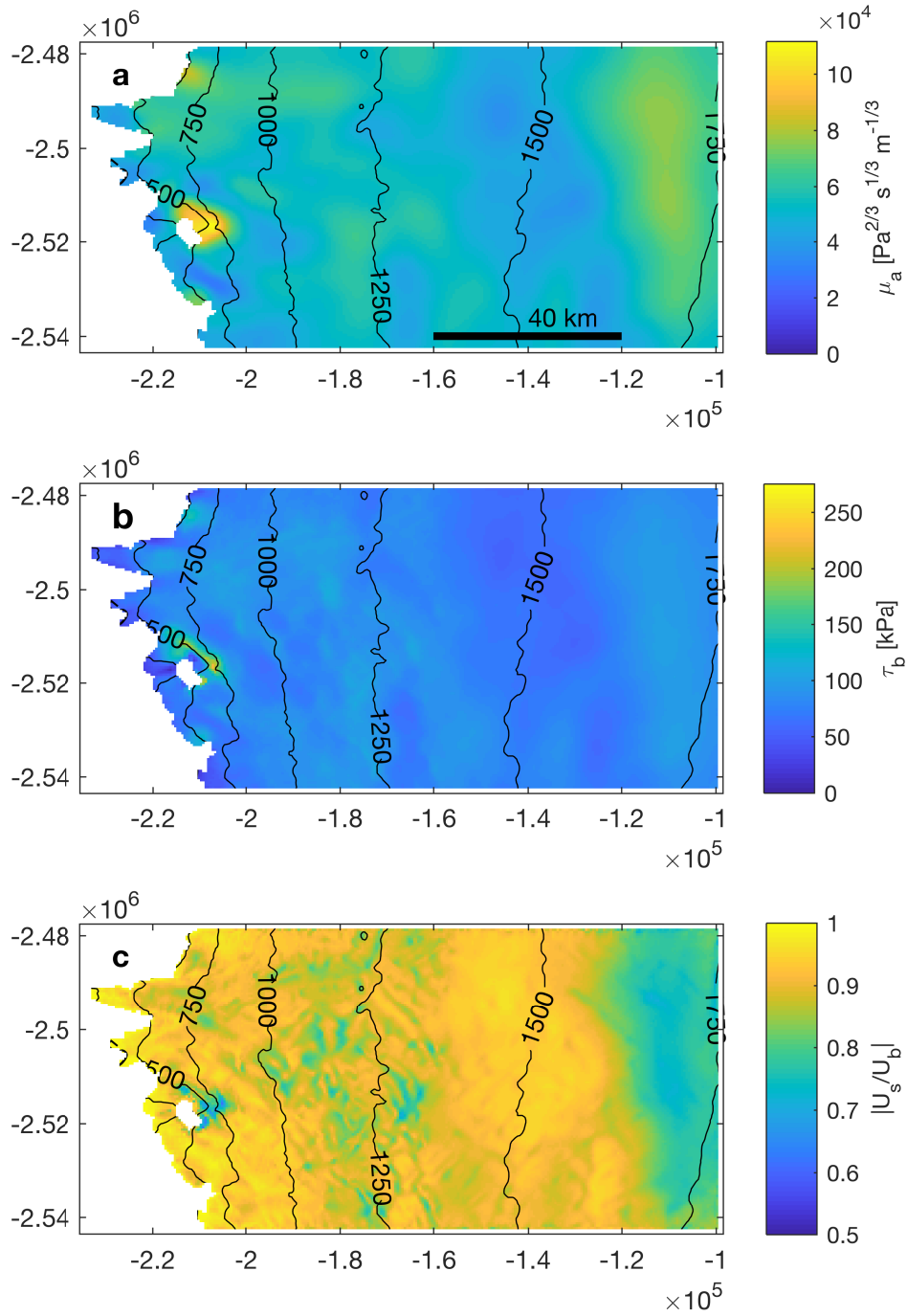


Fig. 4.22 Inversion results using the Weertman sliding law. a) Inverted drag parameter. b) Basal drag. c) Sliding ratio.

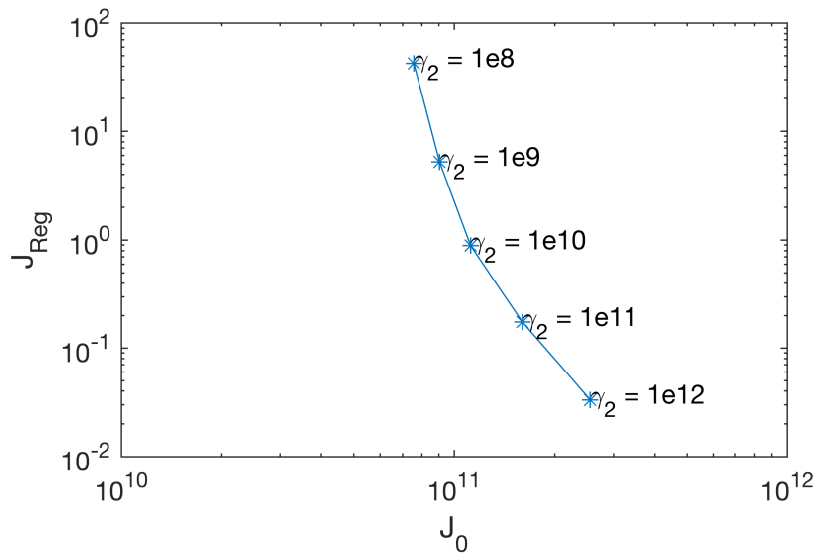


Fig. 4.23 Log-log plot for L-curve analysis of inversions of the Russell Glacier area employing the Schoof sliding law.

the solution approaches a fixed point. These tests show that the model solves the equations stated, and that the model performs robustly.

Multiple methods for calculating the viscosity were tested. When basal topography varies rapidly and there is no basal sliding as in ISMIP-HOM Experiment A at 20 km domain length, the procedure for calculating the viscosity determines whether the solution converges. Testing shows that using the two iteration fixed point iteration methods results in the fastest convergence of the velocity solution. Solving the cubic equation, or using a three fixed point iteration led to instability in the Picard iterative process. This has been observed by other authors implementing the hybrid model, and instabilities have been hypothesized to occur when the viscosity is calculated precisely while the velocity is still far from converged values (D. Goldberg, personal communication, Dec 7, 2016). However, if ISMIP-HOM experiment A was to be run at an even shorter domain length, it may be that the only method that converges is to simply use the previous iteration's viscosity.

Such issues may not be important in practice for every study, as basal topography variability can be effectively damped by low grid resolution, or by low resolution data products. For example, the hybrid model has been successfully applied using the cubic equations to solve for viscosity for all of Antarctica by Arthern et al. (2015). However, a test of the ice sheet model applied the Russell Glacier area at 500 m resolution calculating viscosity by solving the cubic equations revealed that two small areas did not converge.

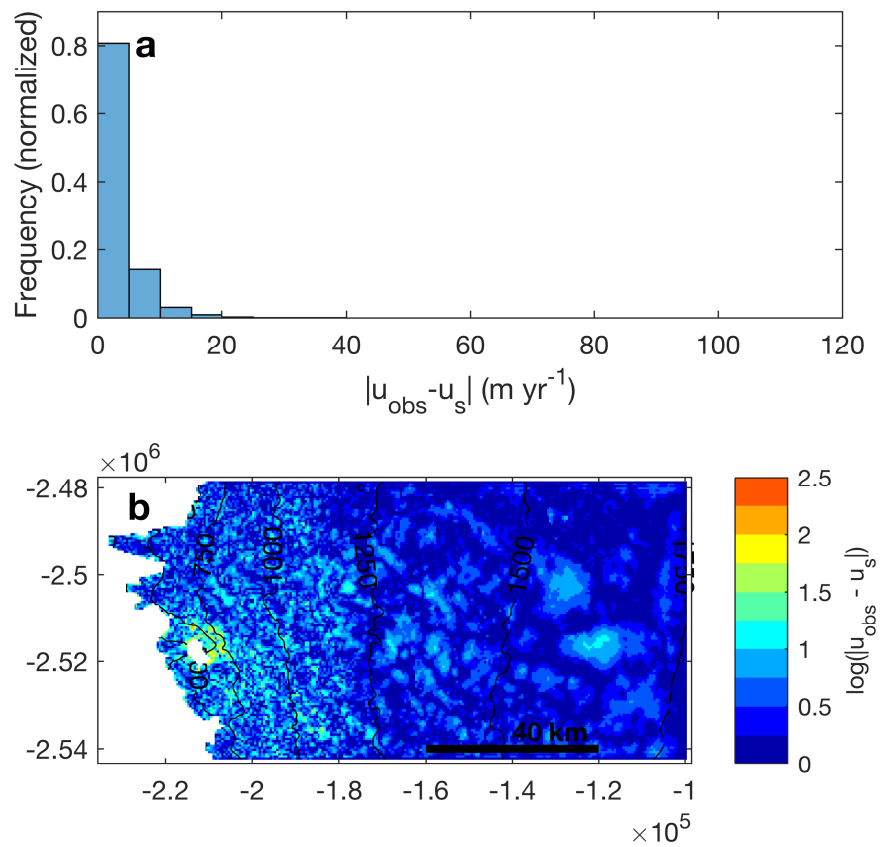


Fig. 4.24 a) Histogram of the absolute difference between the observed and modelled surface velocities for the inversion using a Schoof sliding law. b) Map of the log of the absolute difference between the observed and modelled surface velocities for the same inversion.

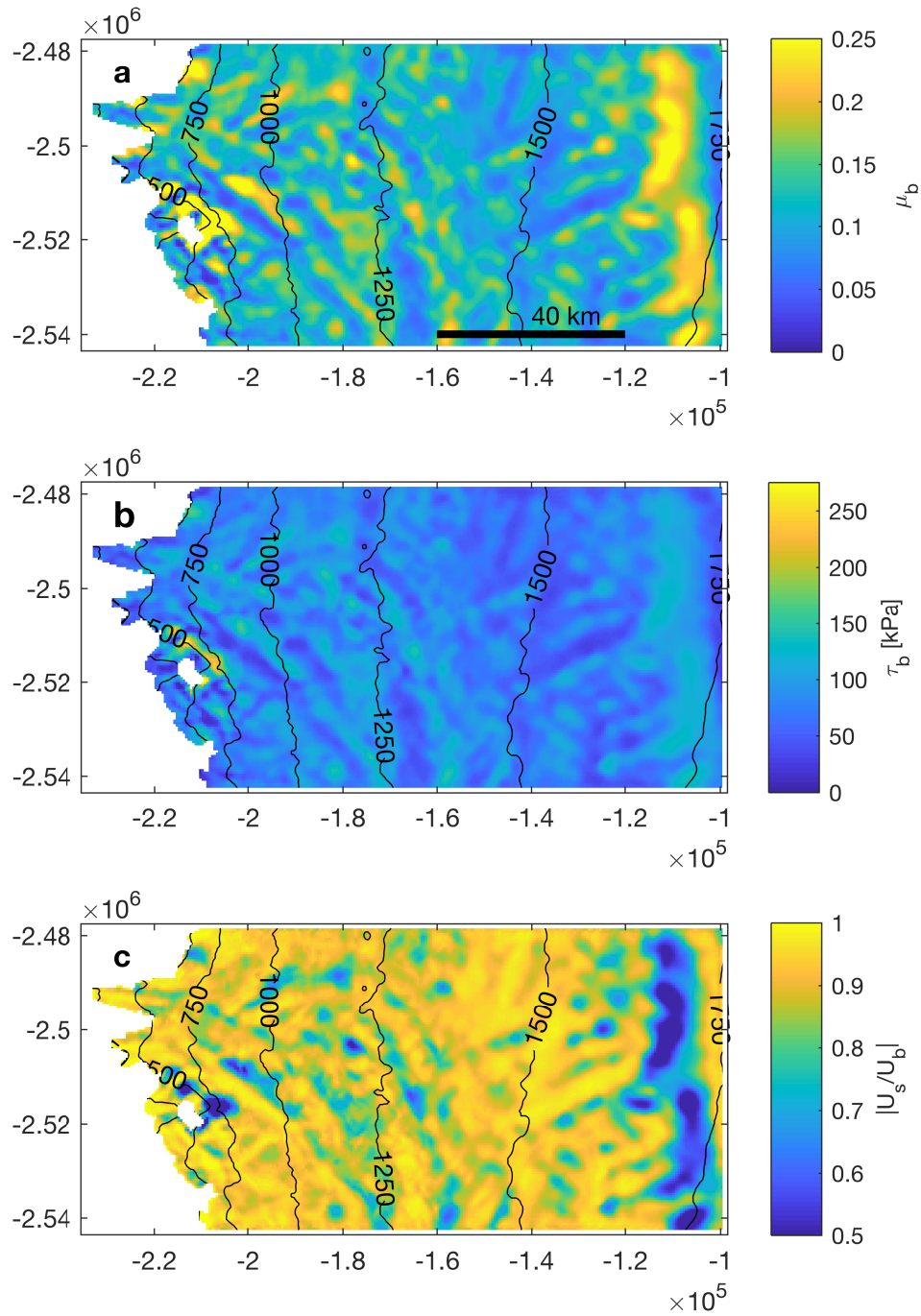


Fig. 4.25 Inversion results using the Schoof sliding law. a) Inverted drag parameter. b) Basal drag. c) Sliding ratio.

In the adjoint model, the viscosity is calculated using the cubic equation. This reduces the memory load of storing previous values, but is also necessary for ADiGator to process the forward code. When the adjoint model is called, both the velocity and viscosity are at converged values. Hence, this should not lead to the instabilities observed in the forward model.

The hybrid model approximates the BP equations. Performance in the fast sliding regime is known to be better than in the slow flow/frozen bed regime, and previous work has shown that the hybrid model performs poorly when ice flow is over variable topography or is slow/frozen at the bed (Goldberg, 2011). This is observable in the results of ISMIP-HOM experiments A and C at low domain lengths, where the model performance decreases as basal topography variability increases. Basal topography in the Russell Glacier area shows variations on the length scale 10 km, particularly at low and mid elevations. In this region, the hybrid model is expected to have poorer performance, and a higher order ice sheet model would be more appropriate. However, the use of the hybrid model has significant benefits in terms of computational resources, which are important for Chapter 5 in which ice sheet velocities are re-calculated on an hourly timescale for a summer melt season.

A series of twin tests was performed for each of the sliding laws using the ISMIP-HOM domain. In each test, the inversion procedure optimized the basal parameter to recreate the known surface velocity to satisfactory accuracy. Inversion performance was highest for the linear sliding law, and least for the Schoof sliding law. This reflects the accuracy of the gradient from the adjoint model, since as non-linearity increases, the accuracy of the gradient is observed to decrease.

The adjoint model implemented is equivalent to one reverse iteration from the final Picard Iteration, which is equivalent to the method of Lagrangian multipliers (Heimbach and Bugnion, 2009). This is shown in (Martin and Monnier, 2014) to be an approximation of the gradient. To determine the gradient to a higher accuracy, the adjoint model should step backwards through all the Picard iterations, or solve a related fixed point problem (Goldberg et al., 2016). Alternatively, a method such as that in Arthern et al. (2015) could be used.

Calculating the gradient is the computationally expensive task in the inversion process. A significant amount of resources are spent on the counterpart of S2 in the forward model pseudocode (Alg. 3). In the ISMIP-HOM simulations, with an 80x80 grid, this section of code takes approximately 17 s to run on a computer with an Intel Quad Core 3.40Ghz processor. However, this same code takes 550 s to run when applied to the Russell Glacier area (132x274 grid). Hence, at the limit of high grid resolution over the domain of interest in the Russell Glacier area, to step back through the full Picard iterative process, or solve the related fixed point problem, would be computationally prohibitive with the resources

available. An avenue to improve efficiency would be to translate the adjoint operation on the linear system of equations solver section of the code into Fortran or C, and interfacing it with Matlab using a Mex function.

4.5.2 Application

Inversions of the Russell Glacier area are run with a constant creep parameter A , corresponding to an ice temperature of approximately -7 °C (Cuffey and Paterson, 2010). For inversions with the linear sliding law, tests showed poorer results when A increased (corresponding to warmer ice). As A decreased, the sliding ratio approached one uniformly, and inversion results were better able to match observed surface velocities. The value of A was selected as a balance of model fit, while keeping a contribution to motion from internal deformation. Observations from two boreholes located in the Paakitsoq region show that internal deformation results in approximately 27-56% of ice velocities during winter (Ryser et al., 2014). In reality, A would have a heterogeneous distribution. By using a constant A , the basal drag parameter will account for some of the effects which would otherwise be due to variation in A .

Basal velocities determined from the optimal inversion using a linear sliding law are input into the subglacial hydrology model. The distribution of basal velocities is used to both calculate the basal melt rate, and the cavity space in the continuum sheet flow. Due to the selection of a creep parameter such that the sliding ratio is relatively high, it is likely that basal velocities are overestimated. This would result in an overestimate of water generated at the ice-bed interface, and an overestimate of the capacity of cavity space. Application of a higher order ice sheet model would be advantageous in these regards.

The pattern of basal drag inverted using the linear and Weertman sliding law show limited differences. This is due to the fact that basal shear traction must satisfy the global stress balance (Joughin et al., 2004; Minchew et al., 2016). Both the linear and Weertman sliding law have the form $\tau_b = C \cdot u^{1/m}$ in the inversion, since effective pressure can be incorporated into the constant C for the Weertman sliding law. Previous work shows that in this case $C \propto u^{-1/m}$, and the recovered fields of basal drag are within a few percent of each other (Minchew et al., 2016). The basal drag and basal velocities from the the linear sliding law to initiate the subglacial hydrology model are therefore self consistent with the subsequent inversion results of the Weertman sliding law. The pattern of basal drag inverted using the Schoof sliding law however, shows both higher spatial variability and a higher magnitude of variability. This is a result of the Schoof sliding law shifting to Coulumb-like behaviour at low effective pressures.

Interpretation of radar lines in the Russell Glacier area suggests significant winter storage of water along topographic highs, while significant water flow through topographic lows occurs during the summer melt seasons (Chu et al., 2016). Based on these observations, the subglacial hydrology run in this chapter is reflective of summer conditions rather than winter conditions. Water storage, which would be characterized by high sheet thickness, is not observed along topographic highs. Chu et al. (2016) attribute storage on topographic ridges to water storage in parts of the distributed system which become isolated at the end of the melt season. In contrast, porous sediments in bedrock troughs are hypothesized to allow water to drain (Chu et al., 2016). The treatment of the bed in the subglacial hydrology model is uniform. It does not account for differences in till cover or bed properties, nor does it account for sub-grid scale heterogeneity in the distributed system, which is likely the cause of water storage. Replicating these observations likely requires the implementation of another model component, such as the weakly connected distributed system proposed by Hoffman et al. (2016). In general, model output from the subglacial hydrology model can be expected to be much more sensitive to the model formulation during the winter than the summer, when the system is forced by high water input. In line with inferences from tracer injections (Chandler et al., 2013), the model does not predict a channelized system at the margin during the winter.

The initialization procedure introduced in this chapter is not capable of producing the inferred year on year differences in the subglacial hydrological system at the end of winter. Currently, the subglacial hydrology reaches an approximate steady state by day 240, and is not particularly sensitive to the initialization of the distributed sheet thickness. A full steady state takes approximately two years (Hewitt, 2013). In contrast, observations suggest that summer melt has an impact on the state of the hydrological system during the subsequent winter (Chu et al., 2016; Sole et al., 2013). The model output of the model therefore can only be considered an approximation to a generic hydrological state. Any discrepancy between the modelled and actual hydrological system is expected to have a greater impact on inversions using the Schoof sliding law, since it has a stronger dependence on effective pressure. In the limit of viscous flow, the Schoof sliding law depends on N . In contrast, the generalized Weertman law applied in this chapter is a function of $N^{1/3}$ (Budd et al., 1979). All inversions are conducted using mean winter velocities from 2008-2009. Annual differences in mean winter velocities are expected to have a minimal impact, as observed year on year differences are on the order 20 myr^{-1} , which is not significantly greater than the velocity mismatch in the inversions.

Other procedures for determining the background parameters of sliding laws can likely be devised. Currently the procedure only uses mean winter velocities. Using mean annual

velocities may improve estimates of the sliding law parameters by incorporating information from the melt season. A subglacial hydrological model could be run for an entire year, and basal parameters determined from an annual average water pressure. A key difficulty is running the hydrological model during the summer, as the development of the system is known to depend on feedbacks with velocity (Hoffman and Price, 2014). This issue can be avoided by using velocity measurements from remote-sensing as a model forcing (e.g Fahnestock et al., 2016). An advantage of running the subglacial hydrology model during the summer months is that model output may be more representative of water flow beneath the ice sheet. Although in its current form the model is too complex, a simplified subglacial hydrology model may be suitable to time dependent adjoint modelling (Goldberg and Heimbach, 2013). Throughout this chapter, it is assumed the parameters of the sliding law are time independent. This assumption is better suited for bedrock than till, as properties of till are dependent on saturation and deformational history (Minchew et al., 2016).

4.6 Conclusions

The ice sheet and inversion code developed in this chapter are shown to be robust. The hybrid model shows grid convergence, and compares favourably to previously published results. Testing suggests that using a fixed point iteration with two iterations to calculate the viscosity maintains the stability of the Picard Iterative process while providing the fastest rate of convergence.

A procedure for initializing a subglacial hydrology model for a winter run is proposed. However, the modelled state of the subglacial hydrological system at the end of winter appears to reflect summer observations rather than winter observations. This is likely the result of model formulation rather than the initialization procedure, and the initialization procedure should prove useful as model development advances. The results are subsequently used to run inversions using non-linear sliding laws which are functions of effective pressure. This allows the background parameters for the sliding law to be determined. To date, this appears to be the first work to incorporate modelled water pressures in an inversion, and the first to invert with a sliding law explicitly dependent on effective pressure. The usefulness of this inversion for initiating coupled ice sheet/ hydrology model simulations is shown in the next chapter.

Chapter 5

Integrated Modelling

5.1 Overview

In this chapter, the ice flow model developed in the previous chapter is coupled with a current subglacial hydrology model (Banwell et al., 2016; Hewitt, 2013). This combined model is then run for three contrasting melt seasons in the Russell Glacier area to investigate the impact of melt season intensity on the coupled system. The model is initialized using the inversions for basal conditions from the previous chapter performed at a coarser resolution, and driven using surface runoff input from the supraglacial model developed in Chapter 3. Model parameters are calibrated using GPS measurements from 2009 and 2011, and ice velocities are validated against the GPS measurements from 2012 (Tedstone and Neino, 2017).

This chapter begins with an introduction to the link between melt and ice velocities in the GrIS. Following the introduction, the methods section describes the study site, each of the models used, as well as their coupling and the workflow followed. The results include the partitioning of melt between different pathways, and comparison of ice flow to GPS records. The discussion focuses on the quality of model fit, model complexity, and potential future evolution of the subglacial hydrological system. The key conclusion is to support the hypothesis that similarly to the seasonal speedup of alpine glaciers, the summer acceleration of the GrIS margin is controlled by the evolution of the subglacial hydrological system.

5.2 Introduction

Seasonal acceleration at the GrIS margin is driven by surface meltwater draining into the subglacial system. Increased water pressures reduce basal drag by decreasing ice-bed cou-

pling, leading to faster ice flow. Early in the summer, surface runoff drains into an inefficient hydrological system, elevating water pressures and accelerating ice flow (Bartholomew et al., 2011b; Fitzpatrick et al., 2013; Sundal et al., 2011). As the melt season progresses, a channelized system that efficiently drains water develops. This reduces water pressures and leads to a late summer deceleration (Bartholomew et al., 2010; Chandler et al., 2013; Cowton et al., 2013; Schoof, 2010). Understanding the impact of increased surface melting (Hanna et al., 2013; van den Broeke et al., 2009) on the spatial and temporal evolution of basal hydrology is important for constraining the GrIS's future evolution. If increased summer melt intensity drives faster mean annual velocities, than a positive feedback between surface melt and ice flow would contribute to mass loss from the GrIS in a warming climate (Zwally et al., 2002). Faster ice flow would draw ice down to lower elevations, where the melting is greater, which in turn drives faster ice flow.

Observations do not show a simple relationship between surface runoff and ice velocities however. Decadal-timescale observations in Southwest Greenland of land terminating sectors show mean annual velocities decreasing in the ablation zone (Stevens et al., 2016; Tedstone et al., 2015; van de Wal et al., 2015). However reported correlation between summer melt intensity and mean annual ice velocities from these studies are either slightly negative, or nonexistent. In the accumulation zone, measurements are sparse and the data inconclusive about velocity trends (Doyle et al., 2014; van de Wal et al., 2015). Measurements on a daily timescale show increased melt intensity can lead to faster ice flow early in the summer. However, increased ice motion early in the summer can be offset by an earlier onset of channelization and corresponding deceleration (Sundal et al., 2011; van de Wal et al., 2015). Increases in channelization extent may also lead to slower mean winter flow, due to more extensive drainage of the subglacial system leading to lower water pressures during winter (Sole et al., 2013). As melt season intensity continues to increase, it remains unclear how ice velocities may be altered due to changing patterns of input, and input at higher elevations where ice thickness is greater.

Numerical models can provide insight into the hydrological processes driving faster summer flow. Recent subglacial hydrology models have progressed to simultaneously incorporating both distributed and efficient systems, explicitly treating the interaction between the two (de Fleurian et al., 2016; Hewitt, 2013; Hoffman and Price, 2014; Pimentel and Flowers, 2010; Schoof, 2010; Werder et al., 2013). Current models can reproduce the observed upglacier development of the efficient system through the melt season. When coupled to an ice sheet model, the results broadly reproduce the observed velocity patterns of the GrIS margin (Hewitt, 2013; Pimentel and Flowers, 2010). However, recent hydrological models coupled to an ice flow models have not been applied to real domains of the GrIS

to model large-scale behaviour of the ice-margin during the summer melt season . Rather, applications to real domains for the summer melt season have either omitted ice flow (Banwell et al., 2016; de Fleurian et al., 2016), used a simplified hydrological model coupled to ice flow (Bougamont et al., 2014; Colgan et al., 2012), or focused on a small domain (Hoffman et al., 2016). Coupling recent hydrological models with ice sheet models allows for an important feedback between the distributed system and ice velocities (Bartholomaeus et al., 2011; Hoffman and Price, 2014), and allows explicit comparison between GPS velocities and model output. Comparisons to velocity measurements are an important means for validating subglacial hydrological models, and provide a method for constraining poorly understood aspects of subglacial hydrology (see review by Flowers, 2015). Present challenges in applying coupled models to the GrIS margin for modelling seasonal evolution include: the values of parameters; the form of the sliding law which relates water pressures to basal drag; and whether the models presently include the necessary elements. Additionally, modelling surface hydrological input to the drive the hydrology model is in itself a challenge. A variety of different methods have been employed, incorporating different drainage elements (e.g. Banwell et al., 2016; Bougamont et al., 2014; de Fleurian et al., 2016). However, no model to date has included the full spectrum of supraglacial drainage pathways.

This chapter aims to model summer ice flow in the Russell Glacier area for three contrasting melt seasons using a multicomponent model approach similar to the previous work of Arnold et al. (1998) and Flowers and Clarke (2002) on alpine glaciers. The model is then used to test the response to higher melt input. A coupled hydrology-ice flow model is produced by integrating a subglacial hydrology model (Hewitt, 2013) with the ice flow model of Chapter 4. This model is driven by surface input from the surface hydrology model from Chapter 3, and initiated using the inversions from Chapter 4. The Russell Glacier area is selected as a study site to take advantage of the numerous observations available. These observations include radar flight lines constraining topography (Morlighem et al., 2015b), meteorological data constraining climatic input (Noël et al., 2015), and GPS data (Tedstone and Neinow, 2017) which provide a calibration and validation data set for model output.

5.3 Methods

The methods section begins with a description of the Russell Glacier study area and the data sets used. The study site is presented first so that the domain can be referred to when describing the boundary conditions applied in the models. Each individual model is then briefly described, before detailing how the models are linked. The coupled ice flow/subglacial

hydrology model is referred to as the 'integrated model' for simplicity. Finally, the modelling workflow is described.

5.3.1 Study Area and Datasets

The Russell Glacier area is a land-terminating sector of the GrIS in Southwest Greenland. The study area boundaries for the SRLF model and the integrated model are shown in Figure 5.1. The integrated model study domain is the same as used for the inversions described in Ch 4. The domain of the SRLF runs is selected to be larger than the integrated model domain to minimize the impact of boundary conditions. A 6 km buffer is used at the northern and southern boundaries of the SRLF domain, based on the reported internally drained catchments by Yang and Smith (2016). The SRLF domain extends 8.5 km to east of the integrated model study site to capture as much higher elevation melting as possible. The domain of the SRLF model is discretized at a 90 m resolution, while the domain of the integrated model is discretized at a 1000 m resolution.

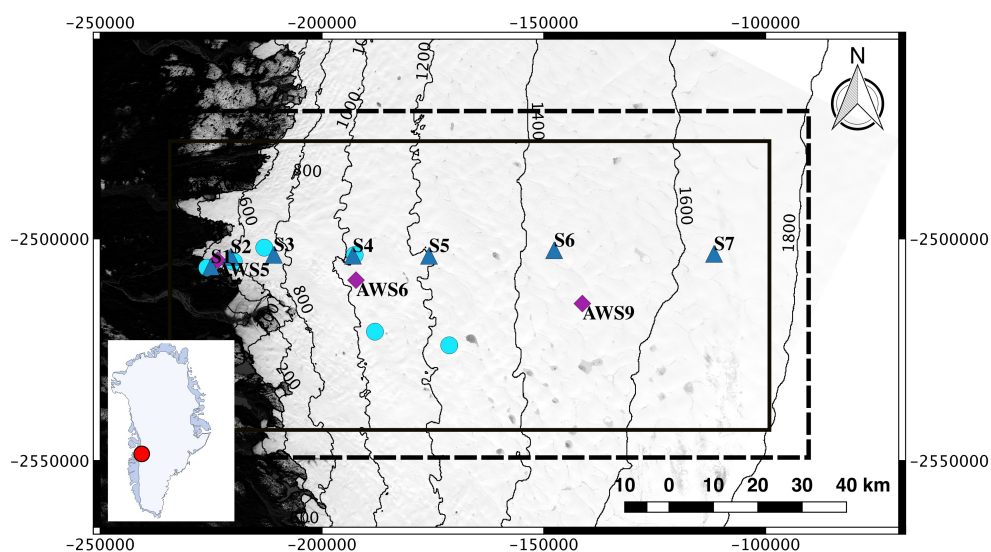


Fig. 5.1 Landsat 8 satellite image, band 2, showing the Russell Glacier area. Black solid rectangle outlines the study domain for the integrated model, while the black dashed rectangle outlines the SRLF study domain. The blue triangles show the locations of GPS stations (Tedstone and Neino, 2017). Purple diamonds show the locations of automatic weather stations (van de Wal et al., 2015). Cyan circles show the locations of moulin injection sites in Chandler et al. (2013). Inset shows the location in reference to Greenland.

Two different topography datasets are used. The SRLF model is run with the 90 m resolution surface and bed topography from the GIMP dataset (Howat et al., 2015). The high resolution surface topography is necessary for accurate water routing and so that lake

basin topography is accurately preserved. The integrated model is run with surface and bed topography from BedMachine2 (Morlighem et al., 2014, 2015b) to take advantage of the mass-conservation methods used to determine basal topography. BedMachine2 provides both topographic datasets at 150 m, although the true resolution is reported as 400 m. This data is reinterpolated to 1000 m resolution.

Surface runoff and snow depth data for the SRLF model are provided by RACMO2.3 (Noël et al., 2015). Both runoff and snow depth are bilinearly interpolated from 11 km to 90 m, as in Chapter 3. Three seasons with contrasting melt volumes are modelled: 2009, 2011, and 2012 (Figure 5.2). Total melt over the SRLF study domain was $1.2 \cdot 10^{10} \text{ m}^3$ in 2009, $1.7 \cdot 10^{10} \text{ m}^3$ in 2011, and $2.1 \cdot 10^{10} \text{ m}^3$ in 2012. These three years serve as analogues for summers with average, elevated, and extreme melt intensity respectively, again following Ch 3.

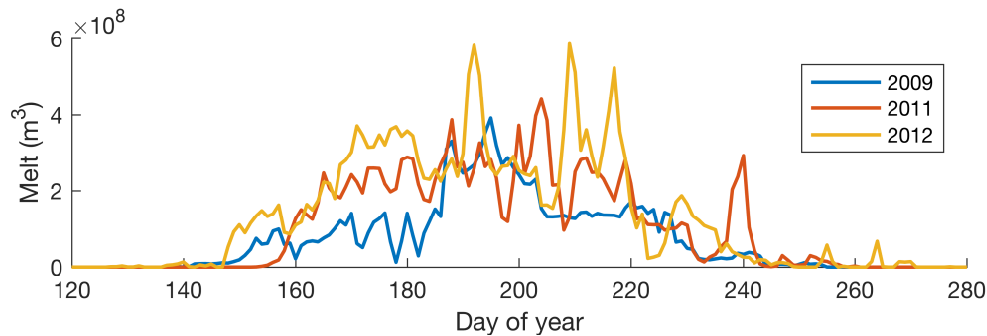


Fig. 5.2 Daily surface runoff over the SRLF Russell Glacier study area for three contrasting summer melt seasons.

Mean winter velocities are used for inversions of winter basal boundary conditions and to determine crevasse locations as an input to the SRLF model. Mean winter velocities for 2008-2009 are provided at 500 m resolution by the MEaSURES Greenland Ice Sheet Velocity Map dataset (Joughin et al., 2010a,b). For the inversion procedure, the winter velocities, along with their associated errors, are reinterpolated to 1000 m. Velocities at 500 m resolution are used to determine surface stresses, assuming an ice temperature of -5° C . Crevassed areas are then calculated using a von Mises stress criterion following Clason et al. (2015), and as in Chapter 3. A crevassing threshold is selected by comparing the von Mises stress to observed patterns of crevassing in a Landsat 8 image. A threshold value of 145 kPa is selected as optimal.

Moulin locations are inputs to the SRLF model. Moulin locations in the Russell Glacier area reported by Yang et al. (2015) are used. These are derived automatically from a Landsat 8 image acquired on 19 August 2013, using an algorithm which determines where streams are observed to abruptly disappear (Yang et al., 2015). As in Ch 3, moulin locations which

do not coincide with a calculated stream location are slightly adjusted, such that they are located on a stream. A small number of moulins from the dataset are deleted, as they were not near a calculated stream, and hence would drain negligible water.

A key dataset in the Russell Glacier area is GPS surface velocity measurements for 2009-2012 (Tedstone and Neinow, 2017). A time series of hourly and daily averaged surface speeds are provided in the dataset. In this chapter, the daily averaged speeds are used to calibrate and validate the modelling. The locations of GPS stations are shown in in Figure 5.1.

5.3.2 Supraglacial Hydrology

This chapter utilizes the supraglacial hydrology model (SRLF) developed in Chapter 3, and is run with the best fit parameters at 90 m resolution. A no-inflow boundary condition is imposed on all boundaries, and water is allowed to drain off the domain or over the western ice margin. Water is routed using a DEM of the surface of the ice sheet and a single flow direction algorithm (Tarboron, 1997). Water collects in depressions forming lakes. Lakes which are predicted to hydrofracture, using a fracture area criterion, drain to the ice-bed interface and create a surface to bed connection for the remainder of the melt season. Lakes can also drain over the surface of the ice sheet via overspill drainage and channelized drainage. Overspill drainage refers to when water exceeding the capacity of the lake is routed downstream, with no incision of a channel at the lake edge. Channelized drainage refers to when water is routed downstream, but incises a channel at the lake edge. Channel incision is modelled following Raymond and Nolan (2000). Overspill and channelized drainage can occur simultaneously if water enters a lake faster than can be evacuated by an existing channel alone. Water flowing over the ice can also drain into crevasses and moulins.

5.3.3 Subglacial Hydrology

The subglacial hydrology model presented in Hewitt (2013) and Banwell et al. (2016), which simulates both distributed and channelized systems, is used in this chapter. Distributed flow occurs through a continuum 'sheet', composed of a cavity sheet component and an elastic sheet component. The latter is included so that during lake hydrofracture events 'hydraulic jacking' is simulated. Channels can form along the edges and diagonals of the rectangular finite difference mesh. Dissipative heating over an incipient channel width length scale provides the initial perturbation for channel initialization. Water input occurs at moulins located at cell nodes, which along with an englacial aquifer, allow for water storage. The model is run at 1000 m resolution. At the ice-margin edge an atmospheric pressure boundary

condition is imposed, while the remaining boundaries have a no-flux condition. A concise model description is given here following Banwell et al. (2016); Hewitt (2013) to provide context for the parameters used. However, for a detailed description the reader is referred to Banwell et al. (2016); Hewitt (2013).

Discharge in the continuum sheet is modelled as:

$$\mathbf{q} = -\frac{Kh^3}{\rho_w g} \nabla \phi \quad (5.1)$$

where $h(x, y)$ is the thickness of the continuum sheet, K_s is the sheet hydraulic conductivity, g is the acceleration due to gravity, and ϕ is the hydraulic potential. The hydraulic potential is defined as $\phi(x, y) = \rho_w g b(x, y) + p_w(x, y)$.

The distributed sheet thickness (h) is the sum of the thickness of the cavity sheet (h_c) and the elastic sheet (h_{el}). The cavity sheet evolves according to:

$$\frac{\partial h_{cav}}{\partial t} = \frac{\rho_w}{\rho_i} m + U_b \frac{h_r - h_{cav}}{l_r} - \frac{2A_b}{n^n} h_{cav} |N|^{n-1} N \quad (5.2)$$

where ρ_i is the density of ice, m is the basal melting rate, U_b is the basal sliding speed, h_r is the bed roughness height scale, l_r is the bed roughness length scale, A_b is the ice creep parameter, n is the exponent from Glen's flow law, and $N(x, y)$ is the effective pressure. The effective pressure is defined as $N = \rho_i g H - p_w$, where H is the ice thickness, p_w is water pressure.

Basal melt rate is given by:

$$m = \frac{G + \boldsymbol{\tau}_b \cdot \mathbf{u}_b}{\rho_w L} \quad (5.3)$$

where $\boldsymbol{\tau}_b = (\tau_{bx}(x, y), \tau_{by}(x, y))$ is the basal drag, $\mathbf{u}_b = (u_b, v_b) = (u(x, y, b), v(x, y, b))$ is the basal velocity, G is the net conductive flux, defined as the geothermal heat flux minus conductive loss into the ice, and L is latent heat.

The elastic sheet thickness is given by:

$$h_{el} = C_{el} \left[-N_- + \frac{1}{2} N_0 \max(0, 1 - \frac{N_+}{N_0})^2 \right] \quad (5.4)$$

where $N_- = \min(N, 0)$, $N_+ = \max(N, 0)$, C_{el} is an elastic compliance, and N_0 is a regularization parameter. When effective pressure is positive, this layer is designed to be zero. As effective pressure approaches zero or is negative, the thickness is determined by the product of the elastic compliance and effective pressure (Banwell et al., 2016).

Discharge in channels is modelled as:

$$Q = -K_c S^{5/4} \left| \frac{\partial \phi}{\partial r} \right|^{-1/2} \frac{\partial \phi}{\partial r} \quad (5.5)$$

where K_c is a turbulent flow coefficient, S is channel cross-section, and r is along channel distance.

The channel cross section evolves according to:

$$\frac{\partial S}{\partial t} = \frac{\rho_w}{\rho_i} M - \frac{2A_b}{n^n} S |N|^{n-1} N \quad (5.6)$$

where M is the melting rate along the channel wall.

The melting rate along the channel walls is given by:

$$M = \frac{|Q \frac{\partial \phi}{\partial r}| + \lambda_c |q \cdot \nabla \phi|}{\rho_w L} \quad (5.7)$$

where λ_c is an incipient channel width.

The equation for mass conservation is:

$$\frac{\partial h}{\partial t} + \nabla \cdot \mathbf{q} + \left[\frac{\partial S}{\partial t} + \frac{\partial Q}{\partial r} \right] \delta(\mathbf{x}_c) + \frac{\partial \Sigma}{\partial t} = m + M \delta(\mathbf{x}_c) + R \delta(\mathbf{x}_m) \quad (5.8)$$

where Σ is englacial storage and R is the supraglacial input to moulins, The delta functions apply along channels ($\delta(\mathbf{x}_c)$) and the positions of moulins ($\delta(\mathbf{x}_m)$).

Englacial storage is represented as

$$\Sigma = \sigma \frac{P_w}{\rho_w g} + A_m \frac{P_w}{\rho_w g} \delta(\mathbf{x}_m) \quad (5.9)$$

where σ is englacial void fraction and A_m is moulin cross sectional area.

Model parameters held constant are shown in Table 5.1. Two parameters are assigned a spatially heterogeneous distribution in the calibration. The englacial storage parameter is assigned a background value of 10^{-3} , with 50% of the cells then randomly set to 10^{-4} . The effective sheet conductivity field is constructed using a background value of 10^{-2} , with 15% of the cell nodes randomly assigned a value of 10^{-7} . Since sheet conductivity is defined on the grid, neighboring nodes are averaged in the x and y directions to determine values on edges. At a sheet depth of 0.1 m, a sheet hydraulic conductivity of 10^{-2} results in an effective hydraulic conductivity kh^2 of 10^{-4} (Hewitt, 2013). This is at the upper end of values for till, which are inferred to be 10^{-4} to 10^{-9} (Fountain and Walder, 1998). The secondary value

Symbol	Constant	Value	Units
ρ_w	water density	1000	kg m^{-3}
ρ_i	ice density	910	kg m^{-3}
g	gravitational constant	9.8	m s^{-2}
n	exponent in glen's flow law	3	
A_b	creep parameter	$7 \cdot 10^{-24}$	$\text{Pa}^n \text{s}^{-1}$
L	latent heat	$3.35 \cdot 10^5$	J kg^{-3}
S_m	moulin area	10	m^2
σ	englacial void fraction	see text	
K_s	sheet flux coefficient	see text	$\text{Pa}^{-1} \text{s}^{-1}$
K_c	turbulent flow coefficient	0.1	$\text{m s}^{-1} \text{Pa}^{-1/2}$
λ_c	incipient channel width	10	m
K	hydraulic conductivity	2	$\text{m}^{-1} \text{s}^{-1}$
h_r	bed roughness height	0.1	m
l_r	bed roughness length	10	m
h_c	critical layer depth	1	m
C_{el}	elastic compliance	$1.02 \cdot 10^{-5}$	m Pa^{-1}
A_m	moulin cross sectional area	10	m^2

Table 5.1 Constants used in the subglacial hydrology model during integrated runs in the Russell Glacier area.

of 10^{-7} for sheet conductivity assigned at nodes was selected to give an effective hydraulic conductivity at the opposite end of the spectrum.

5.3.4 Ice Flow/Inversion

The ice flow model developed in Chapter 4 is used in this chapter. The ice flow model implements the hybrid formulation of the ice sheet stress balance (Arthern et al., 2015; Goldberg, 2011), which can be considered a combination of shallow ice approximation and shallow shelf approximation. The model implicitly accounts for depth varying ice flow, and surface velocities can be explicitly calculated when comparing model output to GPS measurements. This model is similar to the one used in (Hewitt, 2013), except the conservation of momentum equations are a function of depth integrated velocities rather than basal velocities. Parameters for the model are listed in Table 5.2. A Dirichlet boundary condition is imposed on all lateral domain margins except the ice-margin, where the standard boundary condition based on the continuity of stress is used. A no penetration boundary condition is applied at the edge of the nunatak (Figure 5.1). Three sliding laws are implemented:

$$\tau_b = \beta^2 u_b \quad (5.10)$$

Symbol	Constant	Value	Units
A	Ice-flow parameter	$7 \cdot 10^{-25}$	$\text{Pa}^n \text{s}^{-1}$
A_b	Ice-flow parameter for basal ice	$7 \cdot 10^{-24}$	$\text{Pa}^n \text{s}^{-1}$
ρ_i	Ice density	917	kg m^{-3}
g	Gravitational constant	9.81	m s^{-2}
n	Exponent in Glen's flow law	3	
p	Exponent generalized Weertman sliding law	3^{-1}	
q	Exponent generalized Weertman sliding law	3^{-1}	
λ_b	bed roughness scale	1	m
t_y	Seconds per year	31536000	yr^{-1}
ε	viscosity regularization parameter	$1 \cdot 10^{-14}$	m s^{-1}

Table 5.2 Constants used in the ice sheet/inversion model applied to the Russell Glacier Area.

$$\boldsymbol{\tau}_b = \mu_a N_+^p U_b^q \frac{\boldsymbol{u}_b}{U_b} \quad (5.11)$$

$$\boldsymbol{\tau}_b = \mu_b N_+ \left(\frac{U_b}{U_b + \lambda_b A_b N_+^m} \right)^{\frac{1}{n}} \frac{\boldsymbol{u}_b}{U_b} \quad (5.12)$$

where $\beta(x, y)$ is a basal drag coefficient, $\mu_a(x, y)$ is a drag coefficient, p and q are positive exponents, $\mu_b(x, y)$ is a limiting roughness slope, λ_b is a bed roughness length (Hewitt, 2013). Following Hewitt (2013), negative effective pressures are eliminated by setting $N_+ = \max(N, 0)$, and regularized with a small regularization constant.

The linear sliding law (Eq. 5.10) is used for the initial inversion of winter mean velocities, while the Weertman (Eq. 5.11) (Budd et al., 1979; Hewitt, 2013) and Schoof (Eq. 5.12) (Gagliardini et al., 2007; Schoof, 2005) sliding laws are used subsequently. The linear sliding law uses a single parameter to represent all the processes at the ice-bed interface, while the non-linear sliding laws attempt to explicitly incorporate the impact of effective pressure and have a more complex dependence on velocity.

The inversion code used in this chapter is described in Chapter 4. It is based on automatic differentiation methods (Goldberg and Heimbach, 2013; Heimbach and Bugnion, 2009; Martin and Monnier, 2014), and uses the open source Matlab package AdiGator (Weinstein and Rao, 2016). The gradient of the cost function in this method is equivalent to one calculated using Lagrangian multiplier methods (MacAyeal, 1993; Morlighem et al., 2013) to generate the adjoint model (Heimbach and Bugnion, 2009). The cost function minimizes the weighted square of the difference of squares of measured and predicted velocities (Eq. 5.13). A Tikhonov regularization term is added for stability.

$$J = \gamma_1 \int_{\Gamma_s} w \cdot (U_{obs} - U_s)^2 d\Gamma_s + \gamma_2 \int_{\Gamma_b} (\nabla \alpha \cdot \nabla \alpha) d\Gamma_b \quad (5.13)$$

where γ_1 and γ_2 are scaling factors, Γ_s is the surface domain, Γ_b is the basal domain, $w(x,y)$ is a weighting function, $U_{obs}(x,y)$ are observed surface ice speeds, U_s are modelled surface speeds, and $\alpha(x,y)$ is the control parameter. The control parameter depends on the sliding law, and represents β in the linear sliding law, μ_a in the generalized Weertman sliding law, and μ_b in the Schoof sliding law. The reported errors of surface velocities are used as weights.

5.3.5 Model Integration

Englacial drainage is not considered in the SRLF model. For model integration, we assume that water drainage through the englacial system is strictly vertical, and that there is no horizontal transport in the englacial system. The SRLF model routes water into three different surface drainage pathways: moulins, lake hydrofracture, and crevasses. Moulins and surface to bed connections from lake hydrofracture are treated identically. All water entering these cells drains directly to the bed. However, drainage through crevasse field requires additional consideration. When water enters a cell determined as crevassed in the SRLF model, the water is removed from the model, and no further routing occurs. Since it is unlikely that every crevassed grid cell drains water locally to the ice-bed interface, postprocessing of SRLF output is necessary.

Water drainage through crevasse fields is poorly understood, and the scheme implemented here (Figure 5.3) is motivated by simplicity. We assume all water in crevasse fields drain to bed, neglecting any refreezing. We also assume that contiguous areas of crevassed cells are hydrologically connected, perhaps by an internal water table. A crevassed cell in the SRLF model can accumulate water from two sources: 1) local ablation predicted by RACMO2; 2) a cell which is on the margin of a crevassed area may have water flowing into it from adjacent non-crevassed cells. Modelling (See Section 5.4.1) predicts approximately 70% of the water drained by crevasses is intercepted water flow over the ice sheet surface (source 2). This water is concentrated at the points where supraglacial streams intersect the crevasse fields. The model assumes that moulins exist at these points, as high water input would be favourable to nucleating and sustaining moulins. Moulins are only placed in cells with sufficient drainage, determined by a volume threshold. A value of $5 \cdot 10^5 \text{ m}^3$ is selected, corresponding to approximately the median volume drained by moulins outside of lake basins. A lower threshold results in a rapidly increasing number of moulins draining smaller amounts of water. A veronoi partitioning is then used around the inferred moulins to create internal catchments within the crevasse field. All water in a catchment is assumed to drain in it's corresponding moulin. As stated, the SRLF model does not route water within crevasse

fields; there is no travel time associated with melt in the internal catchments of crevasses and the moulin.

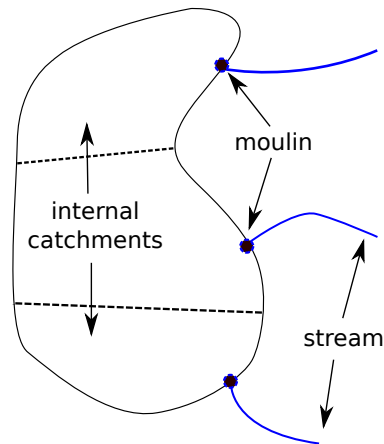


Fig. 5.3 Schematic drawing showing the conceptual model of the crevasse drainage implemented. Moulins are assumed to occur where high-flux supraglacial streams intersect the crevasse field. The crevasse field is then partitioned using Voronoi partitioning into internal catchments. All water in an internal catchments drains to the ice-bed interface at its corresponding moulin.

The supraglacial model is run independently, to determine a time series and location of water inputs to the base. These are then used as input to the coupled subglacial hydrology/ice flow model. A key feedback ignored by this is the influence of surface velocity on lake hydrofracture. However, the current design and computational requirements of the SRLF model make it impossible to run in parallel with the integrated model.

The integration of the subglacial hydrology and ice flow models mirrors that of Hewitt (2013); the subglacial hydrology uses an implicit timestep using the current ice velocity distribution. After the state of the subglacial hydrology model in the next timestep is calculated, the ice model is called to update ice velocities. At each timestep, the basal melting rate is updated. The geometry of the domain is kept constant for the whole run.

5.3.6 Workflow

Figure 5.4 shows the workflow for initializing and running the integrated model. The initial step is to perform an inversion using the linear sliding law over the study area. All linear inversions are run using mean winter velocities from 2009, the most recent year for which data is available. This inversion provides an initial distribution of basal drag and basal velocities to calculate the basal melt rate (Eq. 5.3). The subglacial hydrology model is then run for 240 days holding basal velocities fixed; this corresponds to a run over a winter

season (Sept 1 - April 30). The effective pressures at the end of the subglacial hydrology simulation are then incorporated into an inversion with a non-linear sliding law to determine the background values of the coefficients. These sliding law coefficients, the basal water pressures, and the surface runoff input from the SRLF model form the inputs to the integrated model. The integrated model is then for the summer melt season. As stated in Chapter 4, a key assumption of this procedure is that the mean winter velocities are valid both at the beginning and end of the winter season. Although winter velocities are not constant, published GPS records in Southwest Greenland of winter velocities show limited variability (Colgan et al., 2012; van de Wal et al., 2015).

The inversions are run with constant parameters. Both the winter subglacial hydrology run and the subsequent year-long integrated model runs use the same parameters. A parameter search therefore requires an inversion for each set of parameters tested.

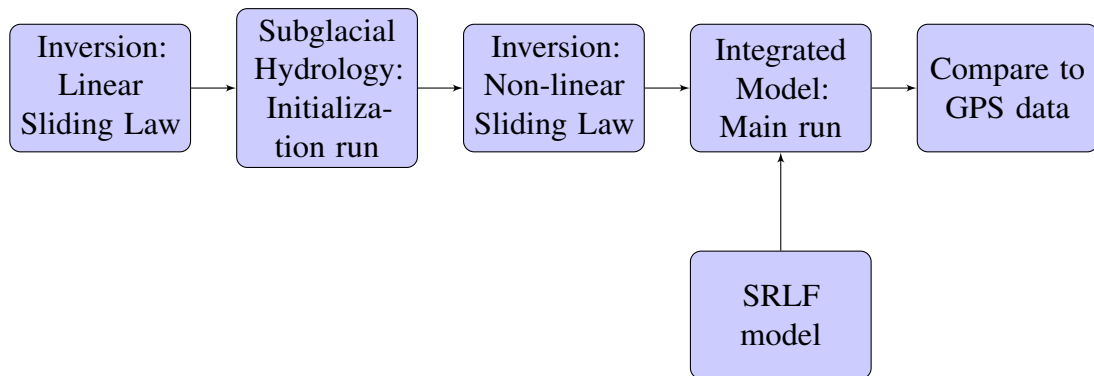


Fig. 5.4 Flow chart showing the work flow for initializing and running the integrated model

5.3.7 Simulations

Five main simulations are run, along with those used in the sensitivity analysis. Two simulations are run calibrating the model using data and inputs for 2009 and 2011. Another simulation is then run validating the model with data and inputs for 2012. The simulations for years 2009, 2011, and 2012 are the modelled melt seasons. Two potential future melt scenarios are simulated by using 2x and 4x the modelled supraglacial input to the subglacial system for 2011. These are referred to as '2011x2' and '2011x4' respectively. The aim of these scenarios is to investigate potential changes in the behavior of the subglacial system, rather than to model a melt season or reliably predict future ice velocities. Accurate predictions of ice velocities would not only require predicted surface runoff, but also depend on predicting changes in ice sheet topography and predicting the future distribution of

supraglacial drainage pathways. Addressing these issues requires careful consideration and are beyond the scope of this thesis.

5.4 Results

5.4.1 Supraglacial Input

The majority of supraglacial meltwater drains into the englacial system (Figure 5.5), consistent with observations (Smith et al., 2015; Zwally et al., 2002) and previous modelling (Chapter 3). Hydrofracture events drain only a small percentage of surface runoff (1.3%). Most drainage (86.1%) occurs through features modelled as moulins: crevasses, surface to bed connections subsequent to lake hydrofracture, and moulins outside of lake basins. Of the water drained by crevasses, approximately 30% is generated locally via ablation in crevassed cells, while 70% is routed into crevasses. Water routing into crevasses is concentrated in a small number of cells, with 50% of water routed over the ice sheet into crevasses entering in only 100 of the 7573 cells forming the perimeter of crevasse fields. Crevasse drainage is concentrated near the ice margin (Figure 5.6), while drainage into other pathways occurs throughout the study area.

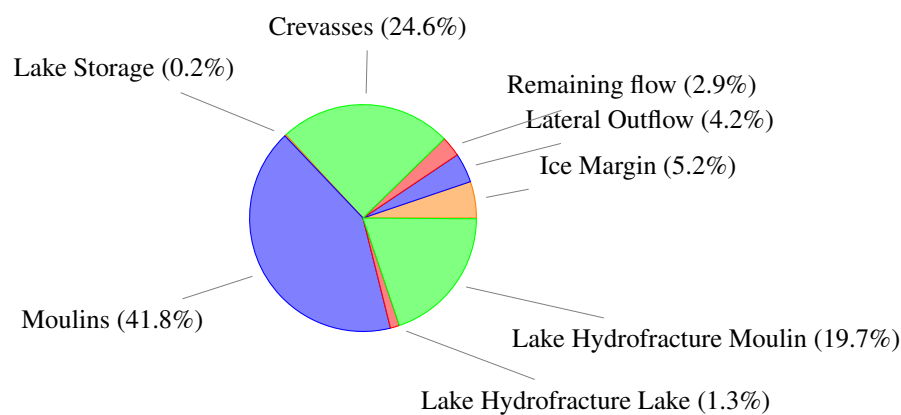


Fig. 5.5 Pie chart of surface runoff partitioning into different meltwater pathways for the 2009 melt season in the SRLF domain. Water flowing over the western boundary is categorized as 'Ice Margin', while water flow over the lateral boundaries is labelled as 'Lateral Outflow'. 'Remaining Flow' refers to water still flowing over the ice sheet at the end of the model run. Water flowing into crevasses and moulins are in categories 'Crevasses' and 'Moulins' respectively. 'Lake Storage' refers to water in lakes at the end of the simulation. 'Lake Hydrofracture Lake' refers to the water in lakes that is drained by hydrofracture events themselves. 'Lake Hydrofracture Moulin' refers to water drainage into the subsequent surface to bed connections from hydrofracture events (as in Chapter 3).

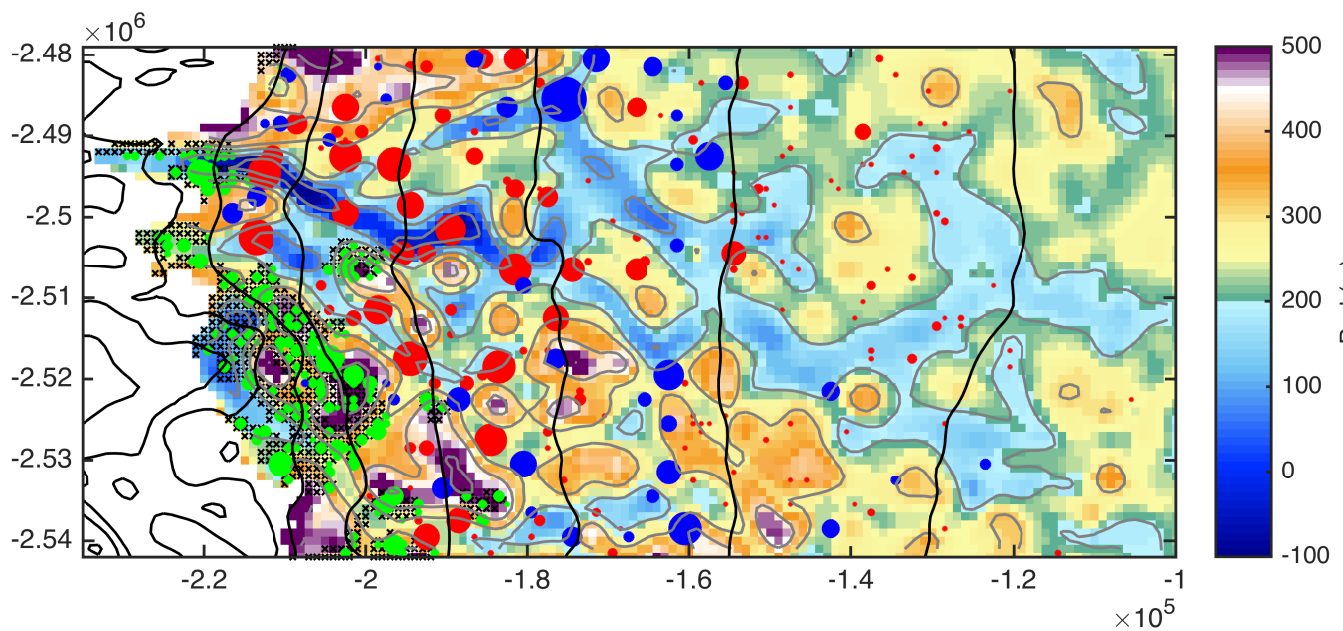


Fig. 5.6 Modelled supraglacial input in the Russell Glacier area for the integrated model domain in 2009. Meltwater pathways are denoted by circles of different colors, with red, green, and blue corresponding to moulins, crevasses, and lakes respectively. Circle areas are scaled by volume. Hatch marks show grid cells calculated as crevassed. Crevasse inputs appear within hatched areas due to resampling from 90 m to 1000 m resolution. Background is basal topography from BedMachine2 reinterpolated at 1000 m. Light gray contours correspond to 100 m basal contours. Black lines correspond to 200 m surface topography contours at the same elevations as in Figure 5.1.

5.4.2 Calibration

Modelled velocities are calibrated against GPS measurements of horizontal surface velocities from 2009 (Figure 5.7) and 2011 (Figure 5.8). The model is calibrated using the Weertman sliding law, and the same parameter values are used in the simulations with the Schoof sliding law. Plots show model velocities output at noon for the Weertman sliding law, and daily averages calculated from output at 6 h intervals for the Schoof sliding law. Sub-daily variability in model output is relatively subdued, except during periods of high velocities in simulations applying the Schoof sliding law (see Appendix 1). All model output values shown are from the summer immediately following the winter initialization. There are only minor differences between this model output and from running the model for an additional year and using the output from the second summer. Since surface water input to the subglacial hydrological system is a key driver of ice velocities, surface runoff from RACMO2 and nearby surface ablation rates determined at weather stations (van de Wal et al., 2015) are plotted alongside velocities. RACMO2 surface runoff forces modelled ice flow, while the weather station ablation rate is taken as representative of the water input driving measured ice velocities. Some caution is necessary comparing the datasets, since RACMO2 accounts for both refreezing of meltwater and precipitation events. Refreezing, however, should only be a small component (van de Wal et al., 2015). An error of 5% is estimated for the calculated daily ablation rates (van de Wal et al., 2015).

The Schoof and Weertman laws result in model output of comparable fit to the measured velocities for large segments of the velocity time series. However, during periods of high velocities, the Schoof law can overpredict the magnitude of the velocity by a factor of 3. Model output with the Schoof sliding law is also observed to have a sharper and higher magnitude summer speedup, as well as a slight increase in velocity variability. Since the Weertman sliding law results in an overall better match to the measured velocities, this chapter focuses on model output from the Weertman sliding law. The results for the remainder of the chapter use the Weertman sliding law, except for model validation where the output of model runs using both sliding laws are shown.

Near the ice sheet margin, the model predicts low ice velocities throughout the summer melt season. In general, measured GPS velocities are also relatively low, except for early high magnitude variability observed at sites S1-S3 (Figure 5.7a-c) in 2009, and at sites S1-S2 in 2011 (Figure 5.8a-b). This observed variability in the GPS velocities precedes melt predicted by RACMO2 and is not reproduced by the model. At site S1, modelled velocities show limited acceleration during the summer in both 2009 and 2011, similar to the mid-late summer GPS measurements. At site S2, the model under predicts GPS velocities in both years. The fit improves at site S3 for both years, as modeled velocities in 2009 approximate

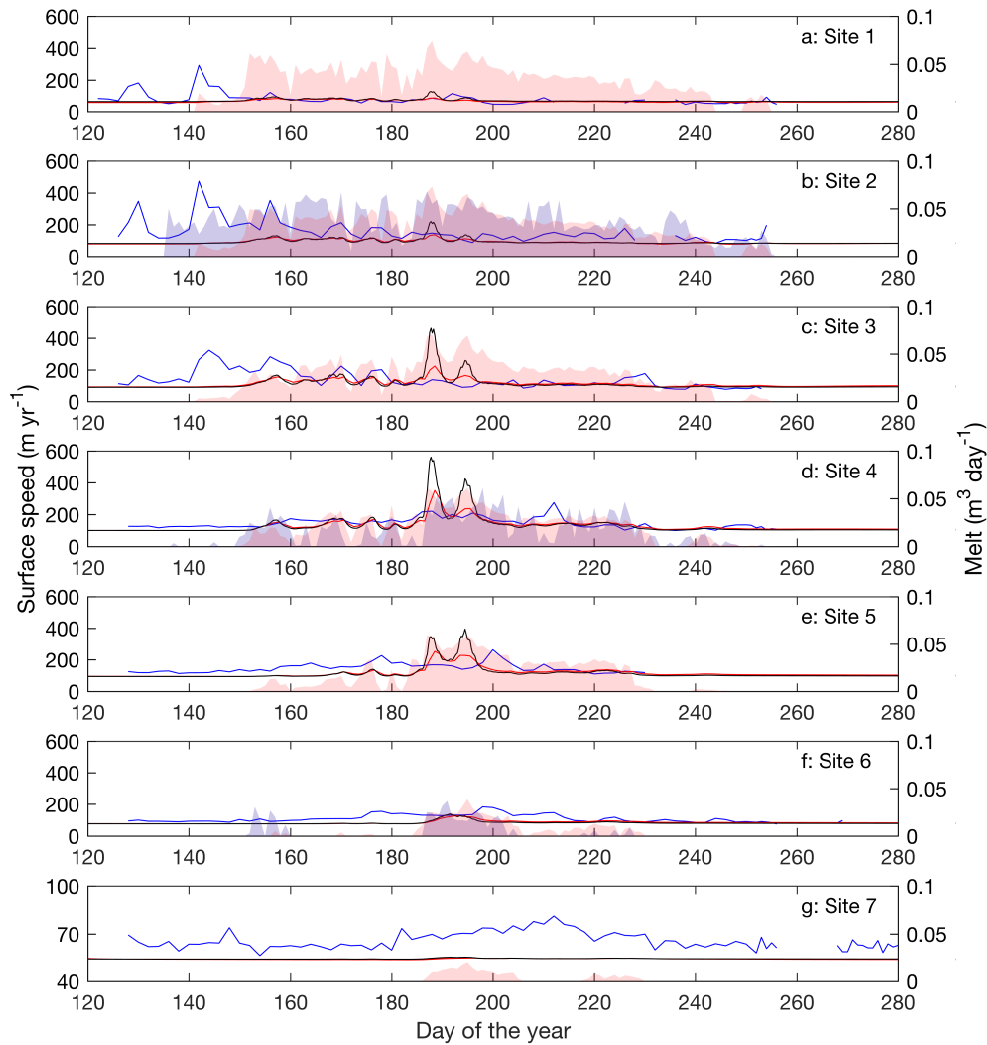


Fig. 5.7 Modelled ice velocities plotted against GPS measurements for the 2009 melt season. Daily average horizontal velocity from GPS measurements are plotted in blue. Modelled velocities using the Schoof sliding law and Weertman sliding law are plotted in black and red respectively. Modelled velocities at the start of the run are shown in a black dashed line. Daily ablation from weather stations are shown in shaded blue, while RACMO2 surface runoff is shown in shaded red. Locations of GPS and weather station sites are shown Figure 5.1. Weather station ablation rates are plotted at the nearest GPS site.

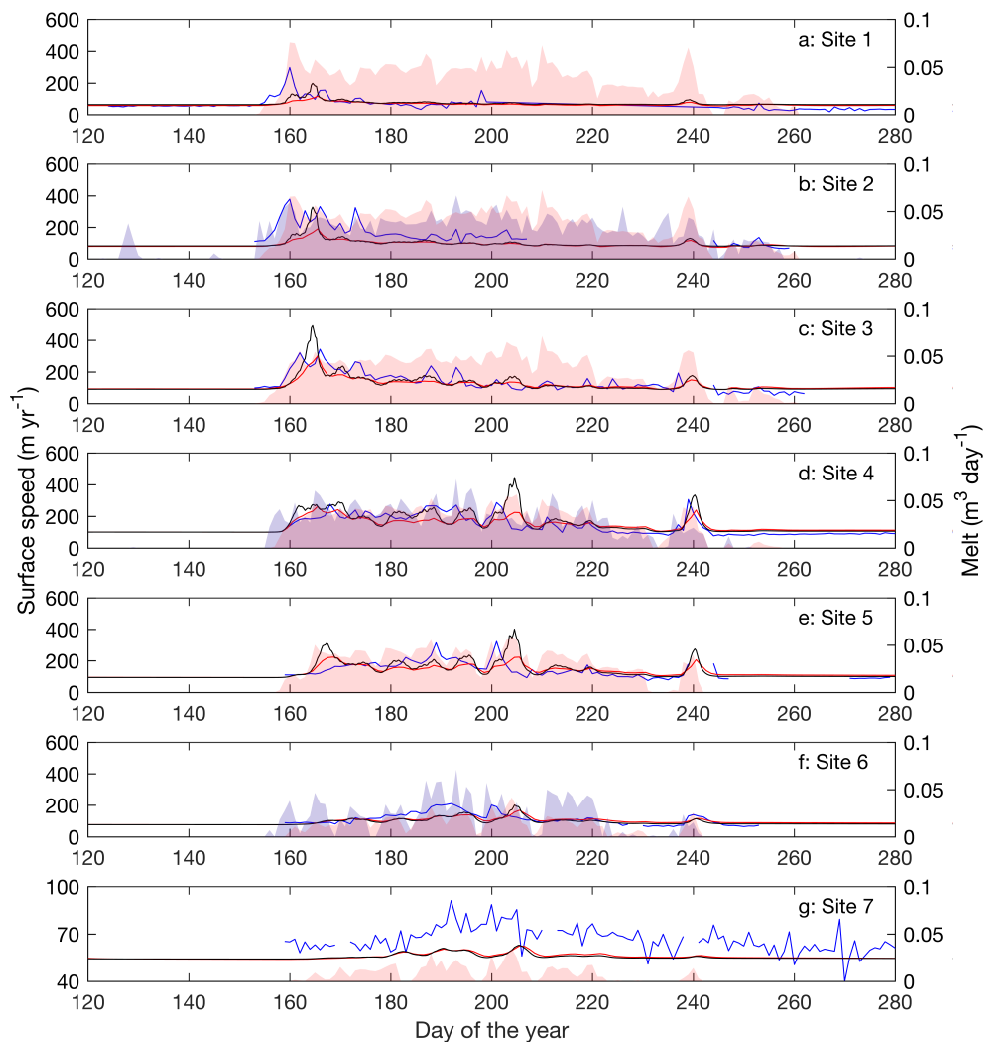


Fig. 5.8 Modelled ice velocities plotted against GPS measurements for the 2011 melt season. Daily average horizontal velocity from GPS measurements are plotted in blue. Modelled velocities using the Schoof sliding law and Weertman sliding law are plotted in black and red respectively. Modelled velocities at the start of the run are shown in a black dashed line. Daily ablation from weather stations are shown in shaded blue, while RACMO2 surface runoff is shown in shaded red. Locations of GPS and weather station sites are shown Figure 5.1. Weather station ablation rates are plotted at the nearest GPS site.

summer velocities following early initial summer variability, while in 2011 the model also predicts the early summer speedup.

Modelled velocities at sites S4-S5 (Figure 5.7d-e and Figure 5.8d-e) capture the seasonal trend of ice flow, and mirror some of the observed short-term speed-up events. Modelled velocities at S4 match the general flow while diverging from GPS measurements during periods of observed and modelled enhanced flow. In 2011 modelled ice flow shows similar short-term speedup events as the GPS measurements, such those beginning on days 198 and 237. At site S5, the model does not predict the gradual speedup observed in the GPS velocities. Similar to the GPS measurements, there is a brief period of enhanced flow in mid-summer, followed by a slowdown. In 2011, however, the model captures the early velocity speedup, and the general trend through the remainder of the summer, including the same speedup events observed at site S4.

Model velocities underpredict the measured velocities at the highest sites. In 2009, site S6 (Figure 5.7f) shows a gradual velocity increase in the first half of the melt season, followed by a gradual decline in the second half. Neither the increase nor decrease in velocity mirrors the weather station ablation rate. In contrast, model velocities are observed to be enhanced in the middle of summer, mirroring modelled melt. Site S6 (Figure 5.8f) shows faster flow in 2011 than in 2009. The model velocities match the initial velocity increase observed in GPS velocities, but do not reach the same magnitude. A late summer slowdown is observed in both the modelled and measured velocities, as are short-term increases in velocities at days 200 and 240. At site S7, modelled velocities depart from the winter mean by a few meters per year in both 2009 and 2011 (Figure 5.7g and Figure 5.8g). Measurements show an increase on the order of $10\text{-}20 \text{ m yr}^{-1}$ in both 2009 and 2011.

In summary, the early summer speedup and subsequent mid summer slow-down at mid-elevations are captured. The model is also able to reproduce the pattern of synchronous speedups observed at multiple adjacent GPS stations. Consistent features not captured are early summer variability at low sites, short term variability, and late summer deceleration below the winter mean. Modelled velocities are only observed to flow slower than the winter velocity mean for a period of a few days and by a small magnitude ($< 5 \text{ m yr}^{-1}$).

Ablation rates calculated from automatic weather stations near to sites S2, S4, and S6 are comparable to predicted RACMO2 surface runoff. The two data sets show similar magnitude at sites S2 and S4, with higher variability in ablation than runoff. At S6, both ablation and predicted runoff are similar in 2009, while in 2011 ablation is approximately twice the magnitude of surface runoff and has a much higher variability. Qualitatively, model velocities at sites S1-S3 do not correlate to predicted surface runoff, while they do show correlation at

sites S4-S6. GPS measurements do not in general show correlation with the ablation rate at S2, and appear only mildly correlated at S4 and S6.

5.4.3 Model Sensitivity

Calibrating the integrated model is an underdetermined problem. Multiple parameters in each cell across the grid are constrained using only seven times series of point GPS data. The parameters selected for the subglacial hydrological model are not unique in giving a qualitatively good fit, and approximately similar fits were observed with different variations of parameters. Within the parameter space searched, different sets of parameters either enhanced or dampened the magnitude of the velocity output, or resulted in a velocity signal that significantly diverged from GPS measurements. Extensive sensitivity analysis of the subglacial hydrology component of the integrated model to parameters are conducted in Werder et al. (2013) and Hewitt (2013). In this section, the focus is sensitivity of the model to the setup, and the parameters selected to have a spatially heterogeneous distribution. Figures corresponding to the sensitivity analysis are in Appendix 1.

Drainage through crevasses is poorly constrained, and hence the impact of varying crevasse drainage is tested. Velocities at the GPS stations are not found to be sensitive to variations in crevasse drainage. The standard value of the moulin volume threshold of $5 \cdot 10^5$ resulted in crevasse input partitioning into 182 moulins and internal catchments. Changing the threshold value to 10^5 and 10^6 , resulted in 337 and 122 internal catchments respectively. Model output in both scenarios showed negligible changes. Similarly, neglecting water generated over crevasse fields and only using water flowing into the crevasse fields from external streams had little impact on modelled velocities at the GPS stations.

Lake hydrofracture events result in a large volume of water rapidly draining to the base during the event itself, and a surface to bed connection which drains water for the remainder of the melt season. The impact of the initial rapid delivery of water is tested by running a simulation where the water in the lake when hydrofracture occurs is not input to the base. The impact on ice velocities was found to be negligible.

The GPS records in 2009 and 2011 show differing characteristics, with ice velocities in 2009 showing much less variability and more gradual changes than 2011. The choice of the parameter value setting for englacial storage (σ) attempts to balance the fit in both years. A better fit was observed with increased englacial storage for 2009 and less englacial storage in 2011. Increased capacity of englacial storage had the effect of dampening the velocity output. In 2009, this increased the fit of the model predictions by reducing the high velocities observed at sites S3-S5 between days 180 and 200. However, increased englacial storage

also reduced the velocity speedups observed in 2011, particularly around day 2015, reducing the fit to GPS measurements.

A variable sheet conductivity is found to benefit the fit of modelled velocities by increasing the magnitude of the early summer speedup. The results using a constant value of 10^{-2} are overall very similar to the calibrated run, while decreasing the sheet conductivity value to 10^{-3} leads to model output with prolonged periods of velocities exceeding 400 myr^{-1} . Increasing the initial coverage of lower conductivity nodes assigned a value of 10^{-7} from 15% to 30% had a minor impact. Assigning 50% of the initial nodes resulted in a worsening fit early in the summer at site S4, but had little impact at other sites or beyond the initial speedup. Patterning low conductivity nodes into 4x4 patches, randomly seeded at 125 points was also tested. The number of patches was selected so that if there was no overlap of the patches, 20% of the nodes would be assigned a lower conductivity. Two simulations were conducted with different random locations of patches. One simulation strongly impacted the early summer speedup at site S3 and S4, while the other had a similar effect but on sites S4 and S5.

5.4.4 Validation

The integrated model is validated against GPS velocity measurements from 2012. The pattern of modelled velocities at sites S1 and S2 are similar to those in 2011, with a moderate early velocity speedup followed by a gradual slowdown for the remainder of the summer. Unlike previous years, GPS velocities at site S1 do not exhibit high magnitude velocity variations, improving the match of the modelled velocities. Although the integrated model does not respond strongly to melt input for most of the summer at site S1, it does predict elevated velocities in line with GPS measurements to late season input around days 255 and 265. At site S2, the general pattern of speedup observed in the GPS velocities is mirrored by the modelled velocities. However, the magnitudes are consistently under predicted, particularly those of the short-term high magnitude speedups. The magnitude of modelled velocities improves at site S3, with both magnitude and timing of events at site S4 matching GPS measurements. Minimum GPS data is available at sites S5 and S7. Similar to previous years, model output underpredicts GPS velocities at site S6.

5.4.5 Future Scenario

Increasing melt input accelerates the rate of the early summer speedup and results in a higher peak velocity (Figure 5.10). Following the early summer speedup at sites S1-S3, simulations 2011, 2011x2, and 2011x4 all predict similar velocities.

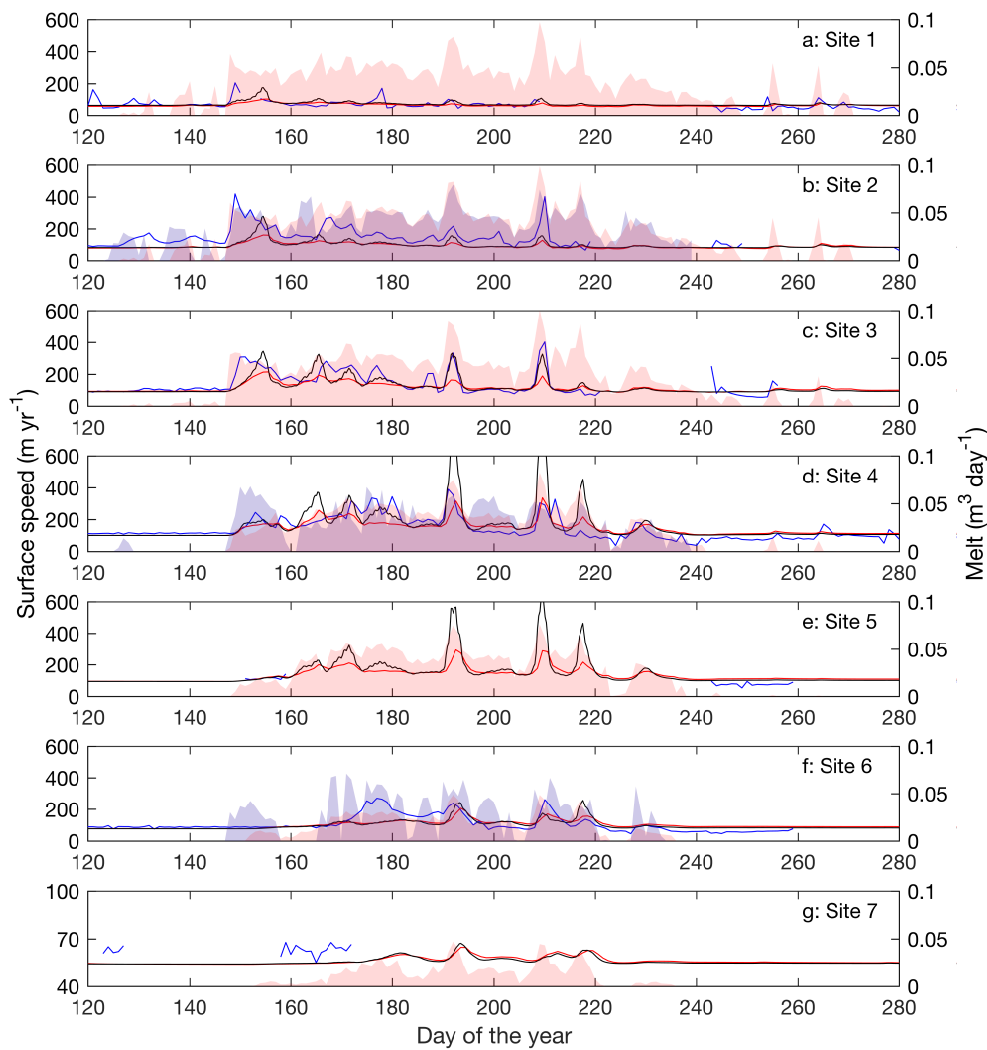


Fig. 5.9 Modelled ice velocities plotted against GPS measurements for the 2012 melt season. Daily average horizontal velocity from GPS measurements are plotted in blue. Modelled velocities using the Schoof sliding law and Weertman sliding law are plotted in black and red respectively. Modelled velocities at the start of the run are shown in a black dashed line. Daily ablation from weather stations are shown in shaded blue, while RACMO2 surface runoff is shown in shaded red. Locations of GPS and weather station sites are shown Figure 5.1. Weather station ablation rates are plotted at the nearest GPS site.

At sites S4-S6, increased melt input results in higher variability of ice flow in the first half of the summer season. Modelled velocity is observed to increase with melt input at these sites during the first half of summer. The relative increase of velocities between 2011x2 and 2011x4 is greater than between 2011 and 2011x2. At sites S4-S6 the model predicts similar velocities in all three simulations for the latter half of summer from days 210 and 238. During this period at site S4, model velocities decrease with simulation melt input (not visible on plot). 2011x2 is approximately 10 myr^{-1} slower than 2011, while 2011x4 is also $\sim 10 \text{ myr}^{-1}$ slower than 2011x2. At site S6, modelled velocities increase with greater melt input. Site S5 shows mixed behavior, with model velocities from simulation 2011x4 higher than the simulation between days 210 and 222, whilst lower between days 223 and 236. Between days 210 and 238 at sites S4-S6, model velocities are low and only slightly elevated above their winter values. Starting at day 238, a late season velocity spike is observed, with the magnitude of the velocity increase dependent on melt input. At site S7, the velocities from future simulations are slightly faster than 2011 velocities. Overall, the timing of events is similar in all three simulations. As melt input doubles, the magnitude of short-term velocity spikes increases as well. However, the increase between 2011x2 and 2011x4 is greater than between 2011 and 2011x2.

5.4.6 Average Melt Season Velocities

Melt season averaged modelled velocities at the GPS sites are shown in Figure 5.11. Average velocities are highest at GPS site S4, and decrease towards the ice margin and at high elevations. Average velocities increase with melt season intensity at all GPS sites, with a pattern skewed away from the ice margin. As melt season intensity increases, velocities in the upper ablation zone and at the equilibrium line (located at 1500 m elevation (van de Wal et al., 2015), slightly above S6) are predicted to increase the most. Average velocities increase non-linearly (comparing 2011, 2011x2, and 2011x4). The pattern observed at the GPS stations is reflective of that across the study domain (Figure 5.12). Overall, areas of slow flow are predicted to accelerate faster than areas of fast flow. Average velocities between 2009 and 2011x4 increase by up to 70%.

5.4.7 Channel Network Morphology/Extent

The development of the channelized system (see supplementary videos) is similar to that observed in previous modelling studies (e.g Banwell et al., 2016; Hewitt, 2013; Werder et al., 2013) and as inferred from observations (Bartholomew et al., 2011b; Chandler et al., 2013). Channelization of the hydrological system begins at the margin and develops progressively

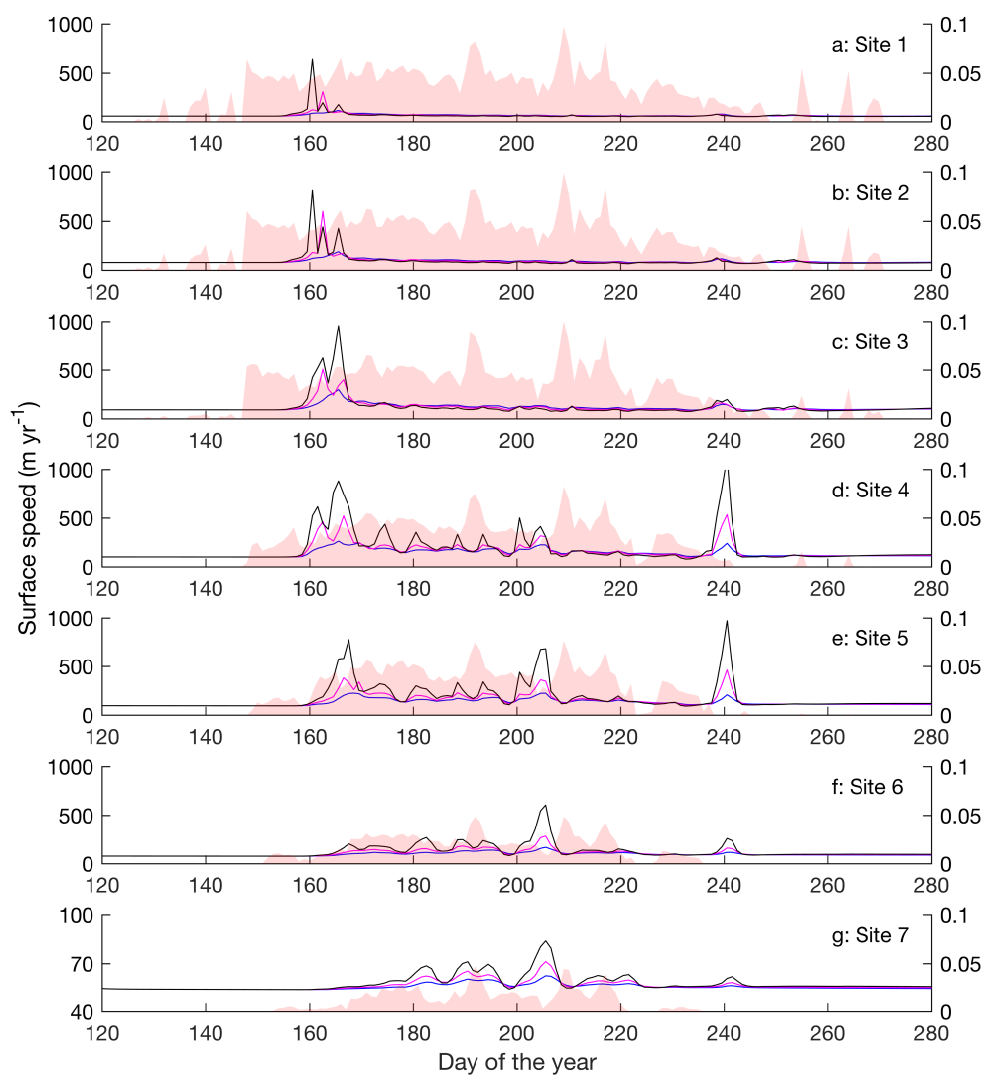


Fig. 5.10 Modelled ice velocities plotted for the 2011 melt season (blue), the 2x melt scenario (magenta), and for the 4x melt scenario (black). Modelled velocities at the start of the run are shown in a black dashed line.

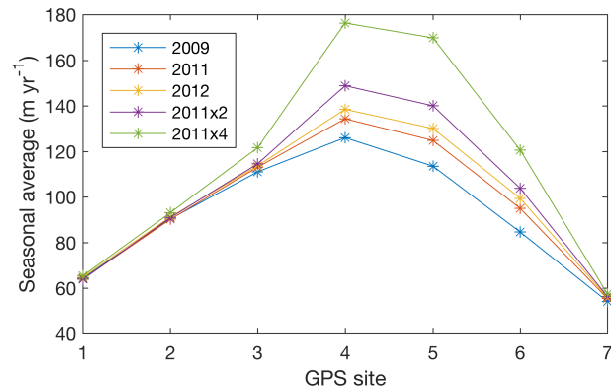


Fig. 5.11 Averaged modelled melt season velocities at each of the GPS sites.

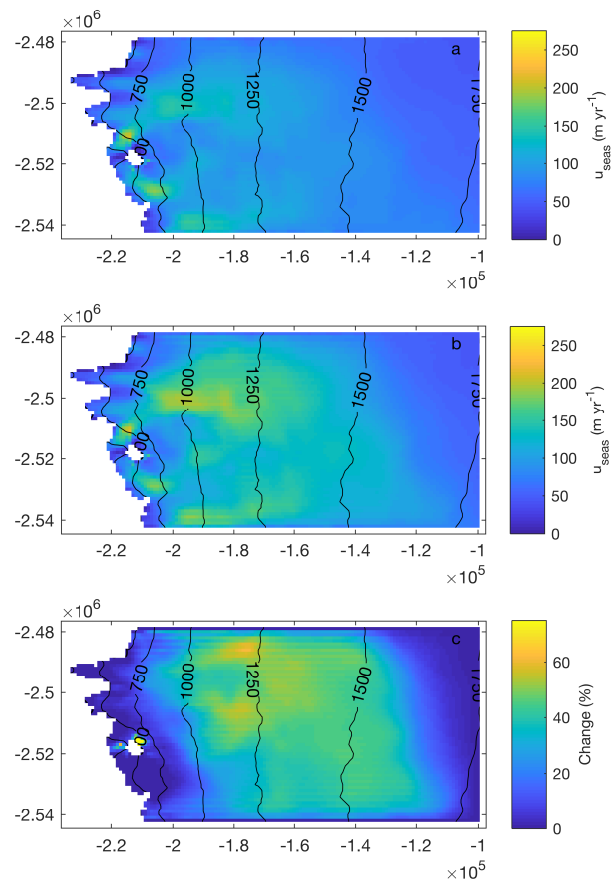


Fig. 5.12 a) Map of melt season average velocities for 2009. b) Map of melt season average velocities for 2011x4. c) Change (%) between the melt season average velocities of 2009 and 2011x4.

up ice-sheet. As channelization develops up-ice, the system evolves to an arborescent morphology. The up-ice extent of channelization increases with summer melt intensity (Figure 5.13). In 2009, channels occur primarily below the 1000 m surface elevation contour. The extent increases past 1100 m, and approaches 1200 m, in 2012. As melt season intensity increases from 2009 to 2012, pockets of channelization at higher elevations are seen. The maximum extent of channelization occurs at approximately the same time in each modelled melt season, and was qualitatively identified to occur between days of the year 220-225 in all three melt seasons. Although the extent of channelization varies between 2009, 2011, and 2012, there are no significant differences in the organization of the channelized system. In the future scenario 2011x4 the morphology of the channelized system is similar to that in the modelled melt seasons. However, the extent increases further upstream past 1300 m and approaches 1400 m

Figure 5.13 shows the locations of moulins used as tracer injections points in Chandler et al. (2013). Except for moulin IS39, tracers injected into the moulins drained from the subglacial system at an outlet located near moulin L1. Tracers injected into IS39 are reported to drain from an outlet of an adjacent catchment. The channel morphology in the modelled melt season output does not predict a major outlet located near L1, nor that L41 and L57 would drain near L1. However, the model does predict that IS39 is on a different branch of the channelized system. Based on tracer measurements, Chandler et al. (2013) report that channelization extends to at least L41, but not as far as L57. The modelled channelized system during 2009, 2011, and 2012 is inline with that result.

5.4.8 Distributed and Channelized Discharge

Water flow beneath the ice sheet is modelled to occur in interacting distributed and channelized systems. The discharge in each system follows similar trends for all three modelled melt seasons (Figure 5.14). In 2009, 2011, and 2012, integrated discharge over the summer melt season in the channelized system is slightly less than half (43%-48%) of the integrated discharge in the distributed system. Modelled discharge begins to increase simultaneously in both systems at the start of the melt season. In 2011 and 2012, discharge in the distributed system rapidly increases in the early melt season. This is followed by a long period with overall high flow but with strong variations. At the end of the melt season, discharge in the distributed system rapidly decreases. In 2009, the early season increase in discharge is less rapid and more prolonged, and discharge peaks before decreasing to a plateau, after which it rapidly decreases. Discharge in the channelized system increases at a much slower rate, and tends to increase until mid-late summer. It mirrors many of the short-time scale variations in the distributed system but with a dampened magnitude. At the end of the melt

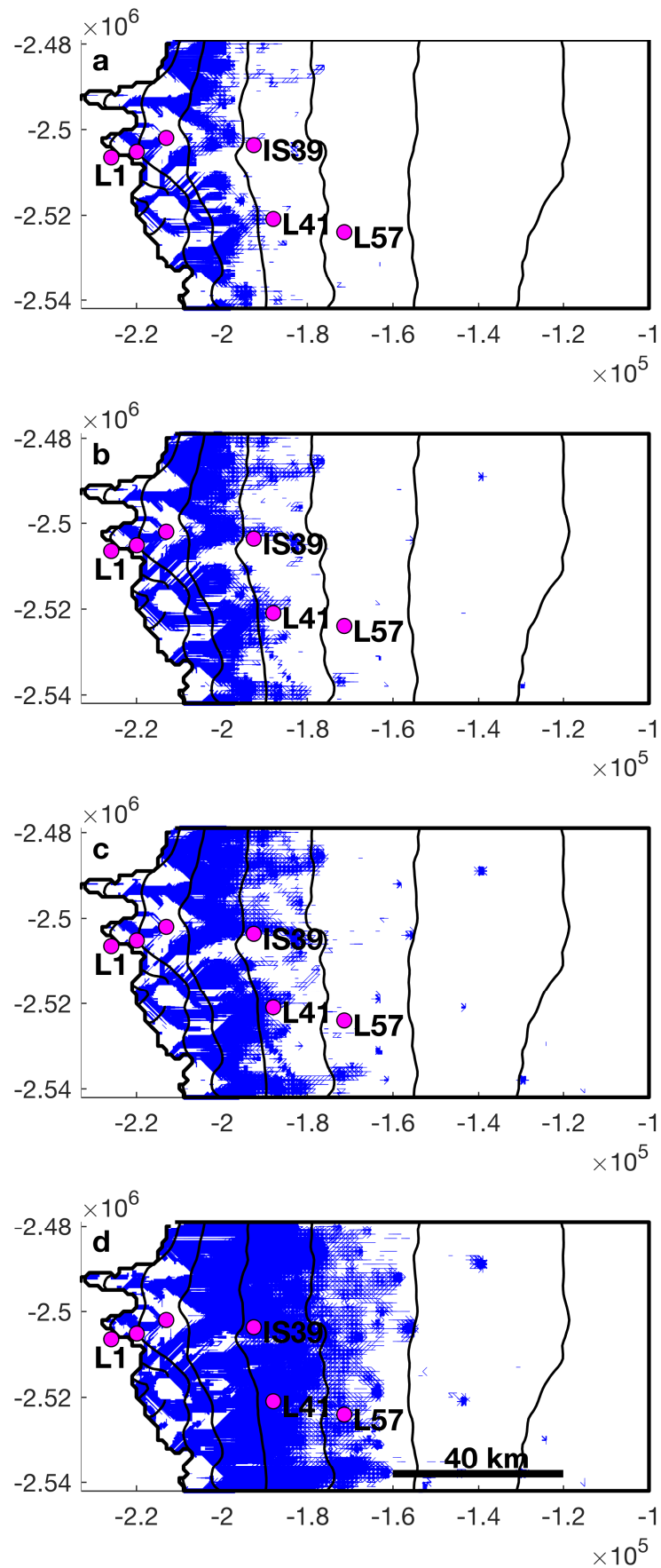


Fig. 5.13 Channelized system at maximum extent: a) 2009. b) 2011. c) 2012. d) 2011x4. Moulin locations used as tracer injections sites in Chandler et al. (2013) are shown in purple. Black lines correspond to 200 m surface topography contours at the same elevations as in Figure 5.1.

season, discharge in the distributed system decreases at a higher rate than in the channelized system, so that there is a brief period in which discharge in channels is higher than in the distributed system. Under the future melt scenario 2011x4, the integrated discharge in the channelized system increases to 77% of the integrated discharge in the distributed system. Early in the melt season, discharge increases in both the channelized system and distributed system simultaneously. Similar to the modelled melt seasons, discharge in the distributed system increases at a faster rate. However, peak discharge in the channelized system is nearly the same magnitude as peak discharge in the distributed system, and discharge in the channelized system exceeds that of the distributed system earlier in the year.

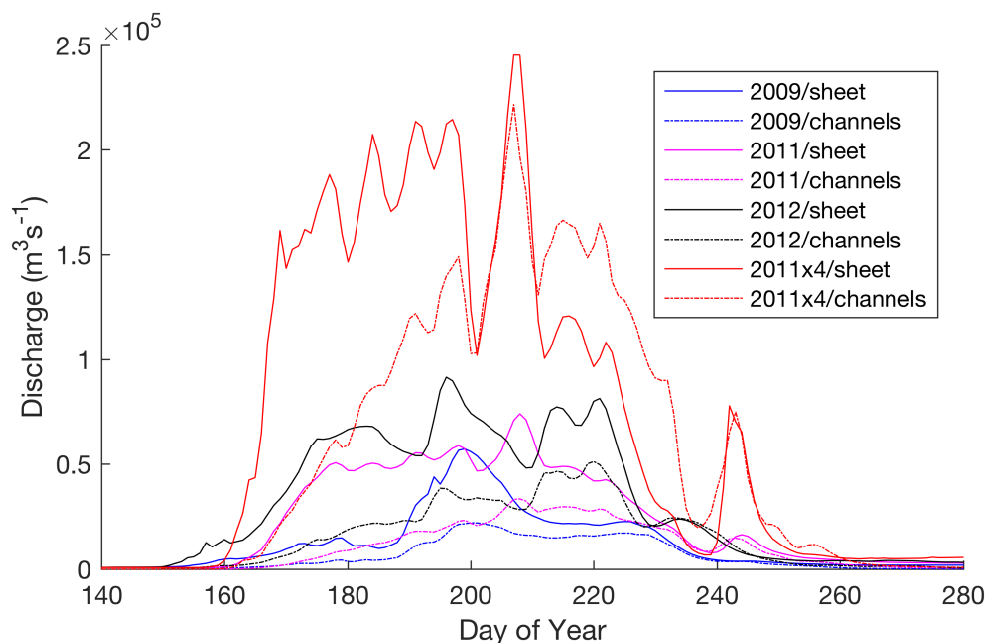


Fig. 5.14 Time series of discharge in the distributed and channelized system for three different summers and a future melt scenario.

5.5 Discussion

5.5.1 Model Fit

The modelled velocities are the combined result of five models (RACMO2, SRLF, an ice sheet model, the associated adjoint model, subglacial hydrology model) and several datasets. Most parameters used in the models are assigned standard values, with calibrated parameter values for the subglacial hydrology model. The validation simulation affirms the calibrated model, as measured velocities are reproduced to the same qualitative level of fit. Although

each model has biases and is limited by assumptions, their combined result reproduces measured ice velocities to a first order. Many of the features observed in the GPS time series are captured in the modelled velocities. This gives confidence that the models and datasets are representative of their respective component. The complexity of the models, and the process, makes assigning a model uncertainty infeasible. It is unclear how to partition the cause of model mismatch between: errors in inputs such as topography, model/theoretical uncertainty such as the form of the sliding law, or computational imposed limitations such as grid resolution or choice ice sheet model.

Overall, model velocities are observed to be better at mid-elevation than either at the lowest or highest sites. Model velocities at sites S1-S2 are likely affected by the model not recreating the subglacial water routing inferred by Chandler et al. (2013). A number of factors could contribute to differences in water routing, including errors in topographic data, the spatial distribution of inputs from crevasse fields, and model assumptions and boundary conditions. In general, thin ice and steep gradients in topography make ice flow and hydrology modelling near the margin difficult. Thin ice deviates from the assumption of a high aspect ratio in the hybrid formulation, while steep gradients are likely to lead to stresses assumed negligible in the stress balance. Drainage components in the subglacial hydrology model are formulated in terms of effective pressure, on the implicit assumption that they remain full. Underneath thin ice, or when there are steep gradients, both channels and cavities could be expected to exist while partially full or empty. The atmospheric pressure prescribed at the ice sheet margin, may in reality, extend inland for periods in the summer. The high velocity spring events observed in the GPS records occur before any melt is predicted by RACMO2. Similar to Bougamont et al. (2014), modelled velocities do not capture any of this behavior. These may be the result of internal dynamics of water stored over winter, such as flooding events, that the subglacial hydrology model cannot capture.

Modelled velocities at sites S6-S7 may be affected by excess capacity in the cavity system due to over prediction of basal ice velocities from the inversion process. The inversion process results in a sliding ratio of approximately 0.8 at the high elevations (see Chapter 4). However, internal deformation can be expected to be dominant over basal sliding so far inland, suggesting a much lower sliding ratio. Measurements at boreholes in the Paakitsoq region at lower elevations show a sliding ratio of 0.44-0.73 during the winter, increasing episodically to 0.9 during the summer (Ryser et al., 2014). The largest discrepancy between ablation at a weather stations and RACMO2 modelled surface runoff occurs at site S6, likely due to RACMO2 allowing for refreezing of surface melt. This additional complexity increases the uncertainty in runoff predictions, and surface input to the base may be underestimated at sites S6 and S7.

Spatial maps of modelled velocities show numerical artifacts; the numerical grid used to compute velocities is visible during periods of enhanced flow (see supplementary videos). Although these do not appear to have a strong direct impact on the velocities at the GPS stations, numerical artifacts are a cause for concern and should be mitigated in future work. During speedup events, high velocity gradients occur near the lateral study site margins due to the Dirichlet boundary conditions. High velocity gradients increase the viscosity, leading to greater internal deformation. The implicit calculation of internal deformation likely results in the Picard Iterative process not fully converging to a solution. This could be mitigated in the current model and configuration by using a Newton-Raphson method instead of Picard Iterations for solving the non-linear momentum equations, although at the expense of computational time. Since ice flow in the region is nearly parallel to the study domain boundary, alternative boundary conditions could be used. Using a no penetration boundary condition and a Robin boundary condition for lateral shear stress may resolve the numerical artifacts. A potential contributing factor to numerical artifacts is that internal deformation is determined using the basal drag of the local grid cell. Strong variations in basal drag due to subglacial hydrology likely impact convergence since the hybrid model formulation assumes horizontal gradients in vertical velocities are negligible. Calculating the horizontal velocity profile using a spatially averaged basal drag rather than the local value may improve convergence.

5.5.2 Model Sensitivity

Model velocities calculated with the two different sliding laws are comparable during much of the melt season. The timing of events are not effected by the choice of sliding law, and the primary difference observed is the magnitude of velocities during short-term speedup events. The overprediction of speedup during events with the Schoof sliding law suggests adding a regularization constant, such that a minimum basal drag exists. Such a term could reflect the fact that the subglacial hydrological system may not extend throughout a gridcell, or that part of the cell has a weakly connected system with a different water pressure (Hoffman et al., 2016). Simulation results shows the Weertman sliding law with standard exponent values has practical value in simulations. However, the form and parameters of the sliding law remain uncertain, and the Schoof law has greater theoretical support (Hewitt, 2013).

Calibrating the integrated model is an underdetermined problem, as the number of observations is not sufficient to constrain the parameters in all the models. The calibration therefore focuses on the key parameters of the subglacial hydrology model, while keeping parameters of the ice sheet model and surface hydrology model constant. The calibration was achieved mainly by trial and error, starting with values used in Hewitt (2013). Most model

parameters of the integrated model are similar to previous studies applying the subglacial hydrology model (Banwell et al., 2016; Hewitt, 2013). The most significant parameter value difference is the sheet conductivity. The primary value of 10^{-2} is between the order of magnitudes of 10^0 and 10^{-5} used in Hewitt (2013) and Banwell et al. (2016) respectively. The parameter values for the model reported in Banwell et al. (2016), which are calibrated against observed water discharge at an outlet in the Paakitsoq region, were found not to reproduce GPS velocity records, as water at mid-high elevations was not effectively evacuated. The difference in parameters suggests that care needs to be taken transferring parameter values between study sites in different areas and of different scales.

The calibrated value for sheet conductivity is at the higher end of inferred values for till (Fountain and Walder, 1998). Although model results are no longer comparable when sheet conductivity decreases by an order of magnitude, model results are resilient to heterogeneity. The simple tests conducted suggest that random heterogeneity in sheet conductivity has a lower impact than larger-scale spatial patterns. Heterogeneity in sheet conductivity could arise from local topography, variable till coverage, and till properties (including deformational history). A constant sheet height scale of 0.5 m is selected as a reasonable value in this chapter. However, patterns of sheet thickness would also provide a strong control on discharge at the base. Overall, model results suggest it is necessary for the distributed system to be able to sustain a high discharge.

The initial rapid delivery of a large volume of water to the bed during lake hydrofracture events are not observed to have a pronounced effect in modelled velocities. This suggests that lake hydrofracture events are not a key process in the long term or large scale development of the subglacial hydrological system. At lower elevations, the numerous conduits and high water input drive channelization, while at higher elevations, a combination of insufficient input and conditions unfavourable for channelization exist. Rather, the primary impact of lake hydrofracture is in opening surface-to-bed connections, which then drain a significant proportion of the overall surface melt.

The configuration of internal catchments and moulins which drain crevasses was not found to have a strong impact; neither was eliminating drainage of water generated from ablation in internal catchments. However, the GPS sites at which model velocities are compared do not capture spatial heterogeneity of crevasse drainage, which occurs along the length of the ice margin. Hence, the impact may be much stronger at other locations within in the study area. However, since model velocities at higher GPS sites were not observed to vary with changes in crevasse drainage, the impact of crevasse drainage should be limited to the margin.

5.5.3 Model Complexity

It is encouraging that the results provide a good match to observations, particularly at the relatively coarse resolution used. However, the models and workflow applied in this chapter are characterized by a high degree of complexity. An important consideration is where simplifications can be applied, and where further complexity may be justified.

The use of a higher-order ice sheet model/inversion code should be explored due to increased accuracy in basal velocity calculations. Basal velocities are a key control of the subglacial hydrological system since they determine cavity spacing and provide an important feedback (Hoffman and Price, 2014). A higher order model may perform more robustly throughout the study area. Areas where the performance of the hybrid model may be expected to be sub-optimal occur throughout the study area. Such areas are characterized by: low aspect ratio, high variability in basal topography, or low sliding ratio. The ice flow model is also constrained by the assumption of a uniform temperature distribution throughout the ice. Calculating a thermal-mechanical steady state, or alternatively inverting for the structure, would increase accuracy of calculated basal velocities. Either of these options could be incorporated in the step with the linear inversion at limited cost since this step is only executed once. Importantly, both the use of a higher order ice sheet model and determination of the thermal state can be implemented without adding further assumptions or unconstrained parameters.

The subglacial hydrology model is the least constrained model in the workflow. Many parameters remain unknown and the exploration of its behavior is limited by the parameter space searched. However, a key behavior not observed in is the winter slowdown and subsequent slow winter acceleration. The integrated model returns to its initial state at the end of summer. This indicates a need for a component of the model which operates on a longer timescale than is currently included. The difficulty in recreating both the smoother 2009 velocity record and the more variable 2011 record also suggests inter-annual variability in the background state of the hydrological system. A model component simulating weakly connected regions of the hydrological system as incorporated in Hoffman et al. (2016) may be key to reproducing these observations. These regions are conceptualized as parts of the distributed system with a much lower hydraulic connectivity. The connectivity of these regions may be temporally variable.

The SRLF model offers the best opportunity for simplification. To at least a first order, lakes which hydrofracture can be modelled as moulins (in line with observations by Hoffman et al. (2011)). This suggests using the locations of moulins derived from satellite imagery acquired at the end of the melt season as representative of moulins outside of lake basins and hydrofractured lakes. Lake hydrofracture events are, however, observed to result in

temporarily faster flow locally (Stevens et al., 2015; Tedesco et al., 2013a). In order for a model to capture these events, the specific location, timing, and volume of lakes will need to be incorporated into the model. This implies using observational records of lake drainages derived from satellite imagery as in Bougamont et al. (2014) to derive hydrofracture input to the ice-bed interface. Crevasses drain a significant proportion of water, most of which drains over the ice surface into crevasse fields rather than being generated locally. Since crevasse drainage is poorly understood, a Veronoi partition was used around the points where high input supraglacial rivers intersect crevasse fields. However, patterns of moulins are known to influence the development of the subglacial hydrological system (Banwell et al., 2016), and further work is required on understanding crevasse drainage. Since moulins and crevasses drain water in a continuous manner, with a relatively high spatial density, this suggests simply approximating input into each drainage pathway from its local catchment. The output of each catchment into the corresponding drainage pathway may be simplified to two output hydrographs, one for snow-covered and the other for bare-ice conditions. For internal catchments of crevasse fields routing can likely be neglected. This calculation need only be done once. Subsequently moulin input at each time step could be calculated at little cost based on total surface runoff in the catchment and the dominant surface cover in the catchment.

5.5.4 Implications

The success in the model in recreating features in the measured velocities provides validation for each model component, as well as their integration. The work supports integrating models of high complexity, incorporating a range of processes. Further model refinement and data acquisition should continue to improve the fit between modelled and measured velocities. A key uncertainty in the initialization process was the subglacial hydrology model run during winter, and the subsequent inversion for background basal parameters. Although the process introduced in this thesis cannot capture year on year changes, the practical value of the initialization process is implicitly validated through the subsequent fit to measured velocities. The model results also support the hypothesis that the margin of the GrIS is controlled by subglacial hydrology in a manner similar to alpine glaciers.

The timing of velocity variations are controlled by surface input and modulated by subglacial hydrology. At high elevations where channelization is not observed, variations in model velocities track modelled surface runoff closely. GPS velocities, however, do not show the same fidelity to the time series of ablation from automatic weather stations, which are qualitatively more variable than modelled runoff. This suggests dampening of the variability of surface input by the supraglacial and subglacial hydrology, and that variability in daily

ablation rates are not simply correlated to faster flow. A quantitative analysis of the two time series may provide better insight into the relationship between surface melt and ice velocities. However ice velocities are driven by the cumulative melt over a larger upstream area from the point of measurement, which may not be well represented by the variability of melt at a single point. At lower elevations, channelization is important in modulating the impact of surface water on ice velocities. The low modelled and observed velocities closer to the ice-margin imply a consistently high effective pressure at the GPS sites, due to impact of channelization on water pressures and water routing.

Modelling predicts that average ice velocities over the melt season will increase with melt season intensity. A similar correlation was observed in GPS records over the upper ablation zone of the Russell Glacier region by (van de Wal et al., 2015), but not in GPS records at North Lake, Western Greenland by Stevens et al. (2016). This implies that more intense melt seasons will result in a higher ice flux towards the margin during the summer. Whether this would be offset by decreased ice flux during the winter is unresolved by the model.

Channelization is observed to develop more extensively and further inland as melt intensity increases. This trend is observed in the three modelled melt seasons and continues into the two future melt scenarios. This suggest that the subglacial hydrological system will continue to drain surface meltwater input in a similar manner as melt intensity increases beyond 2012 levels. Since channelization is attributed to a slowdown in mid-late summer (Tedstone et al., 2015; van de Wal et al., 2015), and postulated to result in slowdown in the subsequent winter and spring (Sole et al., 2013; Tedstone et al., 2015; van de Wal et al., 2015), model results suggest increasing summer melt intensity should lead to a more spatially extensive annual velocity slowdown. The slowdown may also become more pronounced in the future as the channelized system is predicted to drain an increased proportion of water.

Interpreting the model velocity output from the future melt scenarios is difficult. As melt season intensity increases, the validity of the initialization and calibration parameters becomes more uncertain. Further, the model has bias towards capturing short-term speedup events, rather than prolonged slowdowns due to model velocities remaining near or above their winter values. The modelled velocities show higher variability, and a significant increase in the magnitude of short-term speedup events. However, quantifying whether these will be offset by a corresponding late summer slowdown or by a winter slowdown is beyond the capability of the current model. Model output can be interpreted to suggest that a late summer velocity slowdown offsetting early summer speedup is less likely at higher elevations.

5.6 Conclusions

In this chapter, multiple models are coordinated to predict summer ice velocities at the southwest margin of GrIS from topographic and climatic input data. These models represent the main components of the ice sheet system: supraglacial hydrology, subglacial hydrology, and ice flow. The key component of the simulations presented in this chapter is a coupled hydrology-ice flow model. This integrated model is initialized using a workflow incorporating the adjoint ice flow model (Chapter 4), and is forced during the simulations using surface input from a surface hydrology model (Chapter 3). Calibration of the integrated model takes advantage of GPS velocities from two summer melt seasons: 2009 and 2011. The model validation on 2012 GPS data reproduces measured ice velocities to a similar degree as in 2009 and 2011. To a first order, the magnitude and timing of the measured velocities are replicated in modelled velocities at multiple sites.

The success of the multicomponent modeling to recreate summer velocities reflects on the integrity of each individual model and dataset. This work should encourage further model coupling as it suggests that individual components and datasets are robust. However, limitations of the multicomponent model are evident in the model output, particularly that the model velocity does not significantly drop below its initialized winter value. Additional data and theory will be necessary to address these issues. Together, the models also form a quantitative test of the hypothesis proposed by numerous authors (e.g Chandler et al., 2013; Colgan et al., 2011a; Cowton et al., 2013; Hewitt, 2013; Hoffman et al., 2011; Schoof, 2010; van de Wal et al., 2015) that the summer acceleration of the GrIS margin is controlled by the evolution of the subglacial hydrological system in a manner analogous to the seasonal speedup of alpine glaciers. The key result of this chapter is quantitative support in favour of this hypothesis.

Chapter 6

Conclusions

6.1 Summary of Thesis

This thesis investigates the impact of surface melt on the subglacial hydrology and ice dynamics of land-terminating sectors of the GrIS. This was approached through numerical modelling, with the ultimate aim of trying to recreate GPS measured ice velocities using a model forced by climatic and topographic data inputs. Through the process, our understanding of each of the main components of the ice sheet system is developed. Three new/updated models are presented: a supraglacial hydrology model, an ice flow model, and an adjoint model. The models attempt to incorporate as much relevant complexity as possible, and applications of the models rely heavily on available datasets, both as model input and for model validation.

The surface hydrology model is run in the Paakitsoq area and the Russell Glacier area. The model results provide a partitioning of surface runoff between different meltwater drainage pathways. This partitioning depends on the study site. The effects of the fast flowing Jakobshavn Isbrae south of the Paakitsoq region are evident in the higher proportion of meltwater draining into crevasses. Model runs in Paakitsoq show that melt partitioning varies inter-annually, and may be dependent on melt season intensity. However, the key output is a temporal and spatial map of meltwater input to the englacial system (and subglacial system under suitable assumptions). This time series is essential for modelling ice velocities.

A new ice sheet model and inversion code are developed. The ice sheet model is based on a numerically efficient approximation that accounts for vertical gradients in horizontal velocities implicitly. This allows basal velocities to be calculated, which provide a key feedback to the subglacial system, while remaining sufficiently efficient to be run at a high spatial and temporal resolution. Developing the ice sheet model necessitated a counterpart

adjoint model. Proper initialization of the model parameters and state is a key challenge for applying a linked hydrology/ice dynamics model to a real world domain. This is addressed by proposing a new initialization workflow. The workflow is novel in that modelled subglacial effective pressures are used to constrain inversions of basal drag, which are performed using non-linear sliding laws explicitly depending on water pressure. Although the subglacial hydrology model output is in line with summer rather than winter radar measurements, the usefulness of the workflow is demonstrated.

A multicomponent model comprised of a supraglacial, subglacial and ice flow components is applied to the Russell glacier area. The model is calibrated and validated against GPS velocity measurements. To a first order, features observed in the measured velocities are reproduced by the model at multiple sites. Limitations of the model are evident in output near the ice margin, and during periods when the measured velocity drops below its winter mean. The key outcome of this modelling is quantitative support for the hypothesis that summer acceleration at the margin of the GrIS is driven by subglacial-hydrology in a manner similar to alpine glaciers. The calibrated parameters also provide a starting point for future simulations. Modelling the impact of surface melt on ice velocities in the future is beyond the current capability of the model. However, the development of the subglacial system under future melt scenarios follows similar patterns as present years, suggesting that current trends are likely to continue.

6.2 Directions for Future Work

Both programming time and computational resources were both considered in the model development process. Two important points were ensuring that the models were deployed in the timeframe of the thesis, and efficient enough to run a suite of calibration and sensitivity experiments. An outcome of this thesis should be to encourage a mature ice-flow project such as Elmer, CISM, or ISSM to integrate an advanced hydrology model into their framework. Advantages of these projects include: computational efficiency of low-level languages, standardization, and longevity. A more computationally efficient question could address the impacts of model resolution and formulation of the ice-flow model. To allow for sufficient calibration of the model, the application of the integrated model in the Russell Glacier area was run at 1000 m resolution. The limiting dataset in the application is the bed topography, which has a reported resolution is 400 m. An important question to address is what the impact of coarsening the bed topography is on water routing, and more generally, at what resolution does bed topography have to be known for accurate water routing. It is also important to determine the minimum order of ice-flow model to use. The longevity of mature projects

is suited to understanding the role of data quality. Already, a higher resolution version of RACMO2 output is available. A standardized model could be routinely rerun as inputs are improved.

Water input to the subglacial hydrological system is a key driver of the evolution of the system. The predicted model velocities may be altered under different assumptions of surface water routing, and by using an alternative set of meltwater drainage pathways. Different subglacial hydrology models should be tested with the same surface input to elucidate differences in model formulation. A stable, user-friendly supraglacial hydrology model would be of benefit for such model inter-comparison.

Model results suggests two avenues for theoretical work to improve results. The first is parameterizing the ice-bed coupling. In general, the form of the sliding law and its parameters are still an open question (Hewitt, 2013). Constraining these would be beneficial for model calibration. The second main theoretical improvement concerns the observation that the model velocities never significantly drop below their winter mean. Hoffman et al. (2016) report that incorporating a weakly connected distributed system is important for modelling the summer slowdown. However, further effort could improve their formulation of such a system, reducing the number of parameterizations and unknown parameters. The presence of a weakly connected distributed system would also need to be considered in the initialization procedure. These issues must be resolved to model the relationship of surface melt and mean annual velocity, and to quantitatively predict the evolution of the GrIS margin.

Application of the model to a land-terminating sector of the GrIS isolated the impact of the hydrological system on ice velocities. However, the role of hydrology on marine-terminating sectors remains understudied. Subglacial hydrology can be expected to impact the ice dynamics of these sectors by modifying basal drag, as well as impact the calving rate via proglacial meltwater plumes (e.g. Slater et al., 2015). Understanding subglacial hydrology in this more complex environment is an important next step.

This thesis introduced a workflow for incorporating modelled subglacial effective pressure into inversions for basal drag using sliding laws explicitly dependent on effective pressure. The aim of this work, however, was operational. Future work could attempt to interpret the inversions rigorously. This would require careful consideration of the inversion process and the length scales of subglacial hydrology, as there is a limit of the wavelength of basal drag transmitted to the surface (Joughin et al., 2004; Martin and Monnier, 2014).

Ultimately, models are constrained and tested against data. Future field campaigns should continue to deploy spatial arrays of GPS stations, and effort should continue on generating velocity maps from remote sensing products.

6.3 Concluding Remarks

Mass loss from the GrIS is accelerating, driven by dynamic losses from marine terminating glaciers and changes in surface mass balance. Since nearly all surface runoff drains from the ice sheet via the subglacial system, increasing surface runoff may lead to dynamic changes in the GrIS by modulating basal drag. Constraining future contributions of the GrIS to sea level rise depends on understanding the impact of increasing surface melt on ice velocities.

Numerous observations show a complex relationship between surface runoff and ice velocities at the margin of the GrIS. These observations have been interpreted using theory developed on alpine glaciers, which attributes seasonal acceleration to changes in the subglacial hydrological system. The numerical modelling in this thesis affirms this approach for explaining the broad pattern of early season speedup and late season slowdown. However, neither the current conceptual model of the ice sheet margin nor the numerical model implemented in this thesis clearly elucidates the observed decadal timescale slowdown in ice velocities nor the inconsistent relationship between melt season intensity and ice velocities on annual time scales.

The multicomponent model applied here is a modest step towards modelling observed ice velocities during the summer melt season. An attempt has been made to be clear about the aspects which have proven successful, and how the model can be improved. Although significant issues are apparent, many of the model components and datasets used have proven to be robust. Hopefully this work inspires, and points the direction for, further work modelling the GrIS as an integrated system.

References

- Albrecht, T. and Levermann, A. (2014). Fracture-induced softening for large-scale ice dynamics. *The Cryosphere*, 8(2):587–605.
- Alley, R. B., Clark, P. U., Huybrechts, P., and Joughin, I. (2005). Ice-sheet and sea-level changes. *Science (New York, N.Y.)*, 310(5747):456–60.
- Andrews, L. C., Catania, G. A., Hoffman, M. J., Gulley, J. D., Lüthi, M. P., Ryser, C., Hawley, R. L., and Neumann, T. A. (2014). Direct observations of evolving subglacial drainage beneath the Greenland Ice Sheet. *Nature*, 514(7520):80–83.
- Arnold, N., Richards, K., Willis, I., and Sharp, M. (1998). Initial results from a distributed , physically based model of glacier hydrology. *Hydrological Processes*, 12(February 1997):191–219.
- Arnold, N. and Sharp, M. (2002). Flow variability in the scandinavian ice sheet: modelling the coupling between ice sheet flow and hydrology. *Quaternary Science Reviews*, 21(4):485–502.
- Arnold, N. S., Banwell, A. F., and Willis, I. C. (2014). High-resolution modelling of the seasonal evolution of surface water storage on the greenland ice sheet. *The Cryosphere*, 7(8):1149–1160.
- Arthern, R. J., Hindmarsh, R. C. A., and Williams, C. R. (2015). Flow speed within the Antarctic ice sheet and its controls inferred from satellite observations. *Journal of Geophysical Research: Earth Surface*, 120(7):1171–1188.
- Banwell, A., Hewitt, I., Willis, I., and Arnold, N. (2016). Moulin density controls drainage development beneath the Greenland Ice Sheet. *Journal of Geophysical Research: Earth Surface*.
- Banwell, A. F., Arnold, N. S., Willis, I. C., Tedesco, M., and Ahlstrøm, A. P. (2012a). Modeling supraglacial water routing and lake filling on the Greenland Ice Sheet. *Journal of Geophysical Research*, 117(F4):F04012.
- Banwell, A. F., Willis, I. C., and Arnold, N. S. (2013). Modeling subglacial water routing at Paakitsoq, W Greenland. *Journal of Geophysical Research: Earth Surface*, 118(3):1282–1295.
- Banwell, A. F., Willis, I. C., Arnold, N. S., Messerli, A., Rye, C. J., Tedesco, M., and Ahlstrøm, A. P. (2012b). Calibration and evaluation of a high-resolution surface mass-balance model for Paakitsoq, West Greenland. *Journal of Glaciology*, 58(212):1047–1062.

- Bartholomew, I., Nienow, P., Mair, D., Hubbard, A., King, M. A., and Sole, A. (2010). Seasonal evolution of subglacial drainage and acceleration in a Greenland outlet glacier. *Nature Geoscience*, 3(6):408–411.
- Bartholomew, I., Nienow, P., Sole, A., Mair, D., Cowton, T., King, M., and Palmer, S. (2011a). Seasonal variations in Greenland Ice Sheet motion: Inland extent and behaviour at higher elevations. *Earth and Planetary Science Letters*, 307(3-4):271–278.
- Bartholomew, I., Nienow, P., Sole, A., Mair, D., Cowton, T., Palmer, S., and Wadham, J. (2011b). Supraglacial forcing of subglacial drainage in the ablation zone of the Greenland ice sheet. *Geophysical Research Letters*, 38(8):n/a–n/a.
- Blatter, H. (1995). Velocity and stress fields in grounded glaciers: a simple algorithm for including deviatoric stress gradients. *Journal of Glaciology*, 41:333–344.
- Bougamont, M., Christoffersen, P., A L, H., Fitzpatrick, A., Doyle, S., and Carter, S. (2014). Sensitive response of the greenland ice sheet to surface melt drainage over a soft bed. *Nature communications*, 5.
- Box, J. E. and Ski, K. (2007). Remote sounding of Greenland supraglacial melt lakes: implications for subglacial hydraulics. *Journal of Glaciology*, 53(181):257–265.
- Budd, W., Keage, P., and Blundy, N. (1979). Empirical studies of ice sliding. *Journal of glaciology*, 23(89):157–170.
- Bueler, E. and Brown, J. (2009). Shallow shelf approximation as a "sliding law" in a thermo-mechanically coupled ice sheet model. *Journal of Geophysical Research*, 114(F3):F03008.
- Catania, G., Neumann, T., and Price, S. (2008). Characterizing englacial drainage in the ablation zone of the Greenland ice sheet. *Journal of Glaciology*, 54(187):567–578.
- Catania, G. A. and Neumann, T. A. (2010). Persistent englacial drainage features in the Greenland Ice Sheet. *Geophysical Research Letters*, 37(2):n/a–n/a.
- Chandler, D. M., Wadham, J. L., Lis, G. P., Cowton, T., Sole, A., Bartholomew, I., Telling, J., Nienow, P., Bagshaw, E. B., Mair, D., Vinen, S., and Hubbard, A. (2013). Evolution of the subglacial drainage system beneath the Greenland Ice Sheet revealed by tracers. *Nature Geoscience*, 6(3):195–198.
- Chu, V. W. (2013). Greenland ice sheet hydrology: A review. *Progress in Physical Geography*, 38(1):19–54.
- Chu, W., Schroeder, D. M., Seroussi, H., Creyts, T. T., Palmer, S. J., and Bell, R. E. (2016). Extensive winter subglacial water storage beneath the Greenland Ice Sheet. *Geophysical Research Letters*, pages 484–492.
- Clason, C., Mair, D. W., Burgess, D. O., and Nienow, P. W. (2012). Modelling the delivery of supraglacial meltwater to the ice/bed interface: application to southwest Devon Ice Cap, Nunavut, Canada. *Journal of Glaciology*, 58(208):361–374.

- Clason, C. C., Mair, D. W. F., Nienow, P. W., Bartholomew, I. D., Sole, A., Palmer, S., and Schwanghart, W. (2015). Modelling the transfer of supraglacial meltwater to the bed of leverett glacier, southwest greenland. *The Cryosphere*, 9(1):123–138.
- Colgan, W., Rajaram, H., Anderson, R., Steffen, K., Phillips, T., Joughin, I., Zwally, H. J., and Abdalati, W. (2011a). The annual glaciohydrology cycle in the ablation zone of the Greenland ice sheet: Part 1. Hydrology model. *Journal of Glaciology*, 57(204):697–709.
- Colgan, W., Rajaram, H., Anderson, R., Steffen, K., Zwally, J., Phillips, T., and Abdalati, W. (2012). The annual glaciohydrology cycle in the ablation zone of the Greenland ice sheet: Part 2. Observed and modeled ice flow. *Journal of Glaciology*, 58(207):51–64.
- Colgan, W., Steffen, K., McLamb, W. S., Abdalati, W., Rajaram, H., Motyka, R., Phillips, T., and Anderson, R. (2011b). An increase in crevasse extent, West Greenland: Hydrologic implications. *Geophysical Research Letters*, 38(18).
- Cowton, T., Nienow, P., Sole, A., Wadham, J., Lis, G., Bartholomew, I., Mair, D., and Chandler, D. (2013). Evolution of drainage system morphology at a land-terminating Greenlandic outlet glacier. *Journal of Geophysical Research: Earth Surface*, 118(1):29–41.
- Creys, T. T. and Schoof, C. G. (2009). Drainage through subglacial water sheets. *Journal of Geophysical Research*, 114(F4):F04008.
- Cuffey, K. and Paterson, W. (2010). *The physics of glaciers*. Academic Press.
- Das, S. B., Joughin, I., Behn, M. D., Howat, I. M., King, M. A., Lizarralde, D., and Bhatia, M. P. (2008). Fracture propagation to the base of the Greenland Ice Sheet during supraglacial lake drainage. *Science (New York, N.Y.)*, 320(5877):778–81.
- de Fleurian, B., Morlighem, M., Seroussi, H., Rignot, E., van den Broeke, M. R., Munneke, P. K., Mouginot, J., Smeets, P. C. J. P., and Tedstone, A. J. (2016). A modeling study of the effect of runoff variability on the effective pressure beneath Russell Glacier, West Greenland. *Journal of Geophysical Research: Earth Surface*.
- Doyle, S. H., Hubbard, A., Fitzpatrick, A. A. W., van As, D., Mikkelsen, A. B., Pettersson, R., and Hubbard, B. (2014). Persistent flow acceleration within the interior of the greenland ice sheet. *Geophysical Research Letters*, 41(3):899–905. 2013GL058933.
- Doyle, S. H., Hubbard, A. L., Dow, C. F., Jones, G. A., Fitzpatrick, A., Gusmeroli, A., Kulesa, B., Lindback, K., Pettersson, R., and Box, J. E. (2013). Ice tectonic deformation during the rapid in situ drainage of a supraglacial lake on the Greenland Ice Sheet. *The Cryosphere*, 7(1):129–140.
- Echelmeyer, K., Clarke, T., and Harrison, W. (1991). Surficial glaciology of Jakobshavns Isbræ, West Greenland: Part I. Surface morphology. *J. Glaciol*, 37(127):368–382.
- Enderlin, E. M., Howat, I. M., Jeong, S., Noh, M.-J., van Angelen, J. H., and van den Broeke, M. R. (2014). An improved mass budget for the Greenland ice sheet. *Geophysical Research Letters*, 41(3):866–872.

- Errico, R. M. (1997). What is an Adjoint? *Bulletin of the American Meteorological Society*, 78(11):2577–2591.
- Fahnestock, M., Scambos, T., Moon, T., Gardner, A., Haran, T., and Klinger, M. (2016). Rapid large-area mapping of ice flow using Landsat 8. *Remote Sensing of Environment*, 185:84–94.
- Fettweis, X., Hanna, E., Lang, C., Belleflamme, a., Erpicum, M., and Gallée, H. (2013). Brief communication: Important role of the mid-tropospheric atmospheric circulation in the recent surface melt increase over the Greenland ice sheet. *The Cryosphere*, 7(1):241–248.
- Fettweis, X., Tedesco, M., van den Broeke, M., and Ettema, J. (2011). Melting trends over the Greenland ice sheet (1958-2009) from spaceborne microwave data and regional climate models. *The Cryosphere*, 5(2):359–375.
- Fitzpatrick, A. A. W., A., Hubbard, A., Joughin, I., Quincey, D. J., Van As, D., Mikkelsen, A. P., Doyle, S. H., Hasholt, B., and Jones, G. a. (2013). Ice flow dynamics and surface meltwater flux at a land-terminating sector of the Greenland ice sheet. *Journal of Glaciology*, 59(216):687–696.
- Fitzpatrick, A. A. W., Hubbard, A. L., Box, J. E., Quincey, D. J., van As, D., Mikkelsen, A. P. B., Doyle, S. H., Dow, C. F., Hasholt, B., and Jones, G. A. (2014). A decade (2002-2012) of supraglacial lake volume estimates across russell glacier, west greenland. *The Cryosphere*, 8(1):107–121.
- Flowers, G. E. (2015). Modelling water flow under glaciers and ice sheets. *Proceedings of the Royal Society of London A: Mathematical, Physical and Engineering Sciences*, 471(2176).
- Flowers, G. E. and Clarke, G. K. C. (2002). A multicomponent coupled model of glacier hydrology 2. Application to Trapridge Glacier, Yukon, Canada. *Journal of Geophysical Research*, 107(B11):2288.
- Forster, R. R., Box, J. E., van den Broeke, M. R., Miège, C., Burgess, E. W., van Angelen, J. H., Lenaerts, J. T. M., Koenig, L. S., Paden, J., Lewis, C., Gogineni, S. P., Leuschen, C., and McConnell, J. R. (2013). Extensive liquid meltwater storage in firn within the Greenland ice sheet. *Nature Geoscience*, 7(2):95–98.
- Fountain, A., Jacobel, R., Schlichting, R., and Jansson, P. (2005). Fractures as the main pathways of water flow in temperate glaciers. *Nature*, 433(7026):618–621.
- Fountain, A. G. and Walder, J. S. (1998). Water flow through temperate glaciers. *Reviews of Geophysics*, 36(3):299–328.
- Gagliardini, O., Cohen, D., Raback, P., and Zwinger, T. (2007). Finite-element modeling of subglacial cavities and related friction law. *Journal of Geophysical Research: Earth Surface*, 112(F2):n/a–n/a. F02027.
- Gagliardini, O. and Zwinger, T. (2008). The ismip-hom benchmark experiments performed using the finite-element code elmer. *The Cryosphere*, 2(1):67–76.

- Giering, R., Kaminski, T., and Slawig, T. (2005). Generating efficient derivative code with taf adjoint and tangent linear euler flow around an airfoil. *Future Gener. Comput. Syst.*, 21(8):1345–1355.
- Goldberg, D. N. (2011). A variationally derived, depth-integrated approximation to a higher-order glaciological flow model. *Journal of Glaciology*, 57(201):157–170.
- Goldberg, D. N. and Heimbach, P. (2013). Parameter and state estimation with a time-dependent adjoint marine ice sheet model. *The Cryosphere*, 7(6):1659–1678.
- Goldberg, D. N., Narayanan, S. H. K., Hascoet, L., and Utke, J. (2016). An optimized treatment for algorithmic differentiation of an important glaciological fixed-point problem. *Geoscientific Model Development*, 9(5):1891–1904.
- Goldsby, D. L. and Kohlstedt, D. L. (2001). Superplastic Deformation of ice: Experimental Observations. *Journal of Geophysical Research*, 106(B6):11017–11030.
- Greve, R. and Blatter, H. (2009). *Dynamics of ice sheets and glaciers*. Springer Science & Business Media.
- Griewank, A. and Walther, A. (2008). *Evaluating derivatives: principles and techniques of algorithmic differentiation*. SIAM.
- Hanna, E., Navarro, F. J., Pattyn, F., Domingues, C. M., Fettweis, X., Ivins, E. R., Nicholls, R. J., Ritz, C., Smith, B., Tulaczyk, S., Whitehouse, P. L., and Zwally, H. J. (2013). Ice-sheet mass balance and climate change. *Nature*, 498(7452):51–59.
- Harper, J., Humphrey, N., Pfeffer, W. T., Brown, J., and Fettweis, X. (2012). Greenland ice-sheet contribution to sea-level rise buffered by meltwater storage in firn. *Nature*, 491(7423):240–243.
- Harrington, J. a., Humphrey, N. F., and Harper, J. T. (2015). Temperature distribution and thermal anomalies along a flowline of the Greenland Ice Sheet. *Annals of Glaciology*, 56(70):98–104.
- Hascoet, L. and Pascual, V. (2004). Tapenade 2.1 users guide. <http://www-tapenade.inria.fr:8080/tapenade/index.jsp>.
- Heimbach, P. and Bugnion, V. (2009). Greenland ice-sheet volume sensitivity to basal, surface and initial conditions derived from an adjoint model. *Annals of Glaciology*, 50(52):67–80.
- Hewitt, I. (2013). Seasonal changes in ice sheet motion due to melt water lubrication. *Earth and Planetary Science Letters*, 371-372:16–25.
- Hindmarsh, R. C. A. (2004). A numerical comparison of approximations to the Stokes equations used in ice sheet and glacier modeling. *Journal of Geophysical Research*, 109(F):1012.
- Hoffman, M. and Price, S. (2014). Feedbacks between coupled subglacial hydrology and glacier dynamics. *Journal of Geophysical Research: Earth Surface*, 119(3):414–436.

- Hoffman, M. J., Andrews, L. C., Price, S. A., Catania, G. A., Neumann, T. A., Luethi, M. P., Gulley, J., Ryser, C., Hawley, R. L., and Morriss, B. F. (2016). Greenland subglacial drainage evolution regulated by weakly-connected regions of the bed. *Nature Communications*.
- Hoffman, M. J., Catania, G. A., Neumann, T. A., Andrews, L. C., and Rumrill, J. A. (2011). Links between acceleration, melting, and supraglacial lake drainage of the western Greenland Ice Sheet. *Journal of Geophysical Research*, 116(F4):F04035.
- Howat, I., Negrete, A., and Smith, B. (2015). Measures greenland ice mapping project (gimp) digital elevation model, version 1. 90m resolution. Boulder, Colorado USA. NASA National Snow and Ice Data Center Distributed Active Archive Center.
- Howat, I. M., de la Peña, S., van Angelen, J. H., Lenaerts, J. T. M., and van den Broeke, M. R. (2013). Brief Communication: Expansion of meltwater lakes on the Greenland Ice Sheet. *The Cryosphere*, 7(1):201–204.
- Hutter, K. (1983). *Theoretical glaciology : material science of ice and the mechanics of glaciers and ice sheets*. Reidel Terra Scientific Pub. Co. Sold and distributed in the U.S.A. and Canada by Kluwer Academic Publishers, Dordrecht Boston Tokyo, Japan Hingham, MA.
- Irvine-Fynn, T. D. L., Hodson, A. J., Moorman, B. J., Vatne, G., and Hubbard, A. L. (2011). Polythermal Glacier Hydrology: A Review. *Reviews of Geophysics*, 49(4):RG4002.
- Jarosch, A. H. and Gudmundsson, M. T. (2012). A numerical model for meltwater channel evolution in glaciers. *The Cryosphere*, 6(2):493–503.
- Johansson, A., Jansson, P., and Brown, I. (2013). Spatial and temporal variations in lakes on the Greenland Ice Sheet. *Journal of Hydrology*, 476:314–320.
- Joughin, I., Das, S. B., Flowers, G. E., Behn, M. D., Alley, R. B., King, M. a., Smith, B. E., Bamber, J. L., van den Broeke, M. R., and van Angelen, J. H. (2013). Influence of ice-sheet geometry and supraglacial lakes on seasonal ice-flow variability. *The Cryosphere*, 7(4):1185–1192.
- Joughin, I., Das, S. B., King, M. A., Smith, B. E., Howat, I. M., and Moon, T. (2008). Seasonal speedup along the western flank of the Greenland Ice Sheet. *Science (New York, N.Y.)*, 320(5877):781–3.
- Joughin, I., MacAyeal, D. R., and Tulaczyk, S. (2004). Basal shear stress of the Ross ice streams from control method inversions. *Journal of Geophysical Research B: Solid Earth*, 109(9):1–20.
- Joughin, I., Smith, B. E., Howat, I. M., Scambos, T., and Moon, T. (2010a). Greenland flow variability from ice-sheet-wide velocity mapping. *Journal of Glaciology*, 56(197):415–430.
- Joughin, I., Smith, B. E., Howat, I. M., Scambos, T., and Moon, T. (2010b). MEaSUREs Greenland Ice Velocity Map from InSAR Data. Boulder, Colorado, USA: NASA DAAC at the National Snow and Ice Data Center.

- Kamb, B. (1987). Glacier surge mechanism based on linked cavity configuration of the basal water conduit system. *Journal of Geophysical Research: Solid Earth*, 92(B9):9083–9100.
- Kingslake, J. (2013). *Modelling Ice-Dammed Lake Drainage*. PhD thesis, University of Sheffield.
- Kingslake, J., Ng, F., and Sole, A. (2015). Modelling channelized surface drainage of supraglacial lakes. *Journal of Glaciology*, 61(225):185–199.
- Koziol, C., Arnold, N., Pope, A., and Colgan, W. (2017). Quantifying supraglacial meltwater pathways in the paakitsoq region, west greenland. *Journal of Glaciology*, pages 1–13.
- Krawczynski, M. J., Behn, M. D., Das, S. B., and Joughin, I. (2009). Constraints on the lake volume required for hydro-fracture through ice sheets. *Geophysical Research Letters*, 36(10):L10501.
- Leeson, A. A., Shepherd, A., Palmer, S., Sundal, A., and Fettweis, X. (2012). Simulating the growth of supraglacial lakes at the western margin of the Greenland ice sheet. *The Cryosphere*, 6(5):1077–1086.
- Leeson, A. A., Shepherd, A., Sundal, A. V., Johansson, A. M., Selmes, N., Briggs, K., Hogg, A. E., and Fettweis, X. (2013). A comparison of supraglacial lake observations derived from MODIS imagery at the western margin of the Greenland ice sheet. *Journal of Glaciology*, 59(218):1179–1188.
- Liang, Y.-L., Colgan, W., Lv, Q., Steffen, K., Abdalati, W., Stroeve, J., Gallaher, D., and Bayou, N. (2012). A decadal investigation of supraglacial lakes in West Greenland using a fully automatic detection and tracking algorithm. *Remote Sensing of Environment*, 123:127–138.
- Lüthi, M. P., Ryser, C., Andrews, L. C., Catania, G. a., Funk, M., Hawley, R. L., Hoffman, M. J., and Neumann, T. a. (2015). Heat sources within the Greenland Ice Sheet: dissipation, temperate paleo-firn and cryo-hydrologic warming. *The Cryosphere*, 9(1):245–253.
- Luthje, M., Pedersen, L. T., Reeh, N., and Greuell, W. (2006). Modelling the evolution of supraglacial lakes on the West Greenland ice-sheet margin. *Journal of Glaciology*, 52(179):608–618.
- MacAyeal, D. (1993). A tutorial on the use of control methods in ice sheet modeling. *J. Glaciol*, 39(131):91–98.
- MacAyeal, D. R. (1989). Large-scale ice flow over a viscous basal sediment: Theory and application to ice stream b, antarctica. *Journal of Geophysical Research: Solid Earth*, 94(B4):4071–4087.
- Martin, N. and Monnier, J. (2014). Adjoint accuracy for the full stokes ice flow model: limits to the transmission of basal friction variability to the surface. *The Cryosphere*, 8(2):721–741.
- McGrath, D., Colgan, W., Steffen, K., Lauffenburger, P., and Balog, J. (2011). Assessing the summer water budget of a moulin basin in the Sermeq Avannarleq ablation region, Greenland ice sheet. *Journal of Glaciology*, 57(205):954–964.

- McMillan, M., Nienow, P., Shepherd, A., Benham, T., and Sole, A. (2007). Seasonal evolution of supra-glacial lakes on the Greenland Ice Sheet. *Earth and Planetary Science Letters*, 262(3-4):484–492.
- Meierbachtol, T., Harper, J., and Humphrey, N. (2013). Basal drainage system response to increasing surface melt on the Greenland Ice Sheet. *Science*, 341(6147):777–779.
- Minchew, B., Simons, M., Bjornsson, H., Palsson, F., Morlighem, M., Seroussi, H., Larour, E., and Hensley, S. (2016). Plastic bed beneath Hofsjokull ice cap, central Iceland, and the sensitivity of ice flow to surface meltwater flux. *Journal of Glaciology*, 62(231):147–158.
- Moon, T., Joughin, I., Smith, B., van den Broeke, M. R., van de Berg, W. J., Noel, B., and Usher, M. (2014). Distinct patterns of seasonal greenland glacier velocity. *Geophysical Research Letters*, 41(20):7209–7216.
- Morlighem, M., Rignot, E., Mouginot, J., Seroussi, H., and Larour, E. (2014). Deeply incised submarine glacial valleys beneath the Greenland ice sheet. *Nature Geoscience*, 7(6):418–422.
- Morlighem, M., Rignot, E., Mouginot, J., Seroussi, H., and Larour, E. (2015a). IceBridge BedMachine Greenland, Version 1, Thickness. Boulder, Colorado USA: NASA DAAC at the National Snow and Ice Data Center.
- Morlighem, M., Rignot, E., Mouginot, J., Seroussi, H., and Larour, E. (2015b). IceBridge BedMachine Greenland, Version 2, Thickness. Boulder, Colorado USA: NASA DAAC at the National Snow and Ice Data Center.
- Morlighem, M., Seroussi, H., Larour, E., and Rignot, E. (2013). Inversion of basal friction in Antarctica using exact and incomplete adjoints of a higher-order model. *Journal of Geophysical Research: Earth Surface*, 118(3):1746–1753.
- Morriss, B. F., Hawley, R. L., Chipman, J. W., Andrews, L. C., Catania, G. A., Hoffman, M. J., Lüthi, M. P., and Neumann, T. a. (2013). A ten-year record of supraglacial lake evolution and rapid drainage in West Greenland using an automated processing algorithm for multispectral imagery. *The Cryosphere*, 7(6):1869–1877.
- Noël, B., van de Berg, W. J., Lhermitte, S., Wouters, B., Machguth, H., Howat, I., Citterio, M., Moholdt, G., Lenaerts, J. T. M., and van den Broeke, M. R. (2017). A tipping point in refreezing accelerates mass loss of Greenland’s glaciers and ice caps. *Nature Communications*, 8(9296):14730.
- Noël, B., van de Berg, W. J., van Meijgaard, E., Kuipers Munneke, P., van de Wal, R. S. W., and van den Broeke, M. R. (2015). Summer snowfall on the greenland ice sheet: a study with the updated regional climate model racmo2.3. *The Cryosphere Discussions*, 9(1):1177–1208.
- Nye, J. (1952). The mechanics of glacier flow. *Journal of Glaciology*, 2:82–93.
- Pattyn, F. (2003). A new three-dimensional higher-order thermomechanical ice sheet model: Basic sensitivity, ice stream development, and ice flow across subglacial lakes. *Journal of Geophysical Research: Solid Earth*, 108(B8):n/a–n/a. 2382.

- Phillips, T., Leyk, S., Rajaram, H., Colgan, W., Abdalati, W., McGrath, D., and Steffen, K. (2011). Modeling moulin distribution on Sermeq Avannarleq glacier using ASTER and WorldView imagery and fuzzy set theory. *Remote Sensing of Environment*, 115(9):2292–2301.
- Phillips, T., Rajaram, H., Colgan, W., Steffen, K., and Abdalati, W. (2013). Evaluation of cryo-hydrologic warming as an explanation for increased ice velocities in the wet snow zone, Sermeq Avannarleq, West Greenland. *Journal of Geophysical Research: Earth Surface*, 118(3):1241–1256.
- Phillips, T., Rajaram, H., and Steffen, K. (2010). Cryo-hydrologic warming: A potential mechanism for rapid thermal response of ice sheets. *Geophysical Research Letters*, 37:L20503.
- Pimentel, S. and Flowers, G. E. (2010). A numerical study of hydrologically driven glacier dynamics and subglacial flooding. *Proceedings of the Royal Society of London A: Mathematical, Physical and Engineering Sciences*, 467(2126):537–558.
- Pimentel, S., Flowers, G. E., and Schoof, C. G. (2010). A hydrologically coupled higher-order flow-band model of ice dynamics with a Coulomb friction sliding law. *Journal of Geophysical Research*, 115(F4):F04023.
- Poinar, K., Joughin, I., Das, S. B., Behn, M. D., Lenaerts, J. T. M., and Broeke, M. R. (2015). Limits to future expansion of surface-melt-enhanced ice flow into the interior of western Greenland. *Geophysical Research Letters*, 42:1800–1807.
- Poinar, K., Joughin, I., Lenaerts, J. T. M., and Van Den Broeke, M. R. (2016). Englacial latent-heat transfer has limited influence on seaward ice flux in western Greenland. *Journal of Glaciology*, pages 1–16.
- Pritchard, H. D., Arthern, R. J., Vaughan, D. G., and Edwards, L. A. (2009). Extensive dynamic thinning on the margins of the Greenland and Antarctic ice sheets. *Nature*, 461(7266):971–5.
- Raymond, C. and Nolan, M. (2000). Drainage of a glacial lake through an ice spillway. *Proceedings of a workshop held at Seattle, Washington, USA*, 264.
- Rignot, E., Velicogna, I., van den Broeke, M. R., Monaghan, A., and Lenaerts, J. T. M. (2011). Acceleration of the contribution of the Greenland and Antarctic ice sheets to sea level rise. *Geophysical Research Letters*, 38(5):n/a–n/a.
- Ryser, C., Luthi, M. P., Andrews, L. C., Hoffman, M. J., Catania, G. A., Hawley, R. L., Neumann, T. A., and Kristensen, S. S. (2014). Sustained high basal motion of the Greenland ice sheet revealed by borehole deformation. *Journal of Glaciology*, 60(222):647–660.
- Schmidt, M. (2005). minfunc: unconstrained differentiable multivariate optimization in matlab. <http://www.cs.ubc.ca/~schmidtm/Software/minFunc.html>.
- Schoof, C. (2005). The effect of cavitation on glacier sliding. *Proceedings of the Royal Society A: Mathematical, Physical and Engineering Sciences*, 461(2055):609–627.

- Schoof, C. (2010). Ice-sheet acceleration driven by melt supply variability. *Nature*, 468(7325):803–6.
- Selmes, N., Murray, T., and James, T. D. (2011). Fast draining lakes on the Greenland ice sheet. *Geophysical Research Letters*, 38(15).
- Selmes, N., Murray, T., and James, T. D. (2013). Characterizing supraglacial lake drainage and freezing on the Greenland Ice Sheet. *The Cryosphere Discussions*, 7(1):475–505.
- Sharp, M., Richards, K., Willis, I., Arnold, N., Nienow, P., Lawson, W., and Tison, J. L. (1993). Geometry, bed topography and drainage structure of the Haut Glacier d’Arolla, Switzerland. *Earth surf. Process. Landforms*, 18(6):557–571.
- Shepherd, A., Hubbard, A., Nienow, P., King, M., McMillan, M., and Joughin, I. (2009). Greenland ice sheet motion coupled with daily melting in late summer. *Geophysical Research Letters*, 36(1):L01501.
- Shepherd, A., Ivins, E. R., A, G., Barletta, V. R., Bentley, M. J., Bettadpur, S., Briggs, K. H., Bromwich, D. H., Forsberg, R., Galin, N., Horwath, M., Jacobs, S., Joughin, I., King, M. A., Lenaerts, J. T. M., Li, J., Ligtenberg, S. R. M., Luckman, A., Luthcke, S. B., McMillan, M., Meister, R., Milne, G., Mouginot, J., Muir, A., Nicolas, J. P., Paden, J., Payne, A. J., Pritchard, H., Rignot, E., Rott, H., Sørensen, L. S., Scambos, T. A., Scheuchl, B., Schrama, E. J. O., Smith, B., Sundal, A. V., van Angelen, J. H., van de Berg, W. J., van den Broeke, M. R., Vaughan, D. G., Velicogna, I., Wahr, J., Whitehouse, P. L., Wingham, D. J., Yi, D., Young, D., and Zwally, H. J. (2012). A reconciled estimate of ice-sheet mass balance. *Science (New York, N.Y.)*, 338(6111):1183–9.
- Shoemaker, E. M. and Leung, H. K. N. (1987). Subglacial drainage for an ice sheet resting upon a layered deformable bed. *Journal of Geophysical Research: Solid Earth*, 92(B6):4935–4946.
- Shreve, R. (1972). The Movement of Water in Glaciers. *Journal of Glaciology*, 11(62).
- Slater, D. A., Nienow, P. W., Cowton, T. R., Goldberg, D. N., and Sole, A. J. (2015). Effect of near-terminus subglacial hydrology on tidewater glacier submarine melt rates. *Geophysical Research Letters*, 42(8):2861–2868. 2014GL062494.
- Smith, L. C., Chu, V. W., Yang, K., Gleason, C. J., Pitcher, L. H., Rennermalm, A. K., Legleiter, C. J., Behar, A. E., Overstreet, B. T., Moustafa, S. E., Tedesco, M., Forster, R. R., LeWinter, A. L., Finnegan, D. C., Sheng, Y., and Balog, J. (2015). Efficient meltwater drainage through supraglacial streams and rivers on the southwest Greenland ice sheet. *Proceedings of the National Academy of Sciences*, 2000:201413024.
- Sole, A., Nienow, P., Bartholomew, I., Mair, D., Cowton, T., Tedstone, A., and King, M. A. (2013). Winter motion mediates dynamic response of the Greenland Ice Sheet to warmer summers. *Geophysical Research Letters*, 40(15):3940–3944.
- Stevens, L. A., Behn, M. D., Das, S. B., Joughin, I., Noel, B. P. Y., van den Broeke, M. R., and Herring, T. (2016). Greenland ice sheet flow response to runoff variability. *Geophysical Research Letters*, 43(21):11,295–11,303. 2016GL070414.

- Stevens, L. a., Behn, M. D., McGuire, J. J., Das, S. B., Joughin, I., Herring, T., Shean, D. E., and King, M. a. (2015). Greenland supraglacial lake drainages triggered by hydrologically induced basal slip. *Nature*, 522(7554):73–76.
- Sundal, A., Shepherd, A., Nienow, P., Hanna, E., Palmer, S., and Huybrechts, P. (2009). Evolution of supra-glacial lakes across the Greenland Ice Sheet. *Remote Sensing of Environment*, 113(10):2164–2171.
- Sundal, A. V., Shepherd, A., Nienow, P., Hanna, E., Palmer, S., and Huybrechts, P. (2011). Melt-induced speed-up of Greenland ice sheet offset by efficient subglacial drainage. *Nature*, 469(7331):521–4.
- Tarboron, G. (1997). A new method for the determination of flow directions and upslope areas in grid digital elevation models. *Water Resources Research*, 33(2):309–319.
- Tedesco, M., Lüthje, M., Steffen, K., Steiner, N., Fettweis, X., Willis, I., Bayou, N., and Banwell, A. (2012). Measurement and modeling of ablation of the bottom of supraglacial lakes in western Greenland. *Geophysical Research Letters*, 39(2):n/a–n/a.
- Tedesco, M. and Steiner, N. (2011). In-situ multispectral and bathymetric measurements over a supraglacial lake in western Greenland using a remotely controlled watercraft. *The Cryosphere*, 5(2):445–452.
- Tedesco, M., Willis, I. C., Hoffman, M. J., Banwell, A. F., Alexander, P., and Arnold, N. S. (2013a). Ice dynamic response to two modes of surface lake drainage on the Greenland ice sheet. *Environmental Research Letters*, 8(3):034007.
- Tedesco, M., Willis, I. C., Hoffman, M. J., Banwell, A. F., Alexander, P., and Arnold, N. S. (2013b). Ice dynamic response to two modes of surface lake drainage on the Greenland ice sheet. *Environmental Research Letters*, 8(3):034007.
- Tedstone, A. and Nienow, P. (2017). Ice motion measurements, south-west greenland ice sheet. <https://data.bas.ac.uk/metadata.php?id=GB/NERC/BAS/PDC/00841>. NERC, Polar Data Centre.
- Tedstone, A. J., Nienow, P. W., Gourmelen, N., Dehecq, A., Goldberg, D., and Hanna, E. (2015). Decadal slowdown of a land-terminating sector of the Greenland Ice Sheet despite warming. *Nature*, 526(7575):692–695.
- Thomsen, H. H. (1988). Mapping and modelling of glacier drainage in the paakitsoq basin, central west greenland. *Greenland Geological Survey Report*, 140:114–117.
- van de Wal, R. S. W., Boot, W., van den Broeke, M. R., Smeets, C. J. P. P., Reijmer, C. H., Donker, J. J. A., and Oerlemans, J. (2008). Large and rapid melt-induced velocity changes in the ablation zone of the Greenland Ice Sheet. *Science (New York, N.Y.)*, 321(5885):111–3.
- van de Wal, R. S. W., Smeets, C. J. P. P., Boot, W., Stoffelen, M., Van Kampen, R., Doyle, S. H., Wilhelms, F., Van Den Broeke, M. R., Reijmer, C. H., Oerlemans, J., and Hubbard, A. (2015). Self-regulation of ice flow varies across the ablation area in south-west Greenland. *Cryosphere*, 9(2):603–611.

- van den Broeke, M., Bamber, J., Ettema, J., Rignot, E., Schrama, E., van de Berg, W. J., van Meijgaard, E., Velicogna, I., and Wouters, B. (2009). Partitioning recent Greenland mass loss. *Science (New York, N.Y.)*, 326(5955):984–6.
- Van der Veen, C. J. (1998). Fracture mechanics approach to penetration of surface crevasses on glaciers. *Cold Regions Science and Technology*, 27(1):31–47.
- van der Veen, C. J. (2007). Fracture propagation as means of rapidly transferring surface meltwater to the base of glaciers. *Geophysical Research Letters*, 34(1):L01501.
- Van Der Veen, C. J., Plummer, J. C., and Stearns, L. A. (2011). Controls on the recent speed-up of Jakobshavn Isbr??, West Greenland. *Journal of Glaciology*, 57(204):770–782.
- Vaughan, D. (1993). Relating the occurrence of crevasses to surface strain rates. *Journal of Glaciology*, 39(132):255–266.
- Vaughan, D., Comiso, J., Allison, I., Carrasco, J., Kaser, G., Kwok, R., Mote, P., Murray, T., Paul, F., Ren, J., Rignot, E., Solomina, O., Steffen, K., and Zhang, T. (2013). *Observations: Cryosphere*, book section 4, page 317–382. Cambridge University Press, Cambridge, United Kingdom and New York, NY, USA.
- Walder, J. S. (1986). Hydraulics of subglacial cavities. *J. Glaciol*, 32(112):439–445.
- Weertman, J. (1972). General theory of water flow at the base of a glacier or ice sheet. *Reviews of Geophysics and Space Physics*, 10(1).
- Weinstein, M. and Rao, A. V. (2011-2016). Adigator: A matlab automatic differentiation tool. <https://sourceforge.net/projects/adigator/>.
- Werder, M. a., Hewitt, I. J., Schoof, C. G., and Flowers, G. E. (2013). Modeling channelized and distributed subglacial drainage in two dimensions. *Journal of Geophysical Research: Earth Surface*, 118(4):2140–2158.
- Yang, K. and Smith, L. C. (2016). Journal of Geophysical Research : Earth Surface. *Journal of Geophysical Research*, pages 1–20.
- Yang, K., Smith, L. C., Chu, V. W., Gleason, C. J., and Li, M. (2015). A caution on the use of surface digital elevation models to simulate supraglacial hydrology of the Greenland ice sheet. *IEEE Journal of Selected Topics in Applied Earth Observations and Remote Sensing*, 8(11):5212–5224.
- Zwally, H. J., Abdalati, W., Herring, T., Larson, K., Saba, J., and Steffen, K. (2002). Surface melt-induced acceleration of Greenland ice-sheet flow. *Science (New York, N.Y.)*, 297(5579):218–22.

Appendix A

Additional Sensitivity Analysis Plots of the Integrated Model

This appendix contains plots detailing the sensitivity analysis performed in Chapter 5 (Figure A1 - A4). The sensitivity analysis is centred around a calibrated run which differs from the one used in the main text. Both the initialization and time step output are slightly different. The primary difference is that the distribution of sheet conductivity and englacial storage are initialized with a different random distribution. Additionally, a plot of measured velocities and model velocities at 6 h intervals is included (Figure A5).

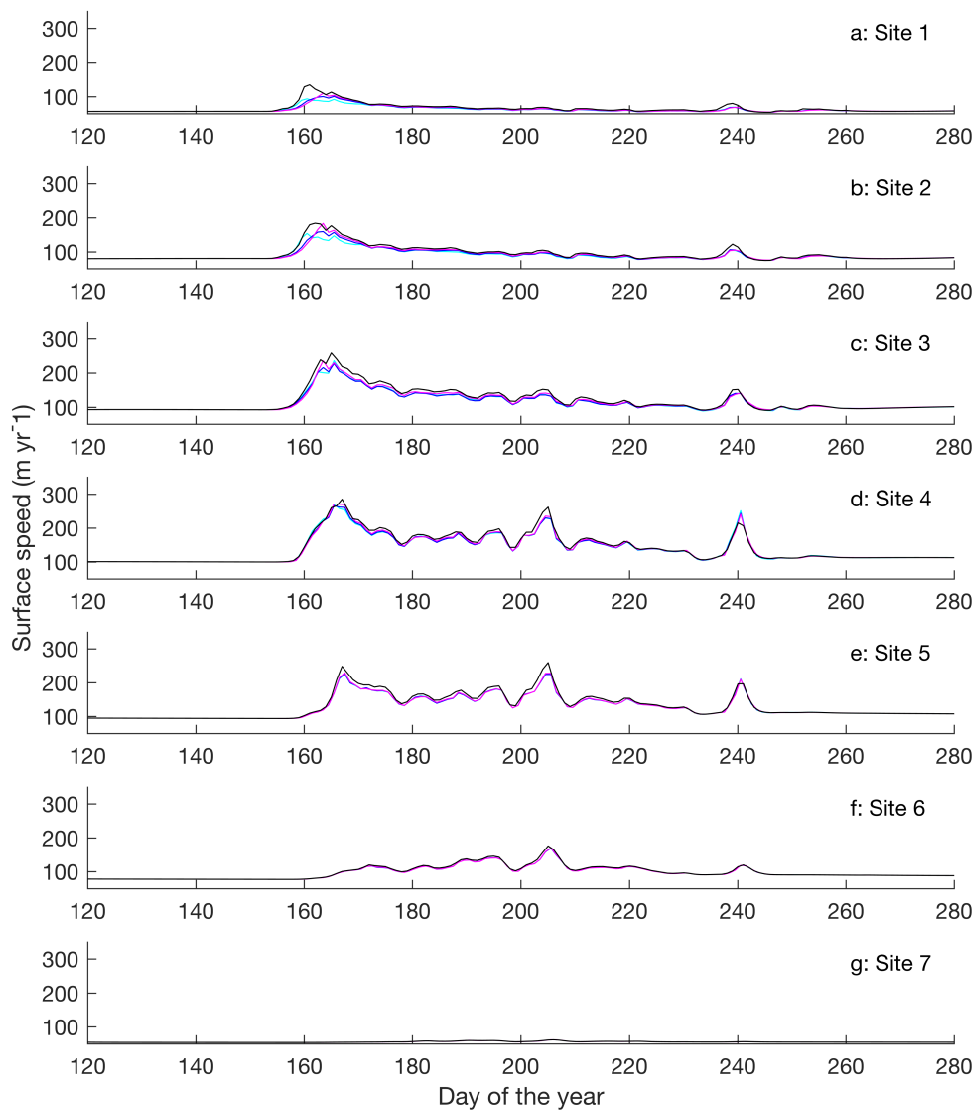


Fig. A.1 Sensitivity analysis of varying crevasse drainage. The calibrated simulation for 2011 is in black. Model simulations with a moulin volume threshold of 10^5 and 10^6 are in cyan and blue respectively. The model simulation neglecting water generated over crevasse fields and only using water flowing into crevasses from external streams is in magenta.

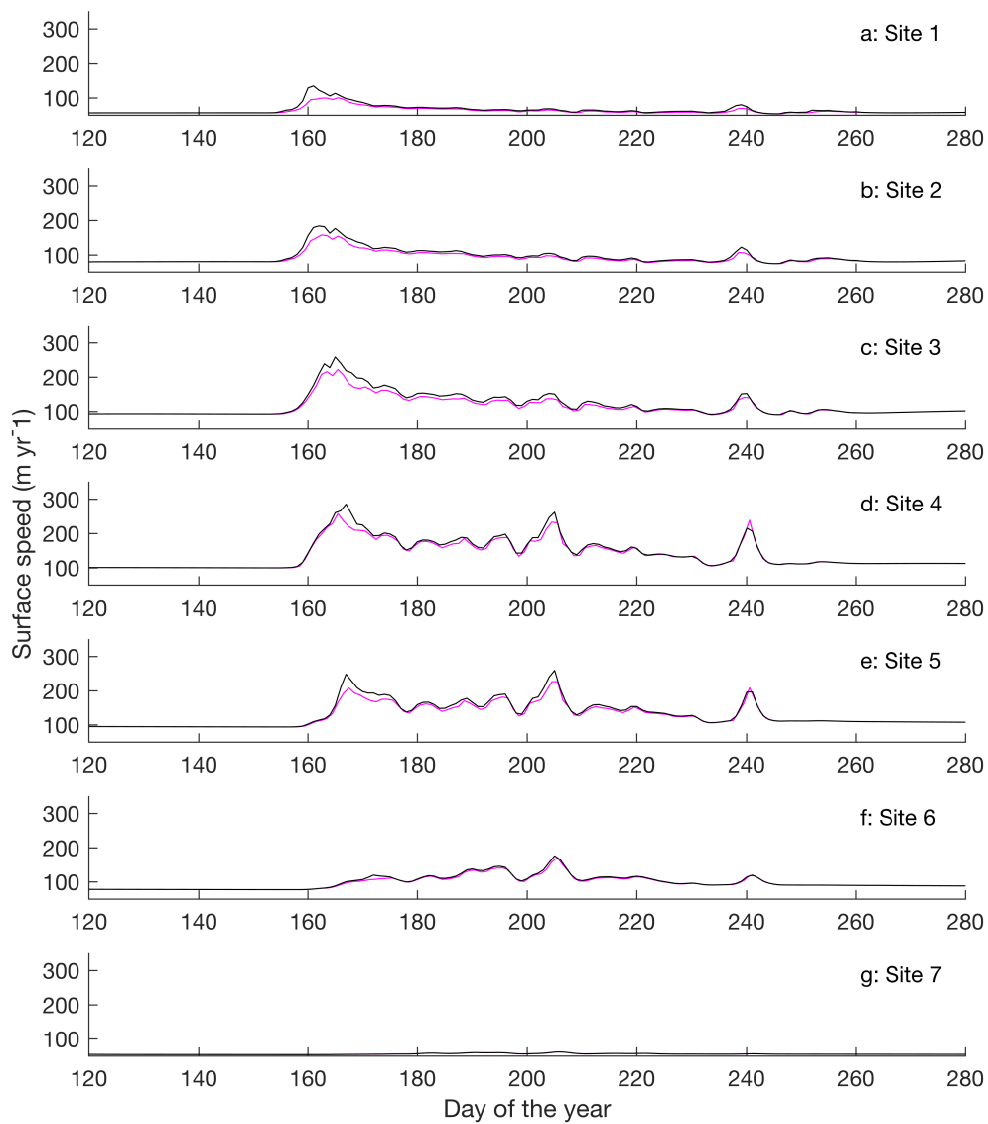


Fig. A.2 Sensitivity analysis of lake hydrofracture events. The calibrated simulation for 2011 is in black. Model simulation eliminating the initial input of water during the hydrofracture event is plotted in magenta

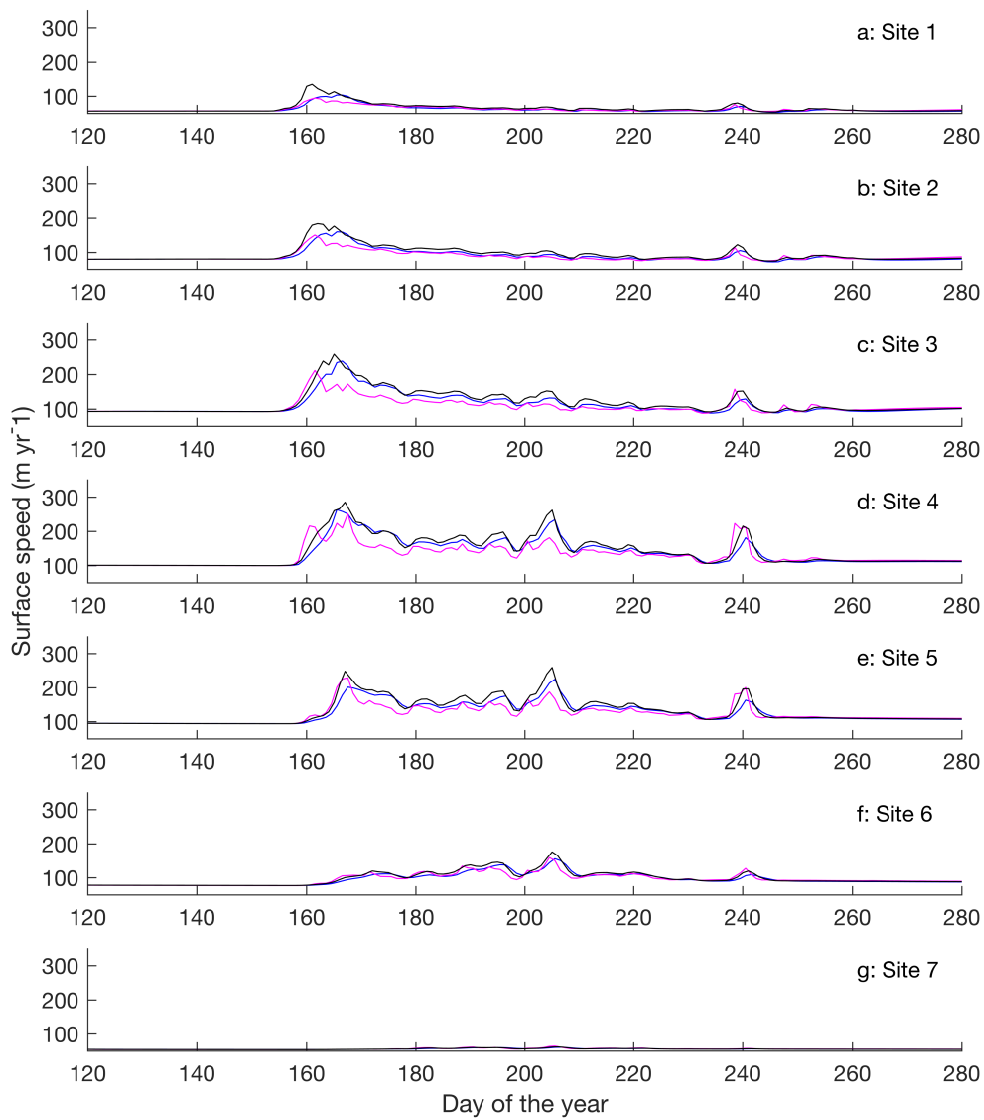


Fig. A.3 Sensitivity analysis of englacial storage. The calibrated simulation for 2011 is in black. Model simulations with values of 10^{-3} and 10^{-4} are in blue and magenta respectively

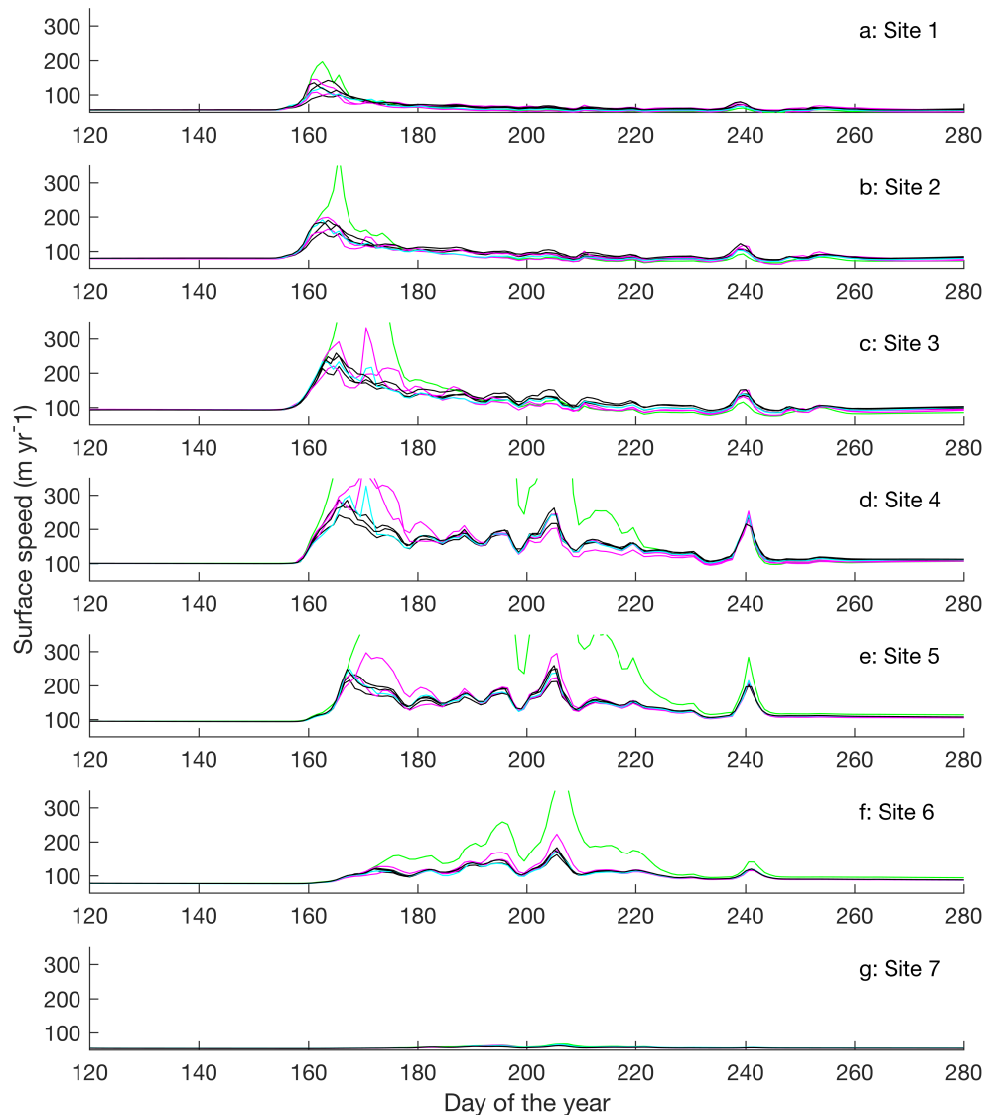


Fig. A.4 Sensitivity analysis of hydraulic conductivity. The calibrated simulation for 2011 is plotted in black. Simulation results for using a spatially homogeneous value of 10^{-2} and for randomly assigning 30% of initial cell nodes a value of 10^{-7} show similar results to the calibrated run. Both simulations are also plotted in black. A simulation increasing the percentage of cells assigned a value of 10^{-7} to 50% is shown in cyan. The sensitivity to assigning sheet conductivity in a spatial pattern is also tested. Two simulations are run, both assigning 4x4 blocks of cell nodes seeded at 100 random locations to values of 10^{-7} . The number of random seeds was chosen so that if there was no overlap between the blocks 20% of the study area would be assigned the lower value. Both these simulations are plotted in magenta. The result of assigning a constant value of 10^{-3} across the entire domain is shown in green.

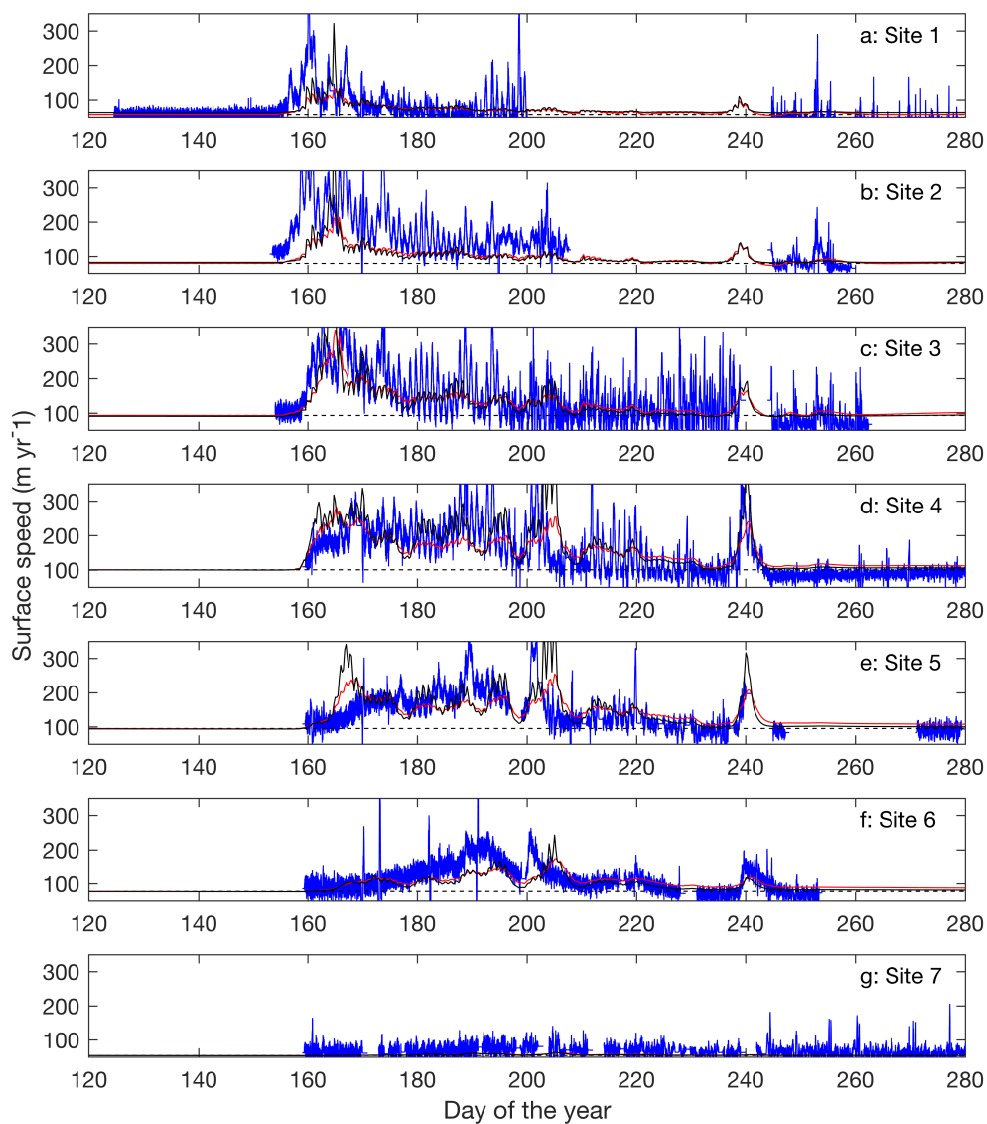


Fig. A.5 Measured and modelled velocities at 6 h intervals. Measured velocities are plotted in blue, modelled velocities using the Schoof sliding law are plotted in black, and modelled velocities using the Weertman sliding law are in red. Dashed black line indicates winter mean.